Using Allosteric Transition Models to Gain Insight on the Signaling Response of Membrane Modulated Proteins

A THESIS SUBMITTED TO THE FACULTLY OF THE UNIVERSITY OF MINNESOTA BY

Stephanie Ellen Greengo Kobany

IN PARTIAL FULLFILLMENT OF THE REQUIREMNTS FOR THE DEGREE OF MASTER OF SCIENCE

Anne Hinderliter

July 2016

Acknowledgments

I would to thank Dr. Anne Hinderliter for the opportunity to become a member of the Hinderliter lab. Her encouragement and mentoring style allowed me to learn more than imagined during the past two years and I am forever grateful for this challenging experience. Thank you to the entire Hinderliter lab, past, present, and future, especially Ben Horn, Ben Orpen, Katie Dunleavy, Mike Fealey, Katie Pederson, and Dr. Jacob Gauer. This work would not have been completed without their constant support and advice. A huge thank you is owed to Dr. John Evans for his guidance and words of inspiration at the times I needed them the most. Lastly, I would like to thank my husband for his patience and devotion during my academic endeavors.

Dedication

To the woman who inspired me to move mountains.

Abstract

The signaling response of membrane modulated proteins are influenced by their complex lipid environments. To further understand the mechanistic role of their signaling response and the influence of their environment, the structure and functionality of membrane protein systems were studied. Synaptotagmin I (Syt 1) is a vesicle-localized integral membrane protein that sense calcium ions (Ca^{2+}) for neuronal exocytosis. The utilization of the cytosolic domains and the role of the intrinsically disordered region (IDR) between Syt I's transmembrane helix and first C2 domain (C2A) in the allosteric communication and modulation of Ca^{2+} binding are poorly understood. Using differential scanning calorimetry (DSC), nuclear magnetic resonance, and isothermal titration calorimetry (ITC), the structure of the IDR and allosteric modulation of Ca^{2+} on Syt I's C2A investigated. Annexins are a large class of membrane binding proteins which are found in all eukaryotic cells and are capable of both sensing membrane damage and orchestrating its repair by means of Ca^{2+} and membrane binding. Annexin a5 is one of many annexins found in muscle cells, and is known to have a mechanistic role in membrane repair. The inability of the cell to repair its membrane after damage causes forms of muscular dystrophy, and it is this repair process that is poorly understood. Using DSC and ITC, the impact of mole fraction of cholesterol within the membrane was studied. Epidermal Growth Factor Receptor (erbB1) is a transmembrane receptor tyrosine kinase that is implicated in normal cellular growth and development. Mutation and/or overexpression of erbB1 can lead to constitutive activity resulting in uncontrolled cellular proliferation. Using single particle tracking of quantum dot-labeled receptors in the plasma membrane of live cells, receptor mobility and interactions were observed in real time. Through analysis of these trajectories, an allosteric transition model was developed to provide a new understanding on the effect of lipid ordering on the conformational distribution and behavior of erbB1.

Table of Contents

List of Tables

List of Figures

List of Abbreviations

Syt I – Synaptotagmin I
Ca^{2+}– calcium ion
IDPs – intrinsically disordered proteins
IDRs – intrinsically disordered protein regions
DSC – differential scanning calorimetry
NMR – nuclear magnetic resonace
CD – circular dichroism
ITC – isothermal titration calorimetry
MOPS – 3-(N-morpholino) propanesulfonic acid
HEPES – 2-[4-(2-hydroxyethyl)piperazin-1-yl]ethanesulfonic acid
EGTA – ethylene glycol-bis(2-aminoethyl)-N,N,N',N' tetra-acetic acid
PS – Phosphatidylserine
PC – Phosphatidylcholine
PI – Phosphatidylinostitol
PE – Phosphatidylethanolamine
POPC – 1-Palmitoyl-2-Oleoyl-sn-Glycero-3-Phosphocholine
POPS – 1-Palmitoyl-2-Oleoyl-sn-Glycero-3-Phosphoserine
POPE – 1-Palmitoyl-2-Oleoyl-sn-Glycero-3-Phosphoethanolamine
SOPE – 1-Stearoyl-2-Oleoyl-sn-Glycero-3-Phosphoethanolamine
DMPS – 1,2-ditetradecanoyl-*sn*-glycero-3-serine
LUVs – large unilamellar vesicles
SUVs – small unilamella vesicles
MRE – mean residue ellipticity
CF – carboxyfluoroscien
ΔH – enthalpy of unfolding
T_m – melting temperature
ΔC_p – change in baseline heat capacity
σ – cooperativity factor
DHE – dehydroergosterol
K_{app} –membrane binding affinity
ΔH_{app} – heat of membrane binding
z – average binding stoichiometry of lipids per protein
n1 – high affinity Ca^{2+} binding site class
n2 – low affinity Ca^{2+} binding site class
erbB1 – epidermal growth factor receptor
EGF – epidermal growth factor
WT – wild type
SPT – single particle tracking
QD – quantum-dots
r^2 – squared displacement
HMM – Hidden Markov Model

Chapter One: Introduction and Background

1.1 Membrane Modulated Proteins and their Signaling Response

Basic functionality of cells rely on signals within their environment and must adapt and appropriately respond when such an event occurs. There are multiple ways the desired response is achieved, but in the case of membrane modulated proteins, the response is affected and depends on the environment of the membrane itself. There are two classes of membrane proteins; peripheral and integral. Peripheral membrane proteins bind to the membrane as a result of a signaling event, whereas integral membrane proteins have a region that is buried within the membrane and contains domains on one or both sides of it.[1] While the structure of each class of proteins differ, their functions both can be allosterically regulated.

The function of allosterically regulated proteins are controlled by structural conformation changes. This change can be induced by a ligand binding to the protein and thus, activating the desired signaling response. For peripheral membrane proteins, the ligand must be transmitted through the membrane, while integral membrane proteins can bind to the ligand through their extracellular domains. However, there is a probability that the response occurs in the absence of ligand with allosteric regulation.

1.2 Allosteric Transition Models and Partition Functions

An allosteric transition model can be utilized to uncover underlying behavior of allosteric mechanisms in membrane modulated proteins systems. By using a quantitative model, the thermodynamics of these systems can be linked to their structural foundations.[2] The simplest model that can be utilized is a two-state model, where the states are inactive or active. While each state potentially has multiple confirmations, a thermodynamic cycle can be used to simplify these confirmations into the states the protein can take on. A thermodynamic cycle gives a complete circle of equilibrium to describe the complexity of the system. Through application of a partition function, a probabilistic representation of each state can be determined utilizing these equilibriums. These mathematical relationships allow for a direct readout of thermodynamic parameters by the means of binding experiments or statistical determination of each state.

Chapter Two: Synaptotagmin I's intrinsically disordered region interacts with synaptic vesicle lipids and exerts allosteric control over C2A

*Note: This chapter was reproduced in its entirety with permission from: **Synaptotagmin I's Intrinsically Disordered Region Interacts with Synaptic Vesicle Lipids and Exerts Allosteric Control over C2A** Michael E. Fealey, Ryan Mahling, Anne M. Rice, Katie Dunleavy, Stephanie E. G. Kobany, K. Jean Lohese, Benjamin Horn, and Anne Hinderliter *Biochemistry* **2016** *55* (21), 2914-2926 DOI: 10.1021/acs.biochem.6b00085.

2.1 Introduction

Synaptotagmin I (Syt I) is a vesicle-localized integral membrane protein composed of a short lumenal domain, single transmembrane helix, a cytosolic linker region followed by tandem C2 domains (termed C2A and C2B) that bind acidic phospholipid and calcium ion (Ca^{2+}) (Figure 2.1A). Syt I has been identified as the Ca^{2+} sensor for neuronal exocytosis, providing a biochemical link between the influx of Ca^{2+} induced by propagating action potentials and the fusion of synaptic vesicle and plasma membranes that underlies neurotransmission.[3] How exactly Ca^{2+} ligation of Syt I's C2 domains leads to synchronization of the exocytotic machinery has been studied extensively, but the mechanism for coupled ligation and fusion still remains incompletely understood. We believe that insight into the underlying mechanism requires investigation of allostery in the propagation and modulation of binding signals; an understanding of how binding in one region of the Ca^{2+} sensor influences other distal locations that participate in regulatory protein-protein and/or protein-lipid interactions (and vice versa) is crucial to unraveling coupled Ca^{2+} binding and membrane fusion. Towards this goal, we have shown previously that C2A and C2B are negatively allosterically coupled to one another indicating that binding events in each C2 domain reciprocally regulate one another.[4] It is less clear, however, if the stretch of ~60 amino acids between Syt I's transmembrane helix and C2A plays an important allosteric role in function (Figure 2.1A, amino acid sequence).

Until recently, little attention was given to this juxta-membrane linker's role in neurotransmission as the adjacent C2 domains were assumed to be the primary effectors. However, in recent single vesicle docking and content mixing assays, wherein full-length Syt I was a reconstituted component, missense mutations that perturbed the charge

distribution of the linker were shown to attenuate pore opening, a critical step for membrane fusion. Additionally, large deletions of the linker were found to disrupt vesicle docking.[5] Consistent with these observed *in vitro* disruptions of function, subsequent *ex vivo* studies performed on murine phrenic nerve-hemidiaphragm preparations showed that treatment of these neuromuscular junctions (NMJs) with small peptide derivatives encompassing residues 80-98 of the juxta-membrane linker caused significant inhibition of neurotransmitter release; treated nerves were unable to elicit muscle contraction when stimulated.[6] In *Drosophila melanogaster*, deletion of this juxta-membrane linker abolishes evoked release of neurotransmitter.[7] All of the above findings indicate that the linker region plays an important role in synaptotagmin biology and is worthy of additional inquiry. In this study, we probe juxta-membrane linker function in the context of allosteric regulation.

One approach to assessing allosteric regulation and function is through examination of protein folding.[8,9] When looking at the amino acid sequence of this juxta-membrane linker region (Figure 2.1A, amino acid sequence) with Composition Profiler, it is composed of a significantly high number of positively charged, negatively charged, and polar residues. (Tables S2.1 and S2.2).[10] Such a sequence is consistent with intrinsic disorder suggesting the linker region is unstructured.[11,13] Intrinsically disordered proteins (IDPs) and intrinsically disordered protein regions (IDRs) can, however, fold into stable secondary structure when binding other macromolecules or when mediating biological function.[14] In previous work from our lab, we showed that Syt I C2 domains, though not intrinsically disordered, are characterized by low unfolding free energies that make them sensitive and adaptable to the lipid composition and curvature of membrane vesicles.[4,15,16] In the limited number of structural studies focused on the juxta-membrane linker region, none have assessed the potential impact of lipid composition on structural and folding propensity.[5,17]Given that IDP and IDR folding can be context-dependent, we hypothesized the juxta-membrane linker would be equally if not more sensitive to membrane lipid composition. We examined this potential sensitivity to a more complex and physiological lipid composition (developed previously in reference 16, Figure 2.1B) through application of differential scanning calorimetry (DSC) and nuclear magnetic resonance (NMR) to a juxta-membrane peptide (encompassing either residues 81-157 or

81-142) (Figure 2.1C). In a previous study examining a hexyl-labeled peptide encoding residues 81-98, fluorescence was used to assess the lipid binding specificity of these residues with nitrocellulose strips containing spots of a wide range of lipid species.[6] These results indicated residues 80-98 range likely prefer lipids with acid headgroups with order of preference being phosphatidylinositol monophosphate, phosphatidylinositol bisphosphate, and phosphatidylserine. Given this binding preference, it seemed probable that the linker region constructs used in the current study (Figure 2.1C) would interact with our synaptic vesicle mixture.

Intimately linked to the structural propensity of an IDR is its influence on the function of an adjacent folded domain. Often times IDRs play important functional roles that go unnoticed or are neglected.[18] Intrinsic disorder has, however, been shown to be thermodynamically advantageous for allosteric coupling within proteins.[19] As such, intrinsic disorder is likely of use to Syt I for propagating the Ca^{2+} and lipid binding signals that lead to regulated release of neurotransmitter. We investigated the impact of the juxta-membrane linker on Syt I's first C2 domain (C2A) by applying DSC, circular dichroism (CD), and isothermal titration calorimetry (ITC) to three C2A constructs: a short C2A (encoding residues 140-265), a medium C2A (encoding residues 96-265) which includes most of the juxta-membrane linker, and a long C2A (encoding residues 83-265) that includes essentially all of the linker (Figure 2.1C). The choice of residues in medium and long C2A constructs was meant to help define a potential role for the high density of lysine residues just proximal to Syt I's transmembrane helix.

Overall, our findings indicate that the juxta-membrane linker has a distinct interaction with membranes whose lipid composition mimics that of the outer leaflet of a synaptic vesicle. Intriguingly, comparison of short, medium, and long C2A constructs revealed that inclusion of residues 83-139 or 96-139 resulted in unique allosteric modulations of C2A. This was apparent in both the thermodynamic parameters describing DSC unfolding profiles as well as ITC-derived Ca^{2+} binding profiles of the three protein constructs. In addition to the lipid induced changes in the linker, we found through application of a dye efflux assay that the juxta-membrane linker has a reciprocal impact on the membrane causing vesicle destabilization. Collectively, these results strongly indicate that the juxta-membrane linker, an IDR, is not a passive structural element of Syt

I but instead plays a complex regulatory role in the molecular control of Ca^{2+} sensing through allosteric coupling to the adjacent C2 domains.

2.2 Experimental Procedures

2.2.1 Reagents

Potassium chloride (KCl) and sodium chloride (NaCl) were Puriss-grade. Calcium chloride dehydrate, 3-(N-morpholino) propanesulfonic acid (MOPS), 2-[4-(2-hydroxyethyl)piperazin-1-yl]ethanesulfonic acid (HEPES) and ethylene glycol-bis(2-aminoethyl)-N,N,N',N' tetra-acetic acid (EGTA) were Biochemika grade from Fluka Chemical Corp. Urea and imidazole were obtained from Sigma-Aldrich. Dithiothreitol (DTT) was obtained from ThermoFisher Scientific. $^{15}NH_4Cl$ and ^{13}C-glucose for isotopic labeling were obtained from Cambridge Isotope Laboratories. All buffers were decalcified using Chelex-100 ion-exchange resin (Bio-Rad Labs). All glycerophospholipids including phosphotidylcholines, phosphatidylethanolamines, phosphatidylinositols, and phosphatidylserines with mixed acyl chain unsaturations were obtained from Avanti Polar Lipids (Birmingham, AL) and included the following: 1-palmitoyl-2-oleoyl-*sn*-glycero-3-phosphocholine (16:0, 18:1 POPC); 1-palmitoyl-2-oleoyl-*sn*-glycero-3-phosphoserine (16:0, 18:1 POPS); 1-stearoyl-2-oleoyl-*sn*-glycero-3-phosphoethanolamine (18:0-18:1 SOPE); 1-palmitoyl-2-oleoyl-*sn*-glycero-3-phosphoethanolamine (16:0-18:1 POPE); 1-stearoyl-2-docosahexaenoyl-*sn*-glycero-3-phosphoethanolamine (18:0-22:6 PE); 1-stearoyl-2-oleoyl-*sn*-glycero-3-phosphoethanolamine (18:0-18:1 PE); 1-palmitoyl-2-oleoyl-*sn*-glycero-3-phosphoethanolamine (16:0-18:1 PE); 1-stearoyl-2-docosahexaenoyl-*sn*-glycero-3-phosphoserine (18:0-22:6 PS); 1-stearoyl-2-oleoyl-*sn*-glycero-3-phosphoserine (18:0-18:1 PS); 1-stearoyl-2-arachidonoyl-*sn*-glycero-3-phospho-(1'-myo-inositol-4',5'-bisphosphate) (18:0-20:4 PI(4,5)P2); 1,2-dioleoyl-*sn*-glycero-3-phospho-(1'-myo-inositol-4',5'-bisphosphate) (18:1-18:1 PI(4,5)P2); 1-palmitoyl-2-oleoyl-*sn*-glycero-3-phosphoinositol (16:0-18:1 PI); cholesterol.

2.2.2 Preparation of Lipid Vesicles

Large unilamellar vesicles (LUVs) and small unilamellar vesicles (SUVs) consisting of POPC:POPS (60:40), POPE:SOPE:POPS (38:38:24) or the synaptic vesicle mimic shown in Figure 1B were prepared as previously described, hydrated with buffers relevant to each experiment described below.[16] In each synaptic vesicle mimic preparation, cholesterol in the quantity of 45% of the total moles of phospholipid was doped into the aliquoted phospholipid resulting in a final cholesterol content of ~31% of total lipid (compare pie charts in Figure 2.1B). Concentrations for all lipid stock solutions were verified using a phosphate assay as described in reference 20.[20]

2.2.3 Protein Purification and Peptide Design

Human Syt I C2A constructs including a short C2A construct encoding residues 140-265, a medium C2A construct encoding residues 96-265, and a long C2A construct encoding residues 83-265 were all expressed and purified as fusion proteins as described previously.[4,15] For DSC and CD experiments for which small quantities of protein are needed, the linker region peptide specifically encoding residues 81-157 was produced via solid state synthesis through the University of Minnesota Genomics Center:

KKCLFKKKNKKKGKEKGGKNAINMKDVKDLGKTMKDQALKDDDAETGLTDGEEK EEPKEEEKLGKLQYSLDYDFQNN

Inclusion of residues 143-157, which corresponds to part of C2A's first beta strand, was done so that the peptide would contain absorbing residues for measuring concentration. The linker region is otherwise nearly devoid of absorbing residues. For nuclear magnetic resonance experiments, a linker region gene encoding residues 81-142, with additional codons for a single C-terminal tryptophan followed by a His-tag, was designed:

KKCLFKKKNKKKGKEKGGKNAINMKDVKDLGKTMKDQALKDDDAETGLTDG EEKEEPKEEEKWHHHHHH

The tryptophan in this case was added for the same reason as residues 143-157 in the synthesized peptide. This linker region gene was inserted into a pET28 plasmid,

transformed into BL21 *E. coli* cells, grown to a cellular OD of 0.8, and induced via IPTG in minimal media containing $^{15}NH_4Cl$ and ^{13}C-glucose. Cells were then allowed to express overnight at 18 °C before being pelleted for purification. Cells were lysed in 25 mM HEPES, 250 mM NaCl, and 4 M urea. The cell debris was subsequently removed via centrifugation at 40,000 rpm for 30 minutes. The resultant supernatant was equilibrated with Ni column media to bind the His-tagged juxta-membrane linker peptide. The Ni column was washed with buffer containing 25 mM HEPES, 250 mM NaCl, 4 M urea, and 30 mM imidazole to remove non-specific binding of proteins. The linker region peptide was subsequently eluted from the Ni column using the same buffer above but with 150 mM imidazole. The eluted peptide was then subjected to gel filtration to further purify. Final purity of the juxta-membrane linker peptide was verified via SDS-PAGE (Figure S1) and spectroscopic absorption at 260 nm and 280 nm wavelengths in a Beckman spectrometer. The 260/280 ratio was <0.70 indicating >95% purity in terms of nucleic acid contamination. The pure linker ran on SDS-PAGE at an anomalously high molecular weight. Other proteins containing intrinsic disorder and high charge density have been shown to exhibit this same character.[21] To verify the linker region peptide was not proteolytically cleaved and the appropriate molecular weight, MALDI-TOF mass spectrometry was performed on the pure product and was found to be at the expected value. Alternatively, the high molecular weight may be due to the construct being in dimeric form in solution due to its high degree of charge separation. Final protein concentrations for all linker region and C2A constructs were determined with both Nanodrop (ThermoScientific) and Beckman spectrometers using each construct's respective A280 extinction coefficient.

2.2.4 Differential Scanning Calorimetry

DSC experiments were performed on a NanoDSC (TA Instruments, New Castle, DE) at a scan rate of 1 °C/min as described previously.[4,15] All scans were conducted in chelexed 20 mM MOPS, 100 mM KCl, pH 7.5. The concentration of the synthesized linker region peptide, short C2A, medium C2A, and long C2A in all DSC replicate scans containing synaptic vesicle lipid LUVs were 18 μM, 13 μM, 13 μM, and 13 μM, respectively. For long and medium C2A DSC scans carried out in the absence of any

ligand, protein concentrations were 26 μM and 13 μM, respectively and 500 μM EGTA was included to ensure Ca^{2+}-free conditions. All scans carried out with ligand had Ca^{2+} and LUV (either 60:40 POPC:POPS or synaptic vesicle mixtures) concentrations of 1 mM each. To rule out the possibility of LUVs whose lipid composition mimicked that of a synaptic vesicle contributing to the measured excess heat capacity, a temperature scan was performed on an equal concentration of liposomes and Ca^{2+} as in protein-containing experiments. No clear phase transition was observed, as seen previously.[14] This is consistent with the fact that both increased number of lipid components and a high mole fraction of cholesterol both mute the phase transition of any one lipid species.[20] The concentration of the Ca^{2+} stock solution used for all scans was verified using both a calcium ion selective electrode (ThermoScientific) and a BAPTA chelating assay (Invitrogen/Molecular Probes, Eugene, OR). Lipid stock solution concentrations were verified using a phosphate assay.

2.2.5 Nuclear Magnetic Resonance

NMR was performed on the linker region peptide at the MNMR facility at the University of Minnesota in Minneapolis. Spectra were recorded at 25 °C using both a Varian 600 MHz spectrometer equipped with a cryoprobe (for lipid-containing samples) and a Bruker 850 MHz spectrometer (for partial assignment). NMR samples contained 20 mM MOPS, 100 mM KCl, 0.5 mM DTT, 7% D_2O v/v, at a pH of 6. A lower pH value was chosen to limit the amount of chemical exchange since at physiological pH several cross peaks disappear from the spectrum (Figure S2). At this lower pH the IDR-membrane interaction is still of comparable K_d to a the physiological value (Figure S3). To obtain the partial backbone assignment HNCACB, HNCOCACB, HNCA, and HNCO triple resonance experiments were performed. The resulting data sets were processed in NMRPipes and subsequently analyzed using Sparky software. In samples containing 60:40 POPC:POPS SUVs or synaptic vesicle mixture SUVs, freshly purified Syt I IDR was mixed with 1 mM or 3 mM SUVs and placed in the spectrometer for a 10 hour acquisition period. Each lipid-containing sample was run for this same time period and, in the case of the 3 mM synaptic vesicle mimic SUV sample, fresh IDR linker and fresh lipid were used to prepare a new sample for data acquisition rather than adding more lipid

to the existing 1 mM sample. In these lipid-containing samples, the concentration of Syt I IDR was always 30 μM.

2.2.6 Circular Dichroism

CD was performed on 15 μM short C2A, medium C2A and long C2A (in the same buffer system described for DSC experiments) in a 0.1 cm quartz cuvette using a J-810 JASCO spectropolarimeter. Three replicates were collected for each protein construct. Far-UV spectra were collected over a wavelength range of 200-260 nm for MOPS-containing buffer and 190-260 nm for sodium phosphate buffers. Data points were collected in 1 nm increments and averaged over 5 acquisitions. Spectra were corrected for any buffer, liposome, or urea contributions by subtracting a corresponding scan of an identical solution without protein. Resulting data sets were plotted as mean residue ellipticity (MRE) according to the following equation:

$$MRE = (\theta*(MW/N-1))/(lc) \quad (2.1)$$

Where θ represents the raw ellipticity, MW represents protein molecular weight, N is the number of amino acids, l is path length and c is concentration in mg/mL. In the case of scans carried out in the presence of urea, 60 μM synthesized juxta-membrane peptide was used and shorter wavelengths below 207 nm had poor signal-to-noise due to high dynode voltage. As such, those wavelengths were not collected in 1M and 4M urea-containing samples.

2.2.7 Isothermal Titration Calorimetry

ITC was carried out on a NanoITC (TA Instruments) according to the same rigorous procedures recently described.[23] Briefly, protein samples were thoroughly degassed for 20 minutes and quantified via Nanodrop prior to loading into the sample cell. Calcium chloride dissolved in the same buffer as the protein was then loaded into the titration syringe. The instrument was allowed to equilibrate both prior to and after the initiation of stirring. Heats of dilution were conducted by repeating each titration with

identical titrant concentrations in the absence of macromolecule. These were then subtracted from the corresponding protein titrations before data analysis.

2.2.8 Carboxyfluoroscein efflux

Carboxyfluoroscein efflux experiments were performed similarly to that described in reference 13. Briefly, lipids were hydrated with buffer containing 200 mM carboxyfluoroscein (CF), hand extruded through a 0.1 μm polycarbonate filter and subsequently buffer exchanged using a Sephadex 200 size exclusion column. Vesicles were placed in cuvettes with juxta-membrane peptide (or Ca^{2+}-saturated short C2A as a positive control) and subjected to CF excitation (492 nm) in a Fluorolog 3 spectrophotometer (Horiba Jobin Yvon) while being monitored at 519 nm as the sample was cooled from 37 °C to 7 °C.

2.2.9 Data Analysis

The thermodynamic parameters enthalpy of unfolding (ΔH), melting temperature (T_m), and change in baseline heat capacity (ΔC_p) obtained from DSC denaturation experiments were used to calculate free energies of stability at 37 °C using the Gibbs-Helmholtz equation as described previously (see references 4 and 15):

$$\Delta G = \Delta H(1 - T/T_m) + \Delta C_p(T - T_m - T\ln(T/T_m)) \qquad (2.2)$$

With regard to analysis of ITC data, titrations were fit using a partition function approach that was used previously in our Syt I C2A terbium binding studies.[15,24] The partition function allows for characterization of microscopic binding states of the protein. The partition function is:

$$Q = 1 + 2K[X] + \sigma K^2[X]^2 \qquad (2.3)$$

Where K represents the equilibrium constant of Syt I C2A for ligand, [X] represents free calcium ion concentration, and σ represents a cooperativity factor. Values of $\sigma>1$ indicate the presence of positive cooperativity between cation binding sites. As the titrations did

not include lipid, the above partition function does not take into account lipid-bound states of the protein which would further expand the partition function. It is important to note that because the third cation binding site is of very low affinity (K_d > 1mM) in the absence of membrane containing acidic phospholipid[24,25], the model above assumes that binding involves only 2 of the 3 binding sites (n = 2).

2.3 Results

2.3.1 The disordered linker region of Syt I has an endothermic transition in the presence of membrane that mimics a synaptic vesicle

To first see if Syt I's juxta-membrane linker would potentially order in the presence of membrane, we performed DSC unfolding experiments on a linker region peptide (encompassing residues 81-157) in the presence of LUVs with a 60:40 mole ratio of POPC and POPS and Ca^{2+}. Under these membrane conditions, no clear unfolding transition was observed (Figure 2.2A). Knowing that order within an IDR is typically context dependent, we repeated the DSC experiment with membrane containing a more complex and more physiologically relevant lipid composition (Figure 2.1B). This lipid mixture consists of polyunsaturated neutral and acidic phospholipids as well as cholesterol. We developed this synaptic vesicle mimetic based on mass spectrometry data obtained from a purified synaptic vesicle (see reference 26) and showed previously that the Syt I C2A domain has a unique thermodynamic profile in the presence of this lipid composition.[16,24] Strikingly, Syt I's linker region was equally responsive; when denatured in the presence of our synaptic lipid LUVs, a clear but weak endotherm was observed (Figure 2.2B). This transition did not seem to stem from the synaptic lipids themselves, as a scan of LUVs and Ca^{2+} alone did not show an obvious transition (Figure 2.2C). Moreover, lipid phase transitions do not have changes in baseline heat capacity which is typically a feature of protein phase transitions. These results suggest that, with a synaptic vesicle-like environment, Syt I's juxta-membrane IDR can exist in a membrane-associated state that has measurable heat capacity. While DSC does not provide direct information on the type of folded structure, the small endotherm (particularly on the reversibility scan, dashed light green) does indicate weak intramolecular interactions

within the IDR when membrane associated. This is consistent with the limited number of structural studies performed on this region of Syt I. In previous electron paramagnetic resonance (EPR) studies wherein nitroxide spin labels were attached to the juxta-membrane linker region, continuous wave measurements from one study showed significant probe mobility in the juxta-membrane region of Syt I whereas DEER (double electron-electron resonance) intermolecular distance distributions measured in another study contained significant structural disorder.[5,17]

A notable feature of the Syt I linker's transition in the presence of our synaptic vesicle mimic is the dramatic shift in T_m between first and second DSC scans. On the first denaturation scan there is a T_m of nearly 75 °C and on the second a T_m of 56 °C. This change likely relates to the thermal annealing of synaptic vesicle lipids. When synaptic lipid vesicles are initially added to a solution of juxta-membrane linker, the membrane surface will have some arrangement of lipids dictated by the lipid-lipid interaction network at ambient temperature. This lipid arrangement will select some disordered structural state of the juxta-membrane linker that has a measurable heat capacity. In the calorimeter, however, the high temperature of denaturation will not only disorder the protein but also rearrange the lipids in the membrane surface. Upon cooling of the DSC sample, which is now in the presence of juxta-membrane linker, the synaptic vesicle lipids may organize differentially and, as a result of additional interactions with protein, select an alternate ordered state of the juxta-membrane peptide that has a distinct endotherm. Another alternative is that the synaptic vesicle mimic LUVs facilitates formation of an oligomerized structure of the IDR on the surface of the membrane that, upon heating, dissociates resulting in a monomeric membrane-associated form upon second heating.

2.3.2 Microscopic changes of Syt I linker brought about by synaptic vesicle mimic are visible with solution state NMR

While DSC provides a macroscopic picture of Syt I's juxta-membrane linker region when associated with our synaptic vesicle mimic, we also wanted to assess microscopic features. To do this, we sparingly used solution state NMR. In the absence of any lipid vesicles, Syt I's linker region had a characteristic HSQC spectrum for an

unfolded protein (Figure 2.3A). Despite poor peak dispersion, we were still able to obtain partial assignment of the amide backbone, particularly the central region where amino acid sequence complexity is highest (Figure S2.4 and S2.5). This served as a reference point for lipid-induced chemical shift perturbation.

Because of the repeat nature of the Syt I linker amino acids, several peaks in the HSQC spectrum could not be unambiguously assigned. Multiple sequential lysines, glutamates, and aspartic acids, for example, appear in more than one region of the sequence, as do other residue pairs (Figure S2.6). Additionally, these regions exhibit extensive C_α and C_β chemical shift peak overlap. Regardless, we were still able to assess residual secondary structure from the residues examined by subtracting IDP-/IDR-specific random coil chemical shifts from the observed C_α, C_β and carbonyl carbon chemical shifts.[27] In the majority of assigned residues subjected to this secondary structure analysis, there appears to be no strong preference for residual structure; both C_α-C_β and carbonyl carbon chemical shift differences alternate between positive and negative values indicating this linker region is largely random coil in solution (Figure 2.3B and 2.3C). This finding is consistent with circular dichroism measurements of the IDR (Figure 2.3D) and predictions of Composition Profiler (Table S2.2). However, there may still be minor residual helical content given that equilibration with increasing concentrations of urea results in the juxta-membrane linker more closely resembling the absorption profile of random coil (Figure 2.3D).[28] Alternatively, the increased absorption at ~220 nm with increasing urea could be the result of the juxta-membrane peptide regions adopting polyproline type II helical conformers which can occur in peptides containing multiple sequential lysine residues at near-neutral pH.[29]

After examining the Syt I linker region in the absence of membrane, we then acquired data on samples containing SUVs (which more closely mimic the curvature of a synaptic vesicle) of either a 60:40 POPC:POPS or synaptic lipid composition and monitored which of the assigned regions of the linker underwent chemical shift perturbation. SUVs of POPC:POPS showed little to no effect, largely causing peak broadening (and disappearance) presumably due to membrane association (Figure 2.4A). In contrast, synaptic lipid SUVs caused more pronounced spectral changes. For example, residues A101, I102, V107, T113, A118, and L119 seem to experience larger changes in

their local environment as their membrane-free chemical shifts are missing in the presence of synaptic lipid SUVs (Figure 2.4B-D). More generally, the spectra show greater peak dispersion and some chemical exchange (Figure 2.4D). Since amide chemical shifts are particularly sensitive to structure, such changes are potentially due to partially ordered but dynamic states of the Syt I linker region.

If the Syt I IDR undergoes ordering upon membrane association, a likely form of secondary structure would be that of an α-helix. However, when we measured secondary structure of the Syt I IDR bound to synaptic mimic vesicles using circular dichroism, the IDR seemed to remain mostly disordered (Figure S2.7). The structures of IDRs when membrane associated can vary greatly. In some cases, IDRs can interaction with membranes and be only marginally helical, as was found for the CD3ε cytoplasmic domain.[30] Alternatively, some remain largely disordered.[31] As an example of the latter, a recent comprehensive study examining membrane-IDR interactions of prolactin (PRL) and growth hormone (GH) receptor cytoplasmic domains found these IDRs to exist in a membrane-bound form that was still largely disordered. The Syt I IDR may fall into a similar category as PRL and GH cytoplasmic domains. As further evidence of this, in the study of PRL and GH cytoplasmic domains, lipid interactions were found to be mediated by both a basic patch and downstream hydrophobic staple motifs.[31] A similar mechanism may occur within the Syt I IDR, as the plethora of lysine residues in the 80-98 range contain motifs similar to other PIP_2-binding proteins such as that found in the B motif of N-WASP, and represents what would be the analogous basic patch.[32] Downstream of these Syt I lysines are hydrophobic residues spaced similarly to that proposed for the hydrophobic staples of PRL and GH receptor IDRs of reference 35. Indeed, several of those hydrophobic residues on the Syt I IDR undergo the largest change in chemical environment when presented with synaptic SUVs (Figure 2.4D).

A likely complicating factor to studying the juxta-membrane linker with a synaptic vesicle mimic is membrane-mediated aggregation. In the absence of any membrane, a 75 μM juxta-membrane linker sample seems to be relatively stable. However, an HSQC of the same sample days after all three dimensional experiments were performed suggested the start of protein aggregation (Figure S2.8). When synaptic vesicle mimic SUVs are introduced, cross peaks in the same region of the spectrum

appear and broaden (Figure 2.4C). Protein aggregation is a kinetically slow process with nucleation being the rate-limiting step. However, if the protein has a specific association with synaptic vesicle lipids, this will reduce the volume dimensionality and consequently enhance this form of peptide organization. Despite this complication, the spectral changes present in synaptic lipid-containing samples still have features that distinguish it from protein aggregation alone. Moreover, the spectral changes are distinct from POPC:POPS spectra and thus indicate a specific response to the synaptic vesicle lipid composition.

2.3.3 Syt I linker region exhibits allosteric control over the adjacent C2A domain

Having identified a specific synaptic lipid-IDR interaction within Syt I, we next examined whether or not it was thermodynamically coupled to its adjacent Ca^{2+}-binding C2 domain (C2A). If this IDR of Syt I is capable of propagating Ca^{2+} ligation signals that occur in C2A or of modulating Ca^{2+} binding by C2A, there will be a measurable difference in the thermodynamic parameters of denaturation obtained from DSC endotherms. Such an approach was applied previously to Syt I's C2 domains but in the current study we compared unfolding of a short C2A construct (encoding residues 140-265), a medium sized C2A construct (encoding residues 96-265), and a long C2A construct that includes essentially the entire length of the linker region (encoding residues 83-265).[2]

For the short C2A domain, denaturation in the presence of synaptic vesicle mimic LUVs and Ca^{2+} results in a measured unfolding free energy (calculated with Equation 2.2) of 2.25±0.09 kcal/mole (Figure 2.5A and Table 2.1). Under identical conditions the medium C2A construct was found to have an unfolding free energy of 3.30±0.6 kcal/mole. This increase in free energy of unfolding that comes from inclusion of residues 96-139 indicates that this portion of the linker region confers added stability to the protein (Figure 2.5B). In the HSQC spectra above, the central portion of the linker seems to undergo structural changes (Figure 2.4D). If such spectral changes represent more ordered conformers resulting from interactions with synaptic lipids, the Ca^{2+}-enhanced C2A membrane association may accentuate linker ordering in that region, a form of positive (stabilizing) allosteric coupling. Indeed, when looking at the DSC unfolding profile of medium C2A in the presence of synaptic lipid LUVs and EGTA, a

much broader transition (potentially resulting from two separate unfolding events) can be seen (Figure 2.5B, purple trace). When Ca^{2+} is present, these two transitions coalesce indicative of a more cooperative interaction between the two regions of the protein.[2,6] Moreover, if the endotherms of the linker region peptide (from either the first or reversibility denaturation scan in Figure 2.2B) and short C2A (Figure 2.5A) are summed together, the resultant excess heat capacity curve does not recapitulate the more cooperative unfolding transition of medium C2A (Figure 2.5C). Of additional note, residues 96-139 in medium C2A also seem to enhance reversibility of protein folding, perhaps by acting as an entropic bristle.[31] It should be noted, however, that just as in DSC scans of juxta-membrane linker and synaptic lipids, medium C2A reversibility scans seem to indicate an alternate conformational state of residues 97-139 (compare Figure 2.2B with Figure 2.5D). These two endothermic transitions in the reversibility scan could be consistent with more ordering of the linker's central residues if, for instance, structure of the IDR requires C2-domain pinning to the membrane surface to elevate local lipid concentration.

Similar to medium C2A, when the long C2A construct is denatured under analogous conditions, there is also a change from one to two thermal transitions between first and reversibility scans (Figure 2.5E). However, in long C2A, residues 83-96 seem to weaken the protein construct as indicated by the smaller, less cooperative endotherms (compare Figure 2.5D and 2.5E). As further evidence of these additional 13 residues having an impact on stability, in the absence of any ligand what-so-ever, long C2A has a considerably weaker enthalpy of unfolding than that of the previously characterized short and medium C2A constructs (Figure 2.6A and 2.6B, see reference 15 for comparable stability measure on short C2A).[15] Similar observations wherein a dozen or so amino acids have a significant impact on stability have been made in other IDP systems. One such example is the glucocorticoid receptor, where alternate transcriptional start sites that differentially truncate an N-terminal disordered domain result in dramatically different stabilities and corresponding receptor activation activities.[34] When the reversibility scans of both medium and long C2A are compared to reversibility scans of short C2A, there is only a single transition in the short construct (Figure 2.5F). This suggests that the transition occurring at ~60 °C in medium and long C2A constructs results from segments

of the IDR and its interaction with synaptic vesicle lipids. In the case of both medium and long C2A, the T_m and enthalpy of the first unfolding transitions do not change appreciably with different scan rates indicating that the measured transition is not under the kinetic control of an irreversible step after denaturation and thus still reflects an equilibrium process.[35]

2.3.4 Discrete regions of IDR confer alternate modes of C2A Ca^{2+} binding in solution

To further test whether or not residues 83-96 and 96-139 have distinct functional impacts on C2A as suggested by the denaturation experiments, we examined solution-state calcium binding of short, medium, and long C2A constructs using isothermal titration calorimetry (Figure 2.6D-F). The results of the titration experiments were striking, as each of the two regions of the IDR had distinct outcomes on Ca^{2+} binding. To analyze our binding results, we applied a reduced partition function approach applied previously in our lab that enables assessment of binding site cooperativity (Equation 2.3) (Figure 6G-I).[24] This model was used to analyze short C2A binding as an initial reference state and it was found to bind two Ca^{2+} with an affinity of 2600 M^{-1} corresponding to equivalent K_d of 385 μM and cooperativity factor (σ) of 1 (titration n=3; ΔG = -4.49 ±0.07 kcal/mole) (Table 2.2). When σ = 1 it indicates the two binding sites lack cooperativity and are thus independent of one another. When medium C2A Ca^{2+} binding was assessed in the same way, the construct was found to bind Ca^{2+} with an affinity of 1600 M^{-1} and a σ of ~4 giving rise to a K_d of 625 μM for the first Ca^{2+} binding site and a K_d of 169 μM for the second Ca^{2+} binding site. This corresponds to respective binding free energies of -4.24 ±0.11 kcal/mole and -4.96 ±0.09 kcal/mole (titration n=3; binding free energies calculated using $\Delta G = -RT\ln(K)$ or $\Delta G = -RT\ln(\sigma K)$). In this case, the σ of ~4 indicates that residues 96-139 confer modest positive cooperativity to C2A's Ca^{2+} binding sites, consistent with terbium binding studies performed previously on these same two C2A constructs.[15,24]

The titration of Ca^{2+} into long C2A, in contrast, showed drastic attenuation of heats of binding in comparison to the short and medium C2A constructs (titration n=2) (Figure 2.6F). From the DSC denaturation and also circular dichroism (Figure 2.6A and 2.6B), we know that long C2A is still folded albeit more weakly. Additionally, there does

not appear to be a significant interaction between the IDR and C2A (Figure S2.9), arguing against an altered mode of binding resulting solely from physical contact. The end result of IDR inclusion, however, appears to be pronounced alteration of the thermodynamic parameters describing Ca^{2+} binding. Long C2A is still Ca^{2+} binding-competent as evidenced by the fact that addition of Ca^{2+} to the long C2A construct in the absence of any lipid ligand still results in an elevated unfolding temperature (Figure 2.6C) as would be expected from chelation of ligand.

In the case of medium C2A, there is another potential interpretation of the data. In some of the earliest Ca^{2+} binding studies, it was noted that C2A's third cation when bound to the C2 domain had an incomplete coordination sphere thought to be completed by headgroups of acidic phospholipids.[34] While we have modeled binding of two Ca^{2+} to C2A in part because of the millimolar affinity of the third site, it may also be possible for the C2A domain to better chelate three Ca^{2+} with the aid of the acidic IDR residues just upstream of C2A. When you compare ligand-to-protein ratios of short and medium C2A, there is a shift from 2:1 to 3:1 (compare Figure 2.6G and 2.6H). Control HSQC spectra acquired to assess whether or not the IDR with medium C2A somehow participated in Ca^{2+} binding showed only subtle changes and were only apparent at a high concentration of ligand in excess of the physiological maximum (Figure S2.10). Alternatively, the apparent increase in ligand-to-protein ratio can also be a manifestation of the positive cooperativity of binding[37] in a manner similar to (but opposite) that of a substoichiometric ratio resulting from negative cooperativity.[38]

2.3.5 Syt I IDR contributes to membrane destabilization

After examining the impact of lipid composition on the juxta-membrane linker region (Figures 2.2-2.4) as well as the linker region impact on C2A (Figures 2.5 and 2.6), we next asked the question of whether or not the linker perturbs the membrane in a manner that could promote fusion. Previous spin label accessibility measurements used to determine the membrane partitioning depth of the juxta-membrane linker region at several residues along its length indicated that residues in the 80-90 range partially penetrate into POPC:POPS bilayers.[17] A similar profile was seen previously with Syt I C2 domains, where the Ca^{2+}-binding loops of C2A and C2B insert into the bilayer upon Ca^{2+}

binding.[39] Such insertion is a spontaneous process for Ca^{2+}-bound C2 domains, but is energetically unfavorable for the adjacent phospholipids as the protein intercalation reduces lipid conformational entropy by limiting the number of acyl chain rotamers available to the lipids. This intercalation results in membrane destabilization thought to contribute to overcoming the energetic barrier of fusion.[40]

Given that residues in the 80-90 range also partially partition into the membrane as assessed by EPR, it seemed plausible that the linker region could also destabilize the membrane. To test this hypothesis, we applied our previously developed CF efflux assay.[15] In this experiment, vesicles containing CF at self-quenching concentrations are cooled through their gel-to-fluid phase transition temperature. During the lipid transition, there is a packing mismatch between phases making the vesicles more susceptible to leakage of CF outside the vesicle where it is free to fluoresce. When this experiment was performed previously on the C2A domain (residues 140-265, short C2A), it significantly increased CF release consistent with partial insertion into the bilayer as measured by EPR.[13]

We repeated this CF efflux experiment with the Syt I synthesized peptide using vesicles consisting of a 38:38:24 mole ratio of POPE:SOPE:POPS. This composition was chosen because it maintained the physiological features of both unsaturation in the sn2 position and the same relative PE/PS character of the more complex synaptic vesicle mimic. However, by being only monounsaturated, this composition has an elevated phase transition temperature making it more amenable to experimental monitoring of efflux in response to protein. When the CF-containing vesicles were cooled through their transition temperature in the presence of juxta-membrane linker peptide, the percentage of maximal dye efflux increased by 28 relative to the liposomes alone (Figure 2.7). As a positive control, we also performed the experiment with Ca^{2+}-bound short C2A and found that the percentage of maximal dye efflux was increased by 15. This indicates that the magnitude of dye efflux with the IDR is likely relevant to destabilizing the membrane as maximal efflux exceeds that of the known C2A intercalator. Consistent with the EPR measurements of partial insertion, the juxta-membrane linker destabilizes the membrane. This result may be relevant to protein intercalation as a way of destabilizing the membrane and consequently lowering the energetic barrier to fusion.

2.4 Discussion

In this study, we present evidence in support of Syt I's IDR acting as functional domain that exerts allosteric influence over the adjacent C2 domains. First, we compared C2A's Ca^{2+} binding behavior in solution with and without portions of the IDR to see if there was a direct impact on Syt I's main cellular function, Ca^{2+} sensing (Figure 2.6). In the medium C2A construct, residues 96-139 lower the thermodynamic stability of C2A in solution (relative to short C2A in reference 13) and in doing so seem to enable C2A access to conformers in which the Ca^{2+} binding sites communicate (Figure 2.6E and 2.6H). This is indicated by the modest positive cooperativity between first and second Ca^{2+} binding sites (σ ~4). Addition of residues 83-95 in long C2A, alternatively, attenuates evolved heats of Ca^{2+} binding. Long C2A still chelates Ca^{2+} as evidenced by the fact that the construct's T_m still increases upon addition of ligand (Figure 2.6C) indicating that the ITC measurement is representative of distinct binding thermodynamics. Both medium and long C2A results differ considerably from short C2A where the Ca^{2+} binding is intact, but binding sites act independently of one another, as indicated by the data being best described by a cooperativity factor of 1.

Second, we measured the allosteric impact of Syt I's IDR through examination of protein folding. For this type of measurement, we first sought conditions under which the IDR may become partially ordered and found that lipid composition of the membrane was a key factor. In the presence of a complex lipid mixture that mimics the outer leaflet of a synaptic vesicle (Figure 2.1B), we found through DSC (Figure 2.2) and NMR (Figure 2.4) measurements that the IDR experiences endotherm and chemical shift changes, respectively, consistent with IDR-synaptic lipid interactions, though in a mostly disordered structural state. With these findings in mind, we subjected short, medium, and long C2A constructs to DSC denaturation with the same synaptic vesicle mimic and found that each construct had distinct thermodynamic profiles describing their unfolding transition (Figure 2.5 and Table 2.1). This further indicates that Syt I's IDR has an allosteric impact on C2A.

That inclusion of the IDR has dramatic effects on stability and Ca^{2+} binding is not an unreasonable observation with ample supporting evidence from the literature. In a recent clinical case report, a single point mutation in Syt I was found to have a profound

impact on the patient's cognitive and motor development.[41] Such a physiological impact from a single missense mutation speaks to the sensitivity of Syt I to perturbations in performing its biological functions. Thus, inclusion of 60 disordered residues should be expected to have a functional impact. Additionally, recent in vitro studies looking at the role of the electrostatic network within the linker found missense mutations significantly interfered with Syt I's ability to mediate docking and fusion of vesicles, further highlighting the functional importance of the IDR.[5] And perhaps most pertinent is a recent study that focused on residues 80-99 in the functional inhibition of synaptic release at model neuromuscular junctions (NMJs). In this study, the authors found that treatment of NMJs with a peptide derivative of this region of Syt I resulted in significant inhibition of acetylcholine release.[6] In our study, we found that this region is also important at the level of Ca^{2+} binding, completely altering of the binding thermodynamics of C2A in solution as well as at the level of folding, weakening the C2A endotherm.

In relation to our previous work investigating the allostery of Syt I, the type of allosteric coupling between the juxta-membrane linker and C2A is different from that between C2A and C2B. It does not seem to be strictly negative or strictly positive in nature. In the case of medium C2A, the linker confers added stability with synaptic lipid and Ca^{2+}, a result more indicative of positive coupling (Figure 2.5B). In long C2A, however, the unfolding transition is much weaker, a result suggestive of negative coupling (Figure 2.5E). In the case of C2A and C2B, Ca^{2+} binding destabilized the protein construct and led to more disorder, a finding that was recently supported by elegant molecular dynamics simulations that converged on the same conclusion but with atomic-level resolution.[42] Functionally, the destabilizing interaction between C2 domains is thought to increase the available conformers so that particular subsets can mediate distinct molecular events that underlie neuronal exocytosis.[4,43] In the case of the juxta-membrane linker and C2A, however, if positive coupling is a part of its allosteric mechanism, it may be away to propagate the Ca^{2+} ligation signal away from the C2 domains to more distal locations amongst the fusion machinery. Indeed, in previous EPR measurements in full-length Syt I where a spin label was placed at residue 130, Ca^{2+} binding to the C2 domains resulted in a detectable reduction in probe mobility, consistent with the hypothesis of the linker region becoming more ordered by a positive coupling

allosteric interaction.[5] Alternatively, if the ordered state of the linker is responsible for the apparent destabilization seen in CF efflux experiments (Figure 2.7), the ordering could be propagated to the membrane surface to promote fusion of membranes.

The finding that residues 96-139 produce cooperative Ca^{2+} binding whereas 83-139 produce athermal Ca^{2+} binding can also be interpreted another way. In both the medium and long C2A constructs there is a reduced thermodynamic stability compared to short C2A (see reference 15). The resultant Ca^{2+} binding modes ranging from independent, cooperative, and athermal could indicate that the functionality of C2A fluctuates with fluctuating stability, a model that we have proposed previously.[43] In this model, allosteric modulation of C2A stability either from the N-terminal IDR or C-terminal C2B domain could tune C2A sensitivity to Ca^{2+} in a context-dependent manner for the biological purpose of promoting distinct molecular events underlying neurotransmission.[43]

2.5 Conclusion

The results presented here indicate that the IDR of Syt I exerts allosteric control over the adjacent C2 domain (Figures 2.5 and 2.6). Given that the IDR is sensitive to lipid composition (Figures 2.2 and 2.4), it is likely a key segment of Syt I for integrating organizational information coming from the underlying membrane and relaying it to the adjacent C2A domain which, being allosterically coupled to C2B, results in subsequent propagation to the very C-terminus of the protein. However, because distinct segments of the IDR confer distinct folding and Ca^{2+} binding behaviors, a more concrete rule for allosteric coupling like that defined for C2A and C2B[2] will require further investigation and may involve allosteric switching.[44]

Table 2.1. Thermodynamic Parameters of DSC Unfolding for Short and Medium C2A Constructs in the Presence of Synaptic Vesicle Mimic LUVs and Ca2+[a]

protein	ΔH (kcal/mol)	Tm (°C)	ΔCp (kcal/mol·K)	ΔS (kcal/mol·K)	ΔG37°C (kcal/mol)
short C2A	64.4 ± 0.8	71.0 ± 1.0	2.35 ± 0.02	0.20 ± 0.01	2.25 ± 0.10
medium C2A	107.5 ± 0.6	67.5 ± 0.6	4.50 ± 0.40	0.34 ± 0.01	3.30 ± 0.60

[a]Parameters shown are the average and standard deviation of four replicate measurements.

Table 2.2. Average Thermodynamic Parameters and 95% Confidence Interval Errors Obtained from Partition Function Fitting of Short and Medium C2A ITC Data[b]

	Short C2A	Medium C2A
K (M−1)	2600 ± 320	1600 ± 260
ΔH (kcal/mol)	1.27 ± 0.22	1.63 ± 0.19
σ	1.0 ± 0.1	3.7 ± 0.1
TΔS (kcal/mol)	5.76 ± 0.27	5.84 ± 0.13
ΔG (kcal/mol)	−4.49 ± 0.07	−4.21 ± 0.11

[b]Averages were obtained from three replicate measurements on each C2A construct.

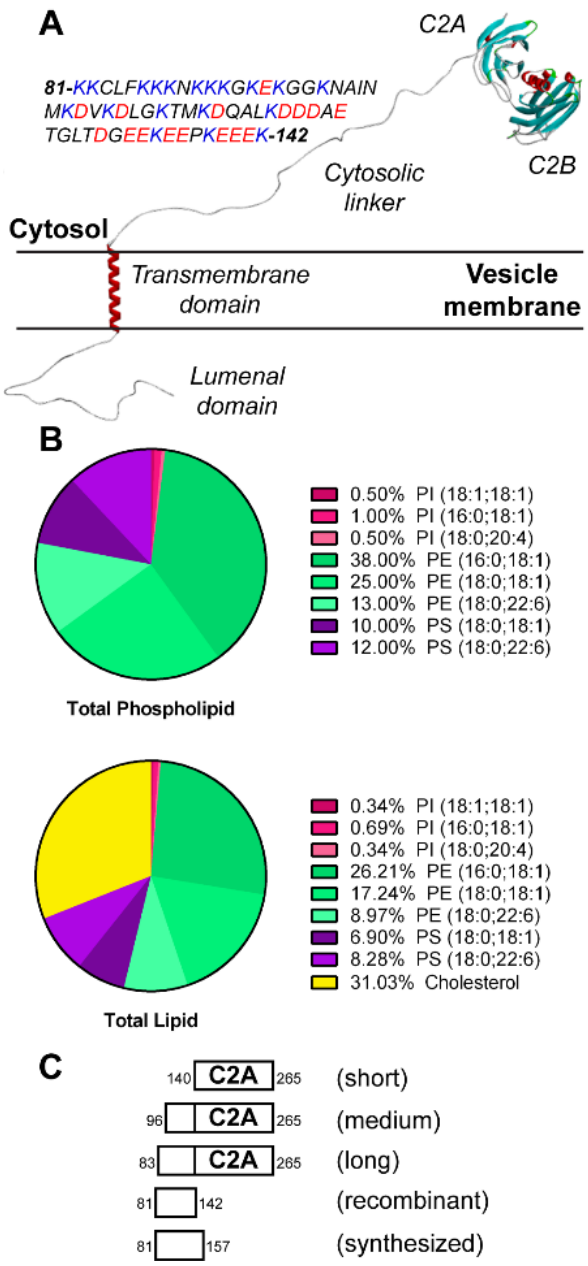

Figure 2.1. Organization of Syt I in a synaptic vesicle. (A) Syt I is a single-pass integral membrane protein. The cytosolic juxtamembrane linker region (listed amino acid sequence, based on residue numbering of UniProt entry P21579) is a polyampholyte and the focus of this study. (B) Lipid composition used to mimic the outer leaflet of a synaptic vesicle in terms of phospholipid (top) and total lipid including cholesterol (bottom). (C) We studied the impact of this IDR using short, medium, and long versions of the first C2 domain (C2A). These constructs encode residues 140−265, 96−265, and 83− 265, respectively. Recombinant refers to the IDR construct used for NMR (81−142), whereas synthesized refers to the synthesized peptide (81−157) used for DSC and dye efflux experiments

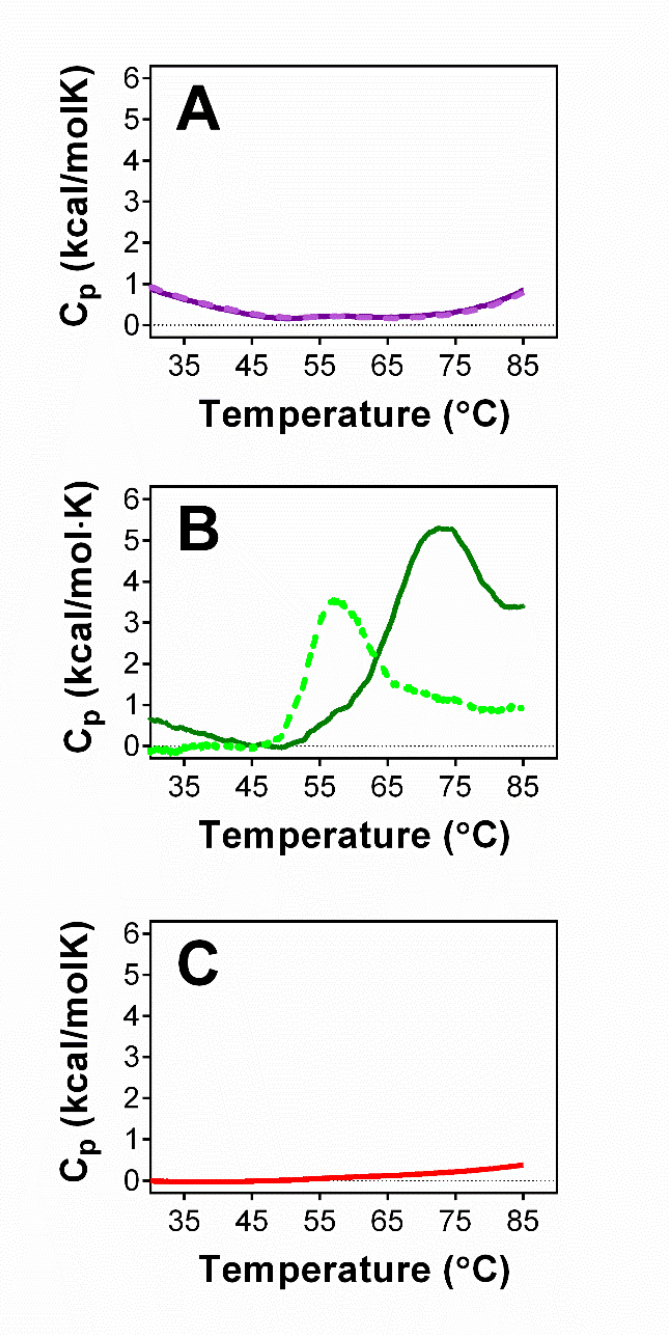

Figure 2.2. DSC denaturation of 18 μM Syt I juxtamembrane linker region. (A) In the presence of 1 mM LUVs with a simple binary 60:40 POPC:POPS lipid composition and 1 mM Ca2+, no apparent unfolding transition was present in first (solid dark purple) or reversibility (dashed light purple) temperature scans. (B) In the presence of 1 mM LUVs with a synaptic vesicle mimic lipid composition and 1 mM Ca2+, a clear endothermic transition is visible in both first (solid dark green) and reversibility (dashed light green) temperature scans. (C) Temperature scan of 1 mM synaptic lipid LUVs and 1 mM Ca2+ that does not show a prominent transition.

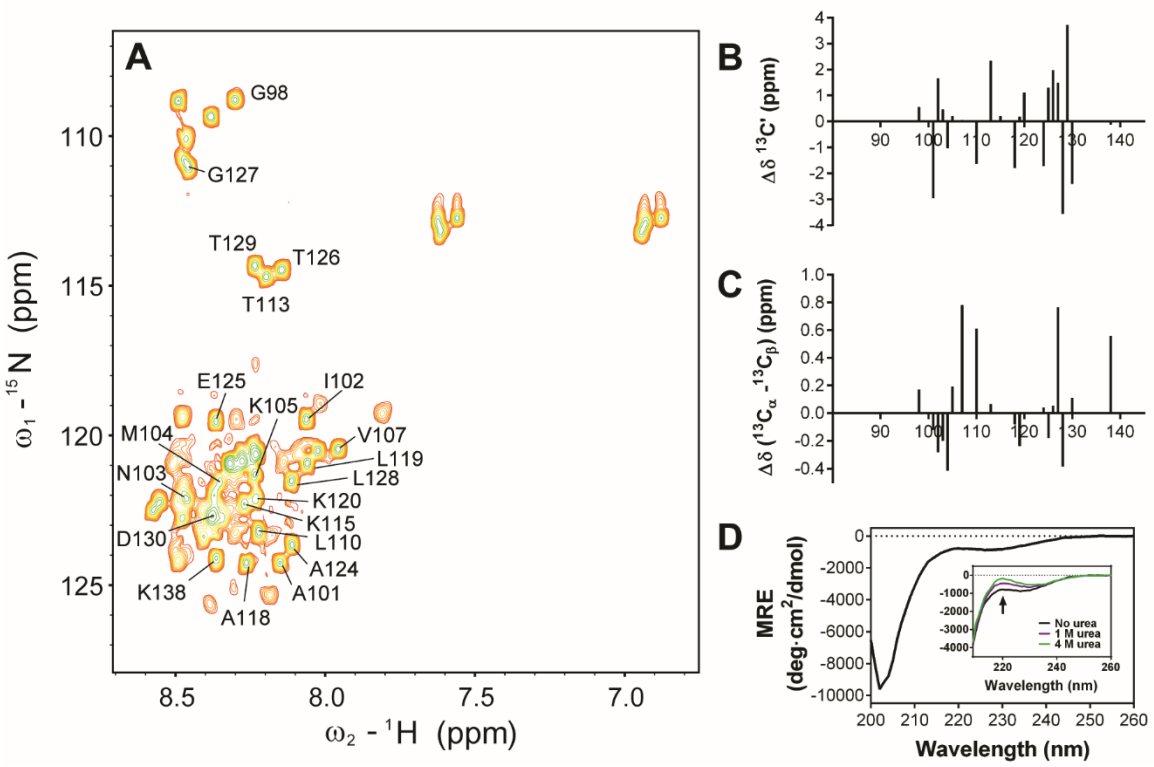

Figure 2.3. Structure of juxtamembrane linker in solution. (A) 1 H−15N HSQC spectrum of 75 μM protein in 20 mM MOPS, 100 mM KCl, and 500 μM DTT (pH 6) with 7% (v/v) D2O. (B and C) Secondary chemical shift analysis shows alternating positive and negative chemical shift differences in a majority of the residues assigned, indicative of a random coil structure in solution. (D) MRE (as calculated in eq 1) of the Syt I juxtamembrane linker in the absence and presence of urea (internal panel) that suggests hints of residual helical structure, showing further disorder-like changes in the absorption profile upon addition of a chemical denaturant.

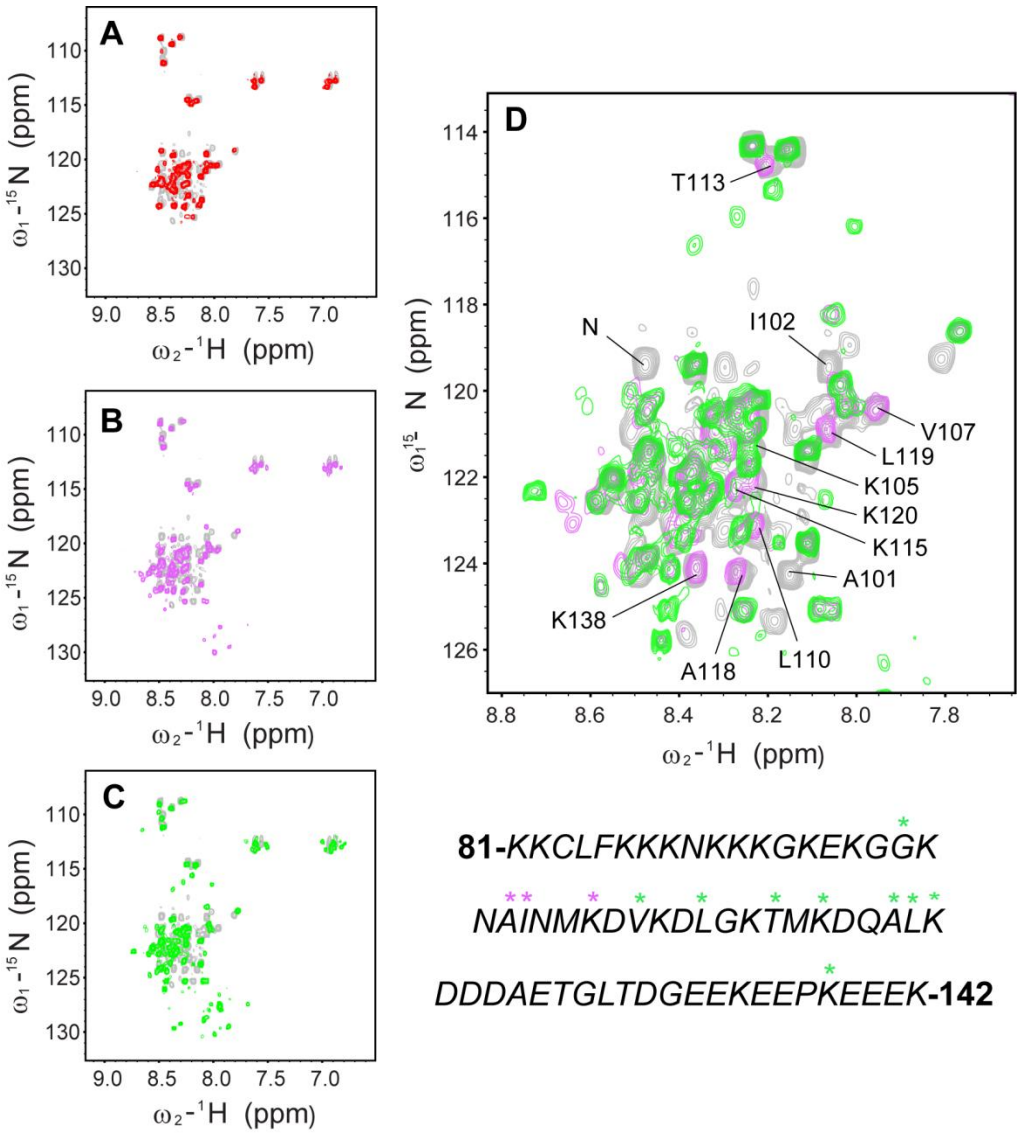

Figure 2.4. 1 H−15N HSQC spectrum of the Syt I linker region in the presence of SUVs. Above is the solution state spectrum of 30 μM protein in 20 mM MOPS, 100 mM KCl, and 500 μM DTT (pH 6) with 7% (v/v) D2O. All colored spectra are aligned with that of the juxtamembrane linker without a membrane (gray cross peaks): (A) 1 mM POPC:POPS SUVs (red overlay), (B) 1 mM synaptic lipid SUVs (purple overlay), and (C) 3 mM synaptic SUVs (green overlay). (D) Comparison of 1 and 3 mM synaptic SUV samples identifies centrally located amino acids undergoing a significant change in the local chemical environment. The amino acid sequence listed below highlights the location of residues with chemical shift perturbation at concentrations of 1 mM (purple asterisks) and 3 mM (green asterisks).

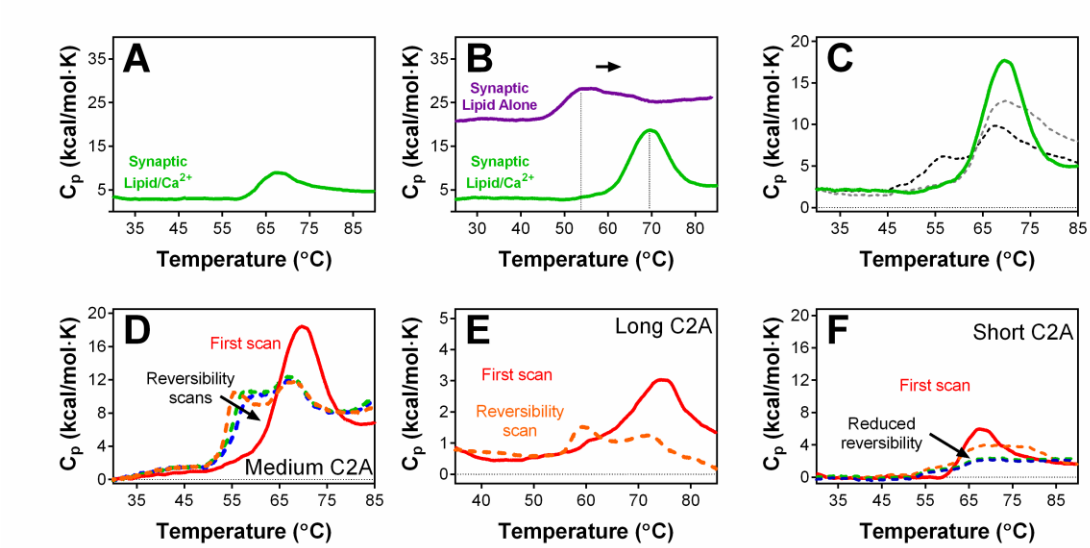

Figure 2.5. DSC comparison of 13 μM short, medium, and long C2A constructs in the presence of 1 mM synaptic vesicle mimic LUVs. (A) Short C2A denatured in the presence of LUVs and 1 mM Ca2+. (B) Medium C2A (residues 96−265) denatured in the presence of synaptic LUVs alone (purple) or synaptic LUVs and 1 mM Ca2+ (green). Note the large shift in unfolding profile (arrow) and coalescence of peaks. (C) Comparison of medium C2A (green) with the endotherm sum of short C2A and juxtamembrane linker (C2A and the first scan of linker, dotted gray; C2A and the reversibility scan of linker, dotted black). Note the added endotherm sums do not recapitulate medium C2A profiles, indicative of cooperative interactions between the two regions of Syt I that sharpen the transition. (D) Reversibility DSC scans of medium C2A. The first scan (red) shows cooperative unfolding, whereas the second (orange), third (green), and fourth (blue) scans show what is likely an annealing effect of residues 96−139 (arrow) in response to thermal reshuffling of synaptic vesicle lipids. (E) Long C2A (residues 83−265) denaturation in the presence of synaptic LUVs and 1 mM Ca2+ on the first denaturation scan (red) and the subsequent reversibility scan (orange). Note that, as seen in the medium C2A construct, the reversibility scan shows two transitions. (F) Reversibility scans of short C2A showing an absence of two transitions, a further indication that the segments of the IDR present in medium and long C2A are likely responsible for the first transition observed in panels D and E.

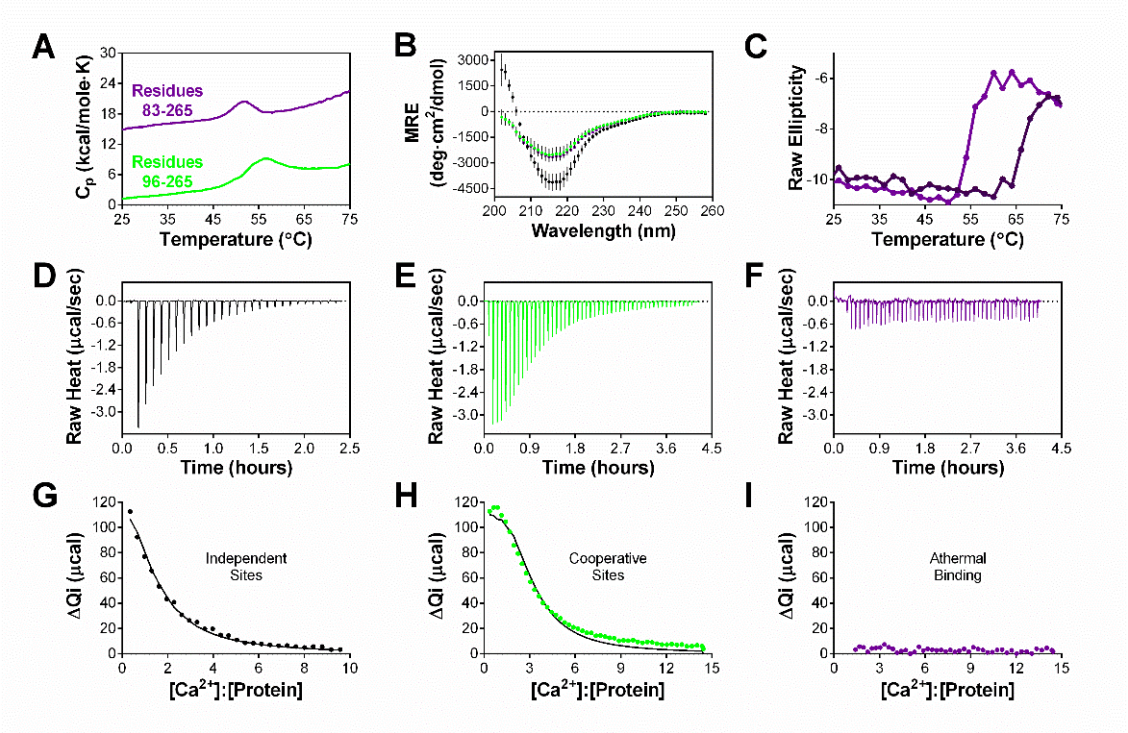

Figure 2.6. Binding and folding comparison of short (black), medium (green), and long (purple) C2A constructs without a membrane. (A) DSC comparison of 13 µM medium (residues 96−265) and 26 µM long (residues 83−265) C2A in the presence of 500 µM EGTA. Note the weaker unfolding transition of long C2A. (B) MRE (as calculated in eq 1) comparison of 15 µM short, medium, and long C2A in the presence of 500 µM EGTA. Note that because medium and long C2A constructs have a similar number of amino acids, their absorption spectra overlap considerably. (C) CD denaturation of long C2A in the absence (light purple) and presence (dark purple) of 1 mM Ca2+. Note the shift in Tm indicative of binding of Ca2+ to C2A. (D−F) Titrations of Ca2+ into (D) short, (E) medium, or (F) long C2A constructs. The short C2A construct was at a concentration of 408 µM and was titrated with 15 mM Ca2+. The injection volume was 1 µL for the first injection and then 9 µL for all subsequent injections. The medium C2A construct was at a concentration of 303 µM and was titrated with 14.5 mM Ca2+. The injection volume for medium C2A was 2 µL for the first injection and 5 µL for all remaining injections. Long C2A was at a concentration of 303 µM and was titrated with 14.5 mM Ca2+. The injection volume for long C2A was 2 µL for the first injection and 5 µL for all remaining injections. All titrations were performed at 15 °C. (G−I) When binding isotherms were fit, three distinct modes of Ca2+ binding were found.

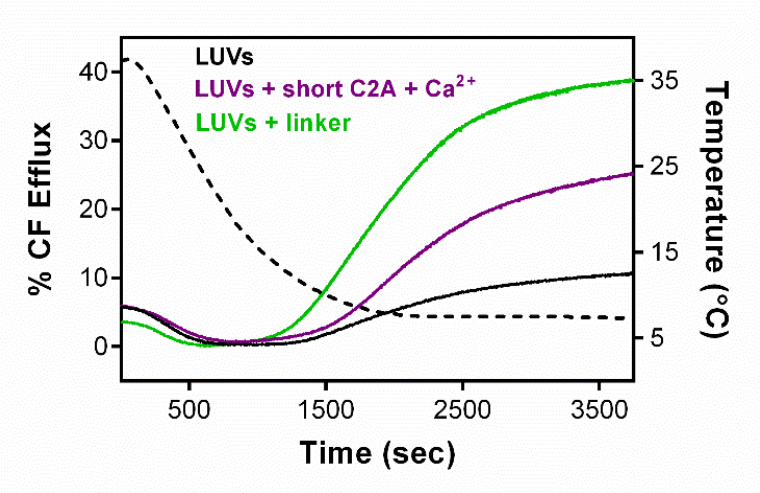

Figure 2.7. Carboxyfluorescein (CF) efflux in the presence and absence of the juxtamembrane linker and Ca2+-bound short C2A. LUVs containing 50 mM CF and consisting of a 38:38:24 POPE:SOPE:- POPS molar ratio were cooled from 37 to 7 °C (temperature indicated by black dotted line). For samples without the juxtamembrane linker, 200 μM LUVs showed a mild maximal efflux of 11% upon cooling through the vesicle phase transition temperature (solid black). However, when 8 μM juxtamembrane linker was added to 200 μM LUVs, CF efflux upon phase transitioning was enhanced (green) to a maximal efflux of 39%, a maximal percent efflux increase of 28 relative to that of the lipid-only control. To assess whether the magnitude was comparable to that of another fusion-promoting domain that inserts into the membrane, the experiment was repeated with short C2A and Ca2+, which enhanced efflux and increased maximal percent efflux by 15.

Supporting Table 2.1 (Table S2.1). Composition profiler analysis of amino acid biases in Syt I juxta-membrane linker relative to Swiss Prot 51 reference database. Results indicate the Syt I juxta-membrane linker is enriched in charged amino acids, particularly lysine, glutamic acid, and aspartic acid.

Amino acid	Propensity in sequence	P-value
Ala	Not significant.	0.371893 (>0.050000)
Arg	Not significant.	0.059816 (>0.050000)
Asn	Not significant.	0.780358 (>0.050000)
Asp	Enriched.	0.037892 (=0.050000)
Cys	Not significant.	0.942419 (>0.050000)
Gln	Not significant.	0.344251 (>0.050000)
Glu	Enriched.	0.013390 (=0.050000)
Gly	Not significant.	0.401722 (>0.050000)
His	Not significant.	0.227821 (>0.050000)
Ile	Not significant.	0.151625 (>0.050000)
Leu	Not significant.	0.392620 (>0.050000)
Lys	Enriched.	0.000000 (=0.050000)
Met	Not significant.	0.663107 (>0.050000)
Phe	Not significant.	0.342777 (>0.050000)
Pro	Not significant.	0.236968 (>0.050000)
Ser	Depleted.	0.032930 (=0.050000)
Thr	Not significant.	0.841118 (>0.050000)
Trp	Not significant.	0.399692 (>0.050000)
Tyr	Not significant.	0.163766 (>0.050000)
Val	Not significant.	0.107521 (>0.050000)

Supporting Table 2.2 (Table S2.2). Composition profiler analysis of physiochemical property biases in Syt I juxta-membrane linker relative to Swiss Prot 51 reference database.

Amino acid	Propensity in sequence	P-value
Aromatic content	Not significant.	0.060494 (>0.050000)
Charged residues	Enriched.	0.000000 (=0.050000)
Positively charged	Enriched.	0.000002 (=0.050000)
Negatively charged	Enriched.	0.000855 (=0.050000)
Polar (Zimmerman)	Enriched.	0.000000 (=0.050000)
Hydrophobic (Eisenberg)	Depleted.	0.000590 (=0.050000)
Hydrophobic (K-D)	Depleted.	0.005613 (=0.050000)
Hydrophobic (F-P)	Depleted.	0.000015 (=0.050000)
Exposed (Janin)	Enriched.	0.014378 (=0.050000)
Flexible (Vihinen)	Enriched.	0.000147 (=0.050000)
High interface prop. (J-T)	Depleted.	0.000070 (=0.050000)
High solvation poten. (J-T)	Enriched.	0.000818 (=0.050000)
Frequent in alpha hel. (N)	Enriched.	0.000278 (=0.050000)
Frequent in beta struc. (N)	Depleted.	0.000810 (=0.050000)
Frequent in coils (N)	Not significant.	0.126978 (>0.050000)
High linker propensity (G-H)	Depleted.	0.030270 (=0.050000)
Disorder promoting (Dunker)	Enriched.	0.023192 (=0.050000)
Order promoting (Dunker)	Depleted.	0.002663 (=0.050000)
Bulky (Zimmerman)	Depleted.	0.010565 (=0.050000)
Large (Dawson)	Not significant.	0.842970 (>0.050000)

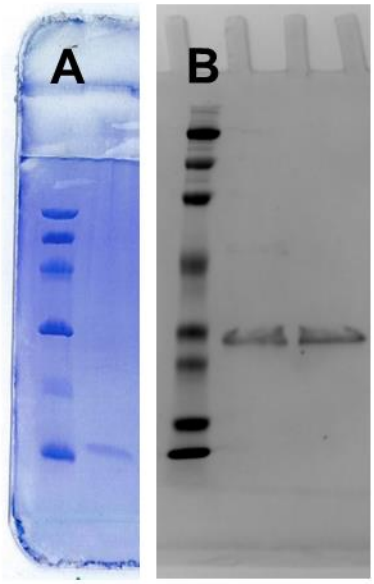

Supporting Figure 2.1 (Figure S2.1). Pure Syt I IDR and long C2A constructs. (A) SDS-PAGE of His-tagged linker region purified for NMR experiments. The first lane on the left is the ladder with molecular weights (from top to bottom) of 97, 66, 45, 30, 20.1, 14.4 kDa. In the second lane is pure linker alone at a concentration of 20 μM. (B) SDS-PAGE of pure long C2A. First lane on the left is the ladder with molecular weights (from top to bottom) of 198.8, 103.6, 57.5, 41.2, 27.7, 20.7, 15, and 6.4 kDa. Second and third lanes are long C2A without and with DTT reducing agent, respectively.

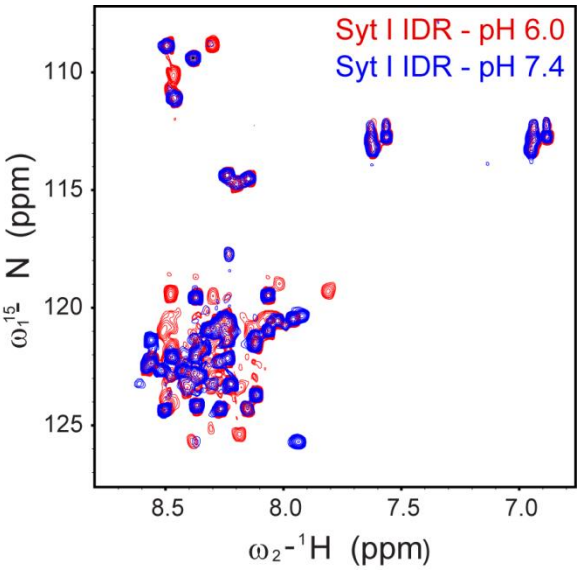

Supporting Figure 2.2 (Figure S2.2). Comparison of Syt I IDR at different pH values at 25 °C. Both NMR samples contained 60 μM IDR, 1 mM DTT, 1 mM EGTA and 7% v/v D_2O in a buffer consisting of 20 mM MOPS and 100 mM KCl. Note loss of cross peaks in sample whose pH is physiological.

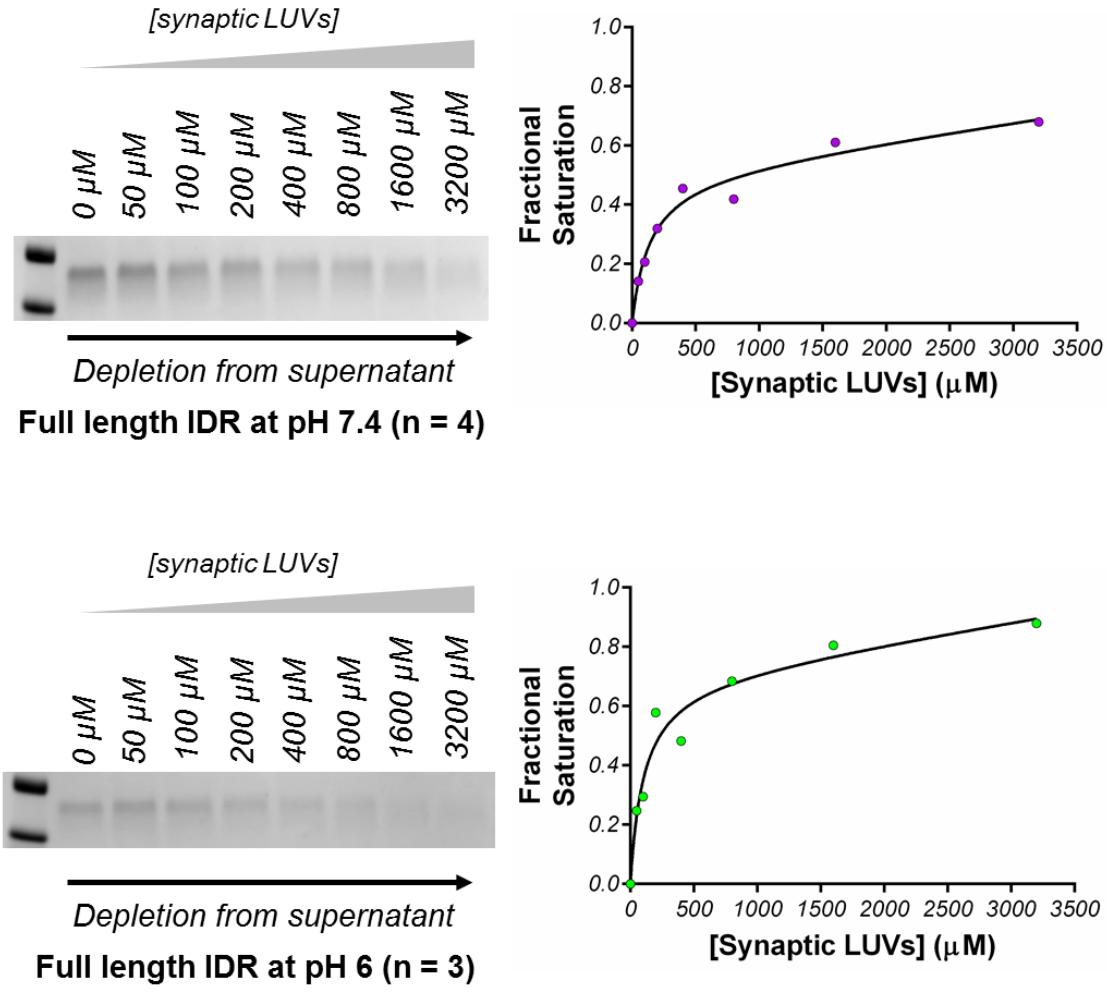

Supporting Figure 2.3 (Figure S2.3). Comparison of Syt I IDR peptide (encoding residues 81-157) binding to synaptic vesicle mimic LUVs. Co-sedimentation of Syt I IDR with LUVs was performed to assess impact of pH. After a 30 minute incubation of 15 µM Syt I IDR with increasing concentrations of LUVs, samples were spun down at 72,000 rpm in a TLA 100 rotor for 1 hour at 22 °C. Depletion of IDR from the supernatant was then used to assess binding. Shown on the left are representative gel images from four or three replicate co-sedimentation assays. On the right are the corresponding binding curves derived from each (plotted as the average of all replicates). The K_d for IDR binding to synaptic LUVs at pH 6 and 7.4 were 138±32 and 117±84, respectively.

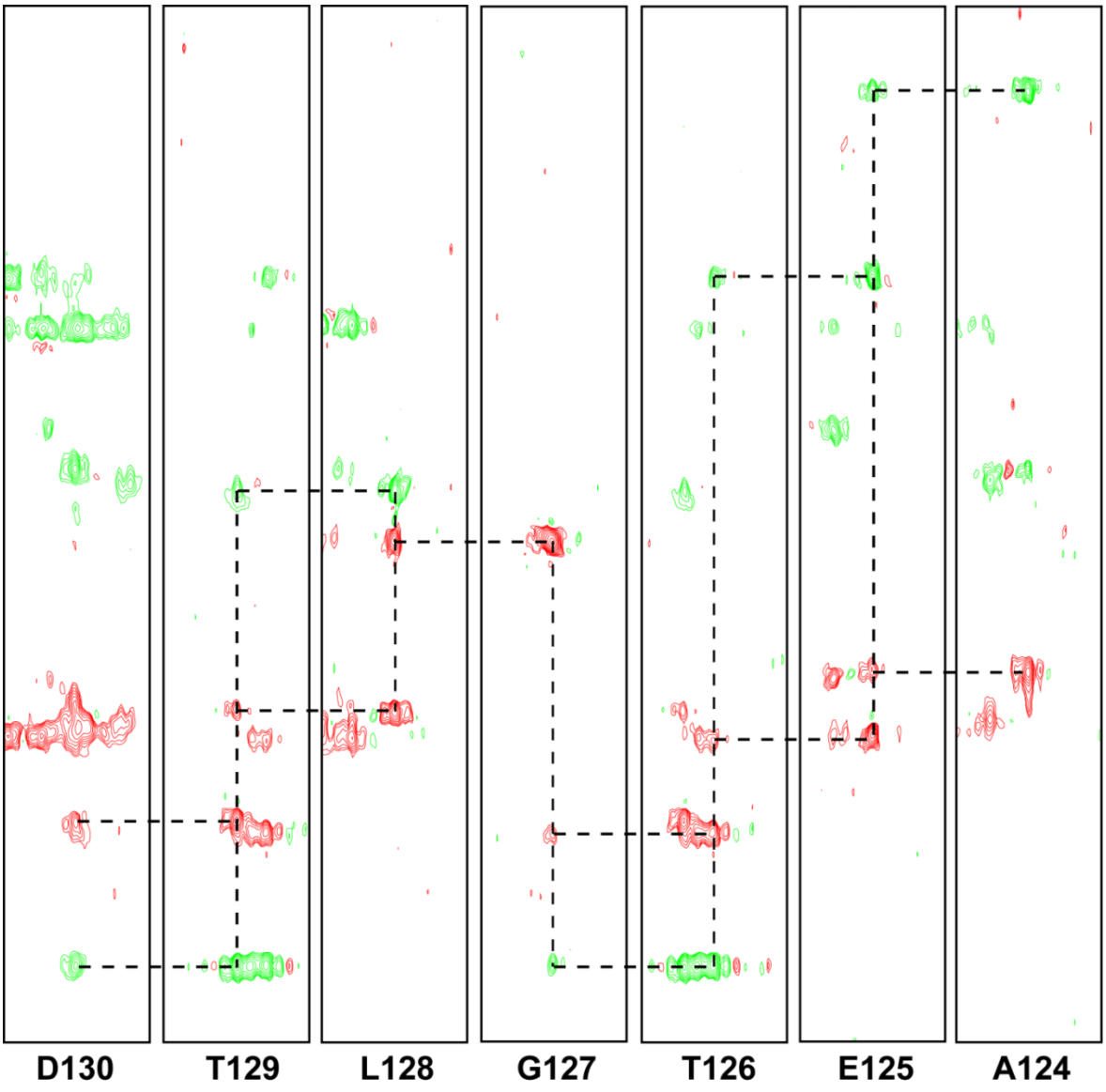

Supporting Figure 2.4 (Figure S2.4). Example HNCACB strip plots showing a walk along the peptide backbone.

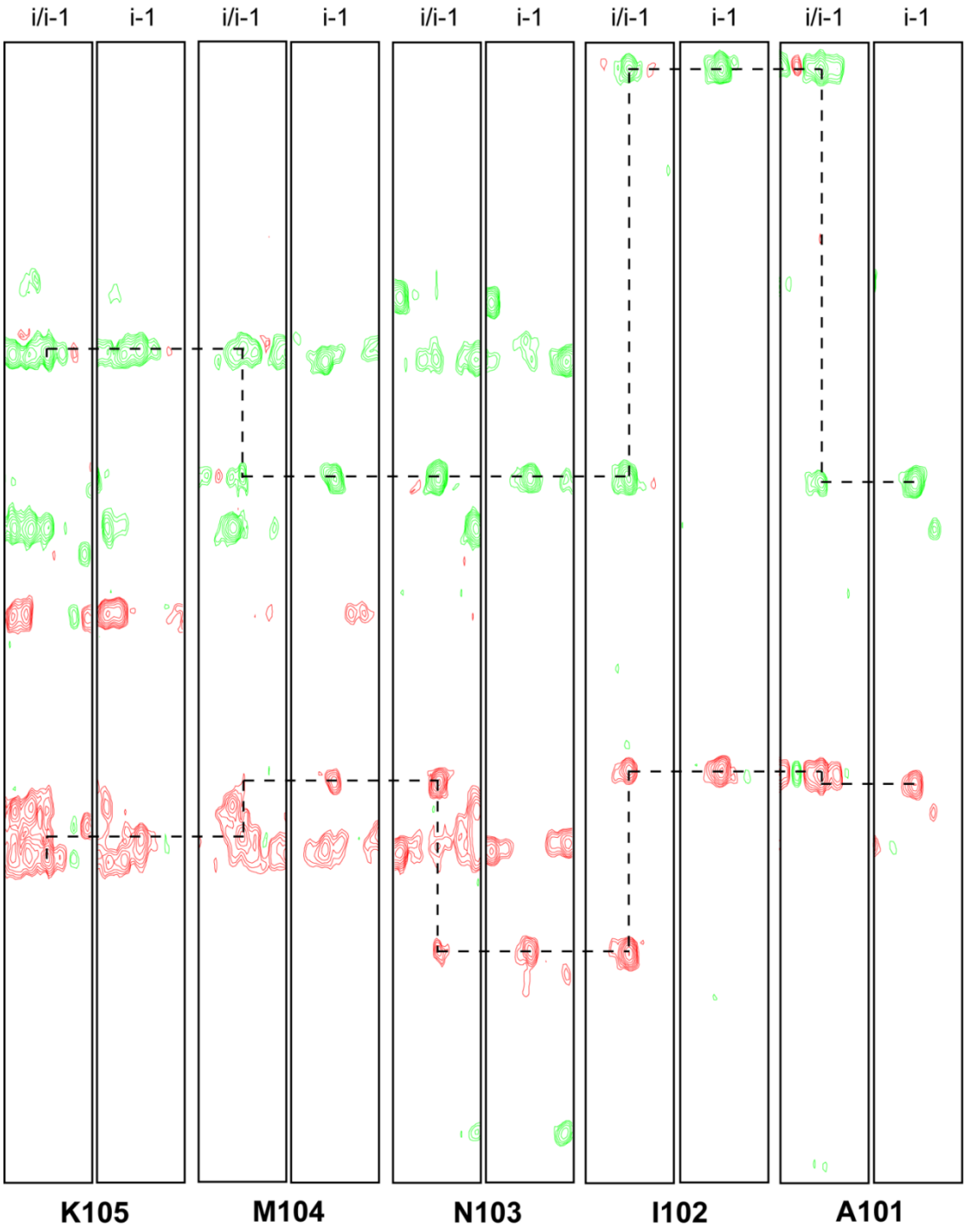

Supporting Figure 2.5 (Figure S2.5). Example HNCACB and HNCOCACB stip plots showing a walk along the peptide backbone.

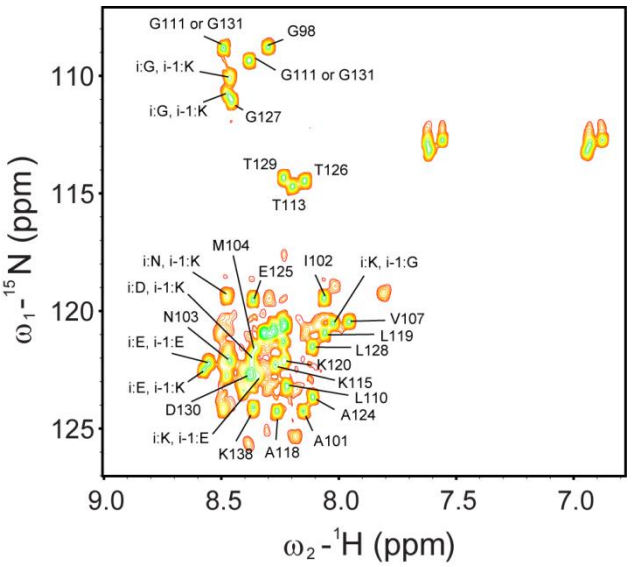

Supporting Figure 2.6 (Figure S2.6). Peaks that could and could not be unambiguously assigned.

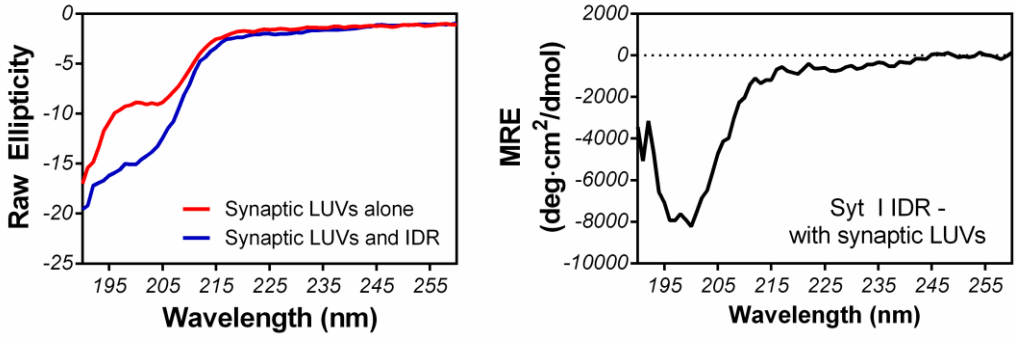

Supporting Figure 2.7 (Figure S2.7). Circular dichroism of Syt I IDR in the presence of synaptic vesicle mimic LUVs. On the left is the absorption spectrum for 1 mM synaptic mimic LUVs alone (red) and the raw, uncorrected absorption of 1 mM synaptic mimic LUVs and 15 μM Syt I IDR. The lipids absorb strongly at shorter wavelengths, likely due to high prevalence of polyunsaturated acyl chains. When corrected for the synaptic mimic LUVs (spectrum on the right), the Syt I IDR still retains significant disorder when membrane-associated. The buffer for these experiments consisted of 10 mM sodium phosphate at a pH of 7.4.

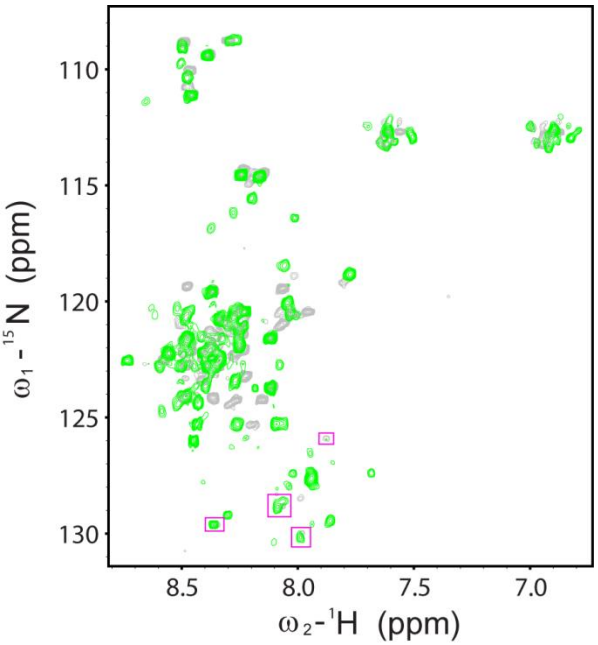

Supporting Figure 2.8 (Figure S2.8). Comparison of juxta-membrane linker with (green) and without (gray) 3 mM brain lipids at 25 °C. Note that magenta boxes indicate the cross peaks that are the same between linker alone after potential onset of aggregation and linker with synaptic vesicle SUVs.

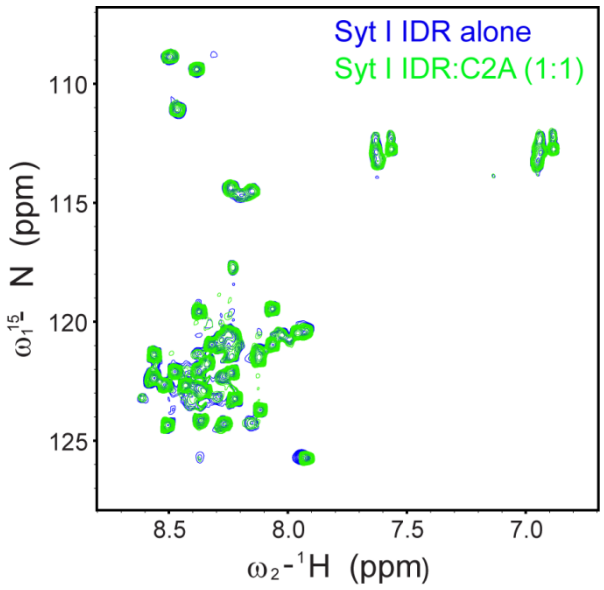

Supporting Figure 2.9 (Figure S2.9). HSQC comparison of Syt I IDR with and without short C2A at 25 °C. The Syt I IDR alone was at a concentration of 60 μM and the sample containing short C2A contained 60 μM of both IDR and C2A for a 1:1 molar ratio. Both samples contained 1 mM DTT, 1 mM EGTA and 7% v/v D2O in a buffer consisting of 20 mM MOPS and 100 mM KCl adjusted to a pH of 7.4.

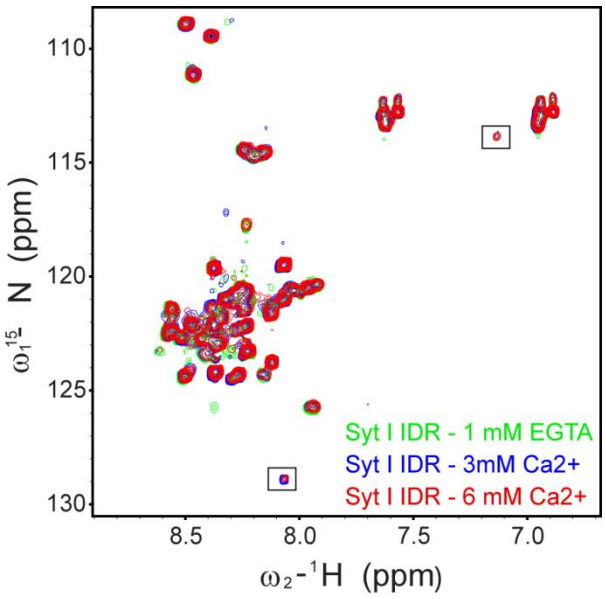

Supporting Figure 2.10 (Figure S2.10). HSQC comparison of Syt I IDR with and without Ca^{2+} at 25 °C. The Syt I IDR alone (green spectrum) was at a concentration of 60 μM and contained 1 mM DTT, 1 mM EGTA and 7% v/v D2O in a buffer consisting of 20 mM MOPS and 100 mM KCl adjusted to a pH of 7.4. Ca^{2+}-containing samples were of identical concentration, but in place of 1 mM EGTA had either 3 mM Ca^{2+} (blue spectrum) or 6 mM Ca^{2+} (red spectrum).

Chapter Three: Annexin a5 has increased affinity for phosphatidylserine and calcium ion as well as a capacity to redistribute sterol between leaflets in cholesterol-containing membranes

*Note: This chapter was reproduced in its entirety with permission from: **Annexin a5 has increased affinity for phosphatidylserine and calcium ion as well as a capacity to redistribute sterol between leaflets in cholesterol-containing membranes** Samantha R. Jaworski, Michael E. Fealey, Stephanie E. G. Kobany, et al. *Biophyscial Journal*.

3.1 Introduction

Signal transduction events involve transmission of ligand binding events from the extracellular matrix to the interior of the cell and *vice versa*. These signaling events occur through the concerted effort of numerous signaling proteins and the cooperativity of membrane lipids.[45] The role of signaling proteins in such processes are understood to a comparatively much greater extent than that of the hundreds of lipid species also present.[46] Currently, one of the most well-known mechanisms by which lipids contribute to signaling events is through domain formation. Lipid domains are areas of membrane enriched in a given lipid type due to favorable lipid-lipid interactions that minimize organizational free energy.[47] Such domains are thought to recruit and concentrate various signaling proteins as a means of initiating and propagating extracellular and intracellular signals. What is less clear about lipid domains, however, is how their differential distribution and prevalence within inner and outer leaflets of the plasma membrane are regulated and whether or not they are transversely coupled to one another to communicate a triggering cellular stimulus.

Often implicated in the formation of lipid domains are cholesterol (for its requirement to observe lipid phase separation) and certain membrane-associated proteins that accentuate lipid domain formation.[48-51] One class of proteins, the annexins, is of particular interest in this process because the basic cellular function of these proteins is unknown despite it encompassing 2% of all intracellular protein. While annexins are known to be involved in signaling and membrane trafficking events[52], the underlying mechanisms for how they mediate such diverse roles is poorly understood. Accumulating evidence suggests that there may be synergy in the phosphatidylserine (PS)- and cholesterol-modulated protein-lipid, lipid-lipid, and protein-protein interactions of

annexin a5 that give rise to subtle and responsive domain formation in model plasma membranes.[23,53,54] In such a system, domain formation results from the weakly attractive interactions between PS and cholesterol, interactions that are offset by phosphocholine's (PC) weakly repulsive interactions with both PS and cholesterol. The selectivity of annexin a5 for PS over PC is small on a general scale (roughly half of thermal energy). However, this preferential protein-lipid interaction is of the same order of magnitude as that of lipid-lipid interaction energies. Essentially, the weak selectivity of annexin a5 for PS over PC alone would not lead to protein-induced domain formation. Rather, it is the presence of cholesterol (which forms an attractive complex with PS and repulses PC) that tunes the system to be poised at the edge of lipid domain formation. At this precipice, weak protein-protein interactions, even on the order of thermal energy, are sufficient to thrust the system over the threshold from that of a nearly random dispersion of lipid and protein to one of large protein and lipid domains that form in tandem.53 The end result of annexin a5-lipid, combined with the favorable lipid-lipid and annexin a5-annexin a5 interactions at the membrane surface, is lipid domain formation with PS and cholesterol being the primary components enriched in the domain.

To add to the intricate cooperative network of protein-lipid, lipid-lipid, and protein-protein interactions, there is a eukaryotic specific signal to which most annexins bind: calcium ion (Ca^{2+}). Previously using isothermal titration calorimetry (ITC), we found that annexin a5 responds to the distribution of PS within a binary mixture of PS:PC such that its number of Ca^{2+} sites, Ca^{2+} affinities, and enthalpies associated with binding of the cation varied with mole fraction of PS.[23] The binding of Ca^{2+} by annexin a5 in the presence of PS was cooperative and the extent of cooperativity varied with mole fraction of PS (its distribution) even when the total concentration of PS was held constant. Overall, this suggests that annexins have the capacity to assimilate the distribution of PS with cellular Ca^{2+} concentration. We conclude that the binding response of annexin a5 is sensitive to lipid composition and enables a unique affinity for the membrane surface that, after initiation by Ca^{2+}, results in a signaling event that then evolves with changing cellular conditions.[23]

While the above cooperative interactions suggest a mechanism for regulation of inner leaflet domains, the question remains as to whether or not this in-plane mode of

regulation extends to the outer leaflet. One of the natural consequences of the annexin a5-induced domain formation discussed above is generation of a local lipid chemical potential difference arising from the change in lipid distribution with respect to pair wise interactions.[47] Annexin a5 binding enhances the propensity of the weakly attractive cholesterol and PS complex to cluster locally in the lateral plane of the membrane. This clustering results in an increased lipid chemical potential in one leaflet of the membrane relative to the other. This protein-driven difference in lipid chemical potential represents a possible mechanism for coupling to (and altering the distribution of) lipids in the opposed leaflet.

In the plasma membrane, the extracellular leaflet is a mosaic flickering between liquid ordered and liquid disordered lipid domains, a cholesterol-based organization unique to eukaryotes.[55] In comparison, inner leaflet lipids are nearly randomly arrayed even though also in the presence of cholesterol.[56] Cholesterol is the common component between membrane leaflets. With only a hydroxyl group in the β-3 position, cholesterol would be expected to expend the lowest energetic penalty for traversing the hydrophobic core of the membrane, making it the most likely candidate to redistribute across the bilayer to minimize the annexin a5-induced lipid chemical potential difference.[57,58] Thus, if the chemical potential driving force were sufficiently large in this context, cholesterol is predicted to flip between leaflets. Indeed, the question of cholesterol flip-flop has been investigated extensively and shown to be possible on fairly rapid time scales, with transbilayer movement and methyl-beta cyclodextrin extraction occurring within <5 seconds.[59] Such a finding would not only provide a means for thermodynamically coupling the leaflets of the membrane, but also would suggest a mechanism for protein-mediated regulation of inner and outer leaflet domains.

In the above hypothesis there are numerous reciprocal mechanisms at play, with membrane influencing protein and *vice versa*. To accommodate this complex cooperative hierarchy of interactions in testing our hypothesis, we used a combination of calorimetric and fluorescence techniques to probe inter-leaflet coupling. First, to understand how annexin a5 responds to a membrane surface containing cholesterol, we applied partition function analysis to ITC-derived binding isotherms. With an understanding of how cholesterol content modulates the annexin a5 Ca^{2+}-binding response with regard to

membrane affinity, we next examined the thermochemical impact of annexin a5 on the membrane through use of differential scanning calorimetry (DSC). Specifically, that annexin a5 induces phospholipid acyl chain ordering upon binding the membrane surface, enhancing the partitioning of cholesterol into its vicinity. Lastly, to test for annexin a5-induced flipping of cholesterol through lipid domain formation and acyl chain ordering, we used the naturally occurring cholesterol analog dehydroergosterol (DHE) employing a steady-state fluorescence quenching approach. DHE is an analog of cholesterol found in yeast that has similar physicochemical properties[60,61] including proclivity to partition into liquid-ordered phases.[62] Due to additional conjugation in rings B and C, DHE can be spectroscopically monitored allowing for study of sterol dynamics in the membrane.[63,64]

3.2 Materials and Methods

3.2.1 Reagents

Potassium chloride (KCl) was Puriss-grade. Calcium chloride dihydrate, 3-(N-morpholino) propanesulfonic acid (MOPS), 4-(2-hydroxyethyl)-1-piperazineethanesulfonic acid (HEPES), and ethylene glycol-bis(2-aminoethyl)-N,N,N',N'tetra-acetic acid (EGTA) were all Biochemika grade from Fluka Chemical Corp. Potassium iodide (KI) was Puriss-grade. All buffers were decalcified using Chelex-100 ion-exchange resin (Bio-Rad Labs) using the batch method. All lipids including 1-palmitoyl-2-oleoyl-*sn*-glycero-3-phosphocholine (POPC, 16:0,18:1PC), 1-palmitoyl-2-oleoyl-*sn*-glycero-3-phosphoserine (POPS, 16:0,18:1PS), 1,2-ditetradecanoyl-*sn*-glycero-3-serine (DMPS, 14:0,14:0PS), ergosta-5,7,9(11),22-tetraen-3β-ol (dehydroergosterol, DHE), and cholesterol (Chol) were obtained from Avanti Polar Lipids (Birmingham, AL).

3.2.2 Protein purification

Purification of annexin a5 used for experimentation was carried out as described previously.[23] Briefly, *E.coli* cells expressing rat annexin a5 were lysed by sonication and separated from insoluble protein via centrifugation. Supernatant was treated overnight with benzonuclease to facilitate removal of contaminating nucleic acid and subsequently

centrifuged and sterile filtered prior to passage over an anion-exchange column resin. Annexin a5 was separated from contaminating proteins and eluted from the anion-exchange column with buffer solutions of increasing salt gradients. Pure annexin a5 eluted from the column had its purity verified by both gel electrophoresis and NanoDrop (260/280<0.6, indicating >95% purity from contaminating nucleic acid). Concentration of annexin a5 stock solutions were determined using a NanoDrop (ThermoScientific) with a molar extinction coefficient of 21050 $M^{-1}cm^{-1}$.

3.2.3Preparation of unilamellar vesicles for ITC and DSC

Large unilamellar vesicles (LUVs) were prepared by aliquotting stock solutions of lipid in chloroform (POPC and POPS) and sterol in chloroform/methanol (4:1, v/v, Chol and DHE) into an acid-washed round bottom rotovap flask using gastight syringes (Hamilton Co., Reno, NV). A 4:1 v/v mixture of chloroform:methanol was added to the aliquoted lipid/sterol mixture to facilitate ideal mixing prior to solvent removal. Samples without cholesterol ((60:40) (POPC:POPS)) once aliquotted were dried to a thin film under a gentle stream of nitrogen gas and dried briefly under a vacuum of <20 mTorr before being lyophilized from benzene/methanol (19/1, v/v). Lipids were subsequently hydrated with decalcified 20 mM MOPS, 100 mM KCl, pH 7.5 in the dark above their gel-to-fluid phase transition temperature under argon. Samples containing sterol were dried to a thin film via roto-evaporation, where the bath temperature was 55 °C, the column temperature was between 17-19 °C, and the pressure was 406 mbar (Buchi). When solvent was evaporated, the system was purged with argon upon being brought to atmospheric pressure. This ensured minimal exposure to oxygen. To ensure complete solvent removal after roto-evaporation, samples were immediately placed under vacuum of <20 mTorr for 8-10 hours. Dried cholesterol-containing samples were then hydrated as described above. For all lipid compositions, LUVs were prepared by hand extruding a multilamellar dispersion through a sandwich of filter supports around a 0.1 μm pore size polycarbonate filter (Avanti Polar Lipids) at least 31 times. All lipids were determined by means of the phosphate assay described by Kingsley and Feigenson.[65]

3.2.4 Isothermal Titration Calorimetry

Isothermal titration calorimetry experiments to determine the binding of Ca^{2+} and POPC:POPS containing LUVs to the protein were performed on a TA Instruments Nano ITC at 15 °C. Both the Ca^{2+} and lipid titrant solutions were prepared in buffer consisting of 20 mM HEPES and 100 mM KCl at pH 7.5 that was passed through Bio-Rad 100 Chelex resin to remove cation impurities and filtered using a 0.2 μm Nalgene PES disposable filter unit. The protein was buffer exchanged into the same 20 mM HEPES and 100 mM KCl buffer using Bio-Rad 10DG disposable chromatography columns. The Ca^{2+} stock concentrations used in the experiments were verified using a BAPTA fluorescence assay (Invitrogen/Molecular Probes). The titrant lipid concentration was verified by phosphate assay according to standard protocols.[65] Heats of dilution were conducted with replicate titrations in the absence of protein and subtracted from the corresponding data sets in order to determine the binding parameters.

In reciprocal titrations, an identical concentration of pre-associated ligand was included in both the sample cell and the titration syringe in order to prevent its change during the course of the experiment. This ensured that only the enthalpy of binding of the titrated ligand was being measured. Regardless of sample composition, the total background phospholipid concentration was maintained during the Ca^{2+} titrations of annexin a5 in the presence of LUVs containing cholesterol contents ranging from (60:40):0, (60:40):10, (60:40):20, to (60:40):30 (POPC:POPS):Chol. For all lipid mixtures specified, the total phospholipid concentration of each sample was kept constant rather than having a constant total lipid (including cholesterol) concentration. This was done intentionally so that changes in measured parameters could be attributed to the amount of cholesterol itself or cholesterol's impact on POPS distribution within the membrane. If, alternatively, total lipid (phospholipid + cholesterol) was kept constant, changes in measured parameters would have the additional confounding factor of reduced POPS content. Titrations in which LUVs containing (60:40) and (60:40):10, (POPC:POPS):Chol were injected into annexin a5 in the presence of Ca^{2+} were conducted with 30uM annexin a5 in a background concentration of 2.02mM Ca^{2+} to achieve 85% saturation of the solution-state annexin a5 and reduce the enthalpic contribution of additional Ca^{2+} binding over the course of the titration. Results for the

titration of LUV's containing higher cholesterol fractions were impossible due to Ca^{2+} driven precipitation/aggregation of higher-cholesterol content LUV's during titration.

3.2.5 Quantitative Description of Complex Binding Behaviors

As described in earlier work from our lab, we employed a partition function approach to fitting of ITC binding isotherms. Most ITC systems contain fitting models that do not allow for assessment of cooperativity between sites. Because our hypothesis directly involves use of binding cooperativity, we purposefully applied partition functions which are capable of quantitatively describing complex binding behaviors. In the current study, the thermodynamic cycle for binding of annexin a5 to model membranes containing (POPC:POPS):Chol was determined analytically using isothermal titration calorimetry. To determine degree of membrane occupancy and Ca^{2+} saturation of annexin a5 in the present study, we used the derived binding partition function that we developed in our previous ITC binding study on annexin a5.[23] The partition function (Q) used in our analysis is:

$$Q = (1 + K_0[X]_f)^{n_0} + K_L[L]_f(1 + K_1[X]_f)^{n_1}(1 + K_2[X]_f)^{n_2} \qquad (3.1)$$

$$K_{app} = \frac{K_L(1+K_1[X]_f)^{n_1}(1+K_2[X]_f)^{n_2}}{(1+K_0[X])^{n_0}} \qquad (3.2)$$

where $[X]_f$ = unbound Ca^{2+}, K_0, K_1, K_2, $K_L[L]_f$ and K_{app} are the affinities of equal and independent Ca^{2+}-binding sites, the high- and low-affinity class of two equivalent and independent Ca^{2+}-binding sites in the presence of membrane, the probability of being in the membrane-associated conformational state, and the apparent affinity for membrane in the presence of Ca^{2+} respectively. The solution state population of annexin is $(1+K_o[X]_f)^{no}$ where the first term of the expansion represents the probability of being in the unbound proteins state and the rest are the probability of being in the Ca^{2+} bound state. The membrane population of annexin is $K_L[L]_f(1+K_1[X]_f)^{n1}(1+K_2[X]_f)^{n2}$ where $(1+K_1[X]_f)^{n1}$ and $(1+K_2[X]_f)^{n2}$ represent two classes of Ca^{2+} binding sites of differing affinities as well as number of sites and the first term of the expansion represents the probability of being in the membrane bound state alone. The number of solution-state

binding sites is represented above as n_0. The sites associated with the membrane bound form of annexin a5 are represented as n_1 for the high affinity sites and n_2 for the low affinity sites.

When varying lipid concentration, the fractional saturation of annexin a5 with respect to lipid (θ_L) is:

$$\theta_L = \frac{\partial Q}{\partial [L]_f} \cdot \frac{[L]_f}{Q} = \frac{K_{app}[L]_f}{1+K_{app}[L]_f} \tag{3.3}$$

When varying Ca^{2+} concentration, the fractional saturation of annexin a5 with respect to calcium ion (θ_{Ca2+}) is:

$$\theta_{Ca^{2+}} = \frac{\partial Q}{\partial [X]_f} \cdot \frac{[X]_f}{Q} \tag{3.4}$$

3.2.6 Differential Scanning Calorimetry

DMPS LUV samples either with or without 10 mole percent cholesterol were prepared for DSC scans by simultaneous stirring and degassing under vacuum prior to loading into the sample cell. This ensured removal of any trapped air bubbles that might otherwise escape solution during sample cell heating. Initial scans were carried out over a temperature range of 10-70 °C repeatedly to anneal the sample. Once DMPS LUVs alone (with or without 10 mole percent cholesterol) were annealed, the sample was removed and 2 mM Ca^{2+} was added and subsequently reloaded into the DSC sample cell for reannealing. After the second round of annealing, the sample was once again removed and annexin a5 protein was added at a final concentration of 100 μM. All scans were performed on a Microcal VpDSC at a scan rate for all DSC measurements was 10 °C/hr.

3.2.7 Preparation of DHE-containing LUVs

LUVs were prepared as described above for sterol-containing lipid samples. After overnight vacuum, these lipids were subsequently hydrated with decalcified buffer containing 20 mM MOPS, 80 mM KCl, 20 mM KI at pH 7.5 in the dark above each lipid's gel-to-fluid phase transition temperature under argon. Water used to make buffers

containing KI was boiled for 10-15 minutes (and subsequently allowed to cool to room temperature prior to buffer making) to reduce the initial amount of dissolved oxygen available for oxidizing aqueous iodide. LUVs were prepared by extruding a multilamellar vesicle dispersion through a sandwich of filter supports around a 0.1 μm pore size polycarbonate filter (Avanti Polar Lipids, Inc.) at least 31 times. LUVs then had the extra-vesicular KI removed by passing liposomes over a G-25 ultrafine Sephadex size exclusion column pre-equilibrated with isotonic buffer containing 20 mM MOPS and 100 mM KCl at pH 7.5. Complete separation of extra-vesicular KI from KI-containing vesicles was visually verified using a starch/hydrogen peroxide assay assay:

$$3\ I^-\ (aq) + H_2O_2\ (aq) + 2\ H^+\ (aq) \rightarrow I_3^-\ (aq) + 2\ H_2O\ (l) \qquad [3.1]$$

$$2\ I_3^-\ (aq) + \text{starch}\ (aq) \rightarrow \text{starch-}I_5^-\ \text{complex}\ (aq) + I^-\ (aq) \qquad [3.2]$$

Equal volumes of a 1/10 (v/v) dilution of 2M sulfuric acid/3% H_2O_2 solution and a 1/25 (v/v) dilution of 1% (w/v) starch solution were added to all test tubes of elutant (except those containing liposomes) collected from the column. The dark blue starch-I_5^- complex that formed in tubes containing extra-vesicular KI were well separated from the eluted liposomes. All lipid samples used in fluorescence experiments had their concentrations determined by a phosphate assay as done previously.[23]

3.2.8 Steady-state fluorescence

Since DHE can self-quench within lipid vesicles at >5 mole percent, we chose a low value of 2 mole percent to limit this potential artifact.(*23*) Self-quenching of DHE could result in signal artifact in flipping experiments with encapsulated KI. Instead of DHE being free to fluoresce upon flipping away from KI, the signal increase would potentially be reduced due to self-quenching in the annexin a5-induced PS-Chol domain. This would make it appear as though less flipping occurred. After samples were prepared, they were very lightly vortexed in the dark and allowed to thermally equilibrate at 22.5 °C for 15-20 minutes as DHE signal changes with temperature (Supplemental Figure 3.1). Control samples containing just LUVs or LUVs and Ca^{2+} were subjected to kinetics scans with the same excitation and emission wavelengths (ex λ = 328 nm, em λ = 374

nm) for 30 seconds, the typical length of time it takes to scan the entire wavelength range of a sample. By comparing the final and initial DHE signal, an approximate 6% photo-bleaching effect was estimated. This suggested that the change in signal due to photobleaching was minimal and not a significant detriment to signal changes brought about by protein binding and lipid rearrangement events.

The apparent variability in sample replicates could simply be the result of sample-to-sample variability in liposome concentration. Another contributing factor could be the rapid flipping of DHE between leaflets. Previous experimentation with this cholesterol mimic has shown rapid flip-flop kinetics.[59] Importantly, the kinetics of sterol flip-flop is thought to further depend on acyl chain saturation, with more rapid flip-flop occurring with greater degrees of unsaturation. Thus, by the nature of our unsaturated lipid system, the distribution of DHE between leaflets may have larger variation, giving rise to larger standard deviations between replicates.

3.3 Results

3.3.1 Binding of annexin a5 to cholesterol-containing membranes in the presence of calcium ion

The titration of annexin a5 with cholesterol-containing membrane in the presence of Ca^{2+} was precisely defined with regard to its thermodynamic parameters via ITC (Figure 3.1 and Table 3.1). Partition function formalism was utilized to define an overall binding model to Ca^{2+} and phospholipid that was constrained by its thermodynamic cycle.[23,67] Membrane binding affinities are conditional (K_{app}) as the extent of binding varies with Ca^{2+} levels as did the heat of membrane binding (ΔH_{app}) and the average binding stoichiometry of lipids per protein (z). To more easily attribute the binding phenomena to a given set of conditions, it should be noted that we attempted to saturate the protein with Ca^{2+} prior to injection of membranes of varying lipid compositions (Figure 3.1). Across all titrations of membrane into a suspension of protein and Ca^{2+}, annexin a5 was uniformly saturated with approximately 85% Ca^{2+} at the beginning of each titration. Saturation concentration was optimized with regard to the criteria of defining the highest saturation although the number of Ca^{2+} binding sites varied with

lipid composition that did not result in precipitation. Furthermore, as the presence of membrane enhanced the affinity of protein for Ca^{2+} during the course of the titration, even with the increased number of Ca^{2+} sites in the presence of membrane, one tendency offset the other such that the level of saturation varied relatively little during each of these titrations. To achieve optimization of titration conditions of membrane into a suspension of protein and Ca^{2+} or the converse titration of Ca^{2+} into a suspension of protein and membrane, some tens to nearly a hundred titrations were performed. In comparison to the prior report[23] the level of saturation was increased (i.e., high levels of saturating Ca^{2+} or membrane) in each of these coupled equilibrium systems so that the exact binding response for each scenario may be more isolated in each titration.

In the presence of saturating 2.02 mM $Ca^{2+,}$ annexin a5 bound membrane composed of (60:40):10 of (POPC:POPS):Chol LUVs has an affinity of K_{app} = 5.6 ± 2.8 mM^{-1} ($K_{D,app}$ = 180 ± 90 μM), a heat of binding of ΔH_{app} = -14 ± 1 kcal/mol, and an average binding stoichiometry of z = 58 ± 5 (Table 3.1). Compared to the absence of cholesterol, (60:40) (POPC:POPS),also under saturating Ca^{2+} conditions, annexin a5 binds the membrane with a lower affinity (K_{app} = 2.8 ± 0.6 mM^{-1} or $K_{D,app}$ = 360 ± 80 μM) but a larger heat of binding of ΔH_{app} = -16.8 ± 0.8 kcal/mol while maintaining the same average binding stoichiometry of z = 57 ± 3 (Table 3.1). The presence of cholesterol enhanced the annexin a5 binding response and the reduction of enthalpy is consistent with the co-clustering of PS and cholesterol. As the protein directly interacts with the exterior of the LUV, this was accounted for in the effective concentration of membrane in all titrations.

3.3.2 Cholesterol content of the membrane tunes annexin a5 affinity for Ca^{2+}

Annexin a5 was titrated with Ca^{2+} in the presence of (60:40) (POPC:POPS) LUVs whose cholesterol content was varied from zero to 30 mole percent (Figure 3.2 and Table 3.2). The results of these titrations are striking, as increasing the mole percentage of cholesterol dramatically increases annexin a5's affinity for Ca^{2+}. This finding has several important features associated with it. Overall, Ca^{2+} binding sites are differentiated into two distinct classes in the presence of membrane: one high affinity class (n_1) and one low affinity class (n_2). The solution state (absence of membrane) Ca^{2+}affinity has a

similar thermodynamic signature as the low affinity class of Ca^{2+} sites (n_2), consistent with the presence of membrane being necessary for the high affinity sites to bind with any detectable probability under cellular conditions. In contrast to cholesterol-free membranes, sterol resulted in an increased number of apparent Ca^{2+} binding sites within the protein. It should be noted, however, that the increased number of Ca^{2+} binding sites was restricted to the low affinity class (Table 3.2). The fact that there is a maximum number of sites suggests that the function of the protein is simply just sensitive its local environment, similar to most other proteins. In the case of enzymes, for instance, catalytic activity always has a maximum value that's dependent on external conditions such as temperature, pH, or salt. Though annexin is not an enzyme, its function (Ca^{2+} binding, which is directly related to the number Ca^{2+} binding sites the protein has) is still presumably tunable by its local environment, which in this case is the membrane and the lipids that reside within it.

The Ca^{2+} binding sites differentiate based upon the high affinity sites being entropically driven while the more numerous low affinity sites are enthalpically dominated. This thermodynamic signature was a commonality amongst the Ca^{2+} titrations in the presence of membrane and was discussed in detail previously.[23] In the presence of cholesterol, this thermodynamic signature is conserved. As in this previous work, the annexin response was sensitive to the distribution of PS such that upon varying the concentration of cholesterol, a unique Ca2+ binding response with regard affinities, enthalpies and number of sites (Figure 2G) was observed. The presence of cholesterol within the membrane enhanced the affinity of annexin a5 for Ca^{2+} to such an extent that the binding response at higher cholesterol content, nearly complete binding saturation occurs at concentrations well below maximal Ca^{2+} levels of ~20μM (Figure 3.2F).[68] The numerous low affinity sites found in the presence of PS-containing membrane upon Ca^{2+} titration may also indicate that a complex of protein with membrane is contributing to create a binding platform for Ca^{2+}. This is being more thoroughly pursued via computational simulations.

3.3.3 Lipid composition modulates entropic penalty of annexin a5 binding to membrane

In the presence of cholesterol, the entropic penalty of Ca^{2+}-saturated annexin a5 binding to membrane is reduced compared to the absence of cholesterol where $T\Delta S$ is -8.6 ± 0.8 kcal/mol in the former and -12.3 ± 0.7 kcal/mol in the latter (Table 3.1). This is consistent with cholesterol ordering the PS acyl chains as well as with PS-cholesterol forming a favorable complex as previously reported.[53] However, overall the ΔG is the same within error for either the presence or the absence of cholesterol. This is due to the enthalpy being slightly reduced in the presence of cholesterol (-16.8 ± 0.8 kcal/mol in presence compared to -14 ± 1 kcal/mol in absence), consistent with cholesterol incorporation reducing the number of PS-annexin a5 contacts, previously shown to strongly modulate the enthalpic signature of annexin a5 binding to membrane.[23]

3.3.4 Annexin a5 binding to phosphatidylserine-containing membranes results in a protein-induced lipid ordered phase consistent with a lyotropic phase transition

After assessing the impact of membrane cholesterol content on annexin a5 Ca^{2+} binding, we next examined the protein's impact on lipid distribution and phospholipid acyl chain order in the presence and absence of cholesterol. The liquid-ordered lipid phase is a manifestation of the flat, planar face of cholesterol restricting the acyl chain distribution of phospholipids.[55] Conversely, ordered acyl chains (such as that which could occur upon annexin a5 binding membrane) is predicted to accentuate cholesterol's tendency to partition into PS domains and overall modulate lipid-lipid interactions.

To address this question, acyl chain order in LUVs consisting of DMPS (14:0,14:0)PS in the absence and in the presence of cholesterol was defined via DSC. This was done by first equilibrating DMPS LUVs alone (as judged by the overlapping of successive heating gel-to-fluid lipid transitions) then removing the LUVs and adding Ca^{2+} for a second round of annealing. After this second equilibration in the presence of Ca^{2+}, the sample was again removed from the calorimeter so that protein could be added and placed back into the instrument. At each step, lipid replicates were phosphate assayed to determine the lipid concentration. Upon addition of Ca^{2+}, due to the limited permeability of the LUV to Ca^{2+}, numerous thermal cycling through the main lipid transition was necessary to reach equilibrium. DSC directly measures the enthalpy associated with the lipid gel-to-fluid phase transition. Because the free energy change at

the transition temperature is zero, the measured enthalpy is proportional to entropy ($\Delta H = T_m \Delta S$).[69,70] DMPS was selected as its T_m was well below the temperature of denaturation of annexin a5.

DMPS LUVs have a T_m and ΔH consistent with previous reports.[71,72] The addition of 2 mM Ca^{2+} to DMPS LUV did not alter the ΔH and ΔS within error compared to the absence of Ca^{2+}. The transition temperature, however, was elevated in the presence of Ca^{2+} by ~8 °C most likely from the cation complexing with the negatively charged headgroups (Table 3.3).[73-75] DMPS lipids in the absence and presence of Ca^{2+} underwent gel-to-fluid phase transitions with corresponding enthalpies of 7.19±0.05 and 7.06±0.05 kcal/mole (Figure 3.3A, purple and green lines, respectively). Intriguingly, in the presence of annexin a5 and 2 mM Ca^{2+}, the enthalpy of the DMPS-Ca^{2+} transition was significantly reduced (3.9±0.1 kcal/mole) (Figure 3.3A, green line). Because the free energy change at the transition temperature is zero, the reduction in enthalpy is directly proportional to the change in entropy. This finding indicates that annexin a5 binding decreases entropy of the membrane through acyl chain ordering, consistent with a lyotropic lipid phase transition.[76] This annexin a5-induced dehydration of lipid head groups would reduce lipid headgroup area, constricting the acyl chains, imparting order and altering lipid-lipid interactions.[67] As a further validation of this mechanism, a binary lipid mixture of DMPC:DMPS (similar to that used in ITC binding measurements) was subjected to the same series of DSC scans. Though the endotherm profile becomes more complex as a result of having two phospholipid species, a substantial reduction in enthalpy and entropy of the transition were still seen (Supplemental Figure 3.2 and Supplemental Table 3.1). Such findings are again consistent with annexin a5 binding inducing acyl chain ordering of DMPS lipids.

3.3.5 Cholesterol attenuates annexin a5-induced ordering of acyl chain

To next assess the effect of cholesterol on acyl chain ordering, LUVs consisting of DMPS in which 10 mole percent was now cholesterol were studied using DSC. Consistent with cholesterol's ordering impact on phospholipids[55,77,78], the addition of cholesterol lowered the enthalpy of the DMPS-Ca^{2+} gel-to-fluid phase transition (from 7.06±0.05 kcal/mole to 4.9±0.2 kcal/mole) (Figure 3.3B, purple and blue lines,

respectively). Significantly, cholesterol sensitizes the membrane surface to accentuate the impact of Ca^{2+} on ordering PS acyl chains. Regardless, in the presence of annexin a5 and Ca^{2+}, the enthalpy of the transition decreased relative to DMPS and cholesterol alone (from 7.03±0.05 kcal/mole to 6.0±0.1 kcal/mole) (Figure 3.3B, purple and green lines, respectively lines). This is consistent with an ordering of the DMPS acyl chains upon annexin a5 binding, but indicates that the presence of even small amounts of cholesterol can sensitively attenuate lipid-lipid interactions and the impact of Ca^{2+} and protein upon them.

3.3.6 Binding of annexin a5 flips the cholesterol analog DHE from the inner to outer leaflet of LUVs

After examining both the impact of cholesterol on annexin a5 binding of Ca^{2+} and annexin a5 binding on lipid order, we next asked whether or not these reciprocal interactions could influence the trans-leaflet distribution of sterol. To test the hypothesis that annexin a5-induced lipid rearrangements have the potential to flip the cholesterol mimic, DHE, LUVs consisting of (60:40):2:8 (POPC:POPS):DHE:Chol were prepared. These liposomes were hydrated with buffer containing a KI contact quencher. Because iodide is water soluble and negatively charged, it only has the capacity to quench the fluorescence of DHE molecules present in the inner leaflet of the bilayer. When annexin a5 is added to a colloidal suspension of vesicles containing cholesterol in the presence of Ca^{2+}, domain formation occurs.[53] Moreover, some degree of acyl chain ordering should result (Figure 3.3). Both are predicted to create a local lipid environment favorable for DHE partitioning. If DHE partitioning occurs through flipping from the inner to outer leaflet, the fluorescent signal is expected to increase (Figure 3.4 *top*).

When the above experiment is performed, increasing the concentration of annexin a5 in a background of 100 μM Ca^{2+} results in substantial increases in DHE fluorescence intensity (Figure 3.4 *bottom*, left and middle panels). Because the binding of annexin a5 to membranes containing (POPC:POPS):Chol seems to become increasingly entropically driven with increasing cholesterol content, there is the possibility that an increase in DHE signal upon annexin a5 binding is partly due to dehydration of the membrane surface. Indeed, when the same experiments in Figure 4 were carried out in the absence of

encapsulated quencher, an increase in DHE intensity was seen (Figure 3.4 *bottom*, right panel). However, the change in magnitude was not as great as that seen with encapsulated quencher (~5-fold change without quencher; ~10-fold change with quencher). Because the magnitude of signal change in the dehydration control does not recapitulate the data with encapsulated quencher, the remaining signal change is likely due to flipping of DHE to the outer leaflet of the LUV membrane. A portion for this signal increase is also likely to stem from the concurrent flipping of cholesterol. This is inferred from the fact that diluting DHE with cholesterol in a POPC:POPS membrane results in further increases in DHE fluorescence (Supplemental Figure 3.3). This measurement indirectly supports annexin a5-induced flipping of cholesterol and further supports our hypothesis that annexin a5 promotes transleaflet redistribution of sterol. Overall, signal seems to reach a maximum representing, perhaps, a point where the equilibrium is strongly shifted in the direction of DHE on the outer leaflet. It is not clear that this apparent sterol flipping is a property of all annexin isoforms. When we repeated the same DHE experiment with annexin A2, for example, we did not measure increased DHE fluorescence (Supplemental Figure 3.4). Collectively, these results suggest different isoforms may or may not have a propensity to redistribute sterol between leaflets.

3.4 Discussion

Annexins are a large, ubiquitously distributed family of intracellular membrane binding proteins.[79] They are as ancient as eukaryotic life with their earliest homologs dating back to the oldest eukaryotic cell fossils found, 1.5 billion years ago. Such an evolutionary history suggests a fundamental role in cells utilizing membrane-bound organelles where their need is accentuated by their diversifying into a many member, highly homologous family.[80] It has been exceedingly difficult to assign a specific biological role to annexins as they lack enzymatic function, negating a trail of reactants and products that might suggest functionality. Thus, their persistence and abundance in eukaryotic cellular evolution emphasizes their paramount functional importance. Here we propose models for such mechanisms, particularly in the regulation of membrane lipid distribution and potentially Ca^{2+}-related signal transduction.

Our results suggest that annexin a5 binding to PS and cholesterol-containing membranes facilitates trans-leaflet flipping of DHE. The thermodynamic driving force for this flipping event is likely derived from several sources, one of which is the chemical potential difference that results from clustered PS. In our membrane system, where each leaflet has the same lipid composition, the only source of lipid chemical potential difference is induced by annexin a5's interaction with the membrane surface. Because of cholesterol's weak preference for PS over PC[53], this clustering of PS by annexin a5 promotes partitioning of more sterol into the protein-induce domain. Another driving force for the observed trans-leaflet sterol redistribution is an annexin a5-induced ordering of lipid acyl chains. When annexin a5 binds to PS, the thermodynamic signature garnered from both ITC and DSC is consistent with dehydration of headgroups and a consequent reduction of phospholipid area. This results in an ordering of acyl chains due to tighter packing of lipids. Because of cholesterol's tendency to associate with more ordered acyl chains, this annexin a5-induced ordering increases the favorability with which cholesterol interacts with PS's acyl chain and, consequently, increases the likelihood of cholesterol recruitment from the opposite leaflet.

When considering the data as a whole in the context of biological function, we assembled an intricate and novel model for annexin a5 function: termination of membrane-localized signal transduction events through modulation of lipid organization. This model for function is formulated based on several convergent observations, the first of which relates to the organization of lipids in the inner leaflet. Normally, lipids of the inner leaflet are nearly randomly distributed.[56] This arrangement of lipids with respect to each lipid's chemical activity maximizes chemical potential change and thus the ability to harness the potential work implicit in the free energy change. Such a free energy change can be channeled to achieve a defined biological outcome. When annexin a5 binds PS in cholesterol-containing membranes, it demixes these weakly attractive lipid complexes enhancing the propensity for local phase separation of lipid. In a truly phase separated system, the chemical potentials equate between the phases thus eliminating the potential to accomplish work. In essence, annexin a5-induced lipid reorganization has the capacity regulate or suppress membrane-mediated signaling. The second observation in support of a signal-terminating model comes from the ITC measurements of Ca^{2+} and membrane

binding affinities. With increasing cholesterol content, annexin a5 becomes increasingly sensitive to the signaling cation. There are many cytosolic signal transduction proteins that rely on Ca^{2+} for activation. To ensure appropriate control of activation, annexin a5's increased affinity would effectively compete for the binding of this second messenger, and, as a result, attenuate the stimulatory signal by shortening its flux duration. This model is based purely on comparison to other in vitro systems involving membrane and Ca^{2+} binding proteins, such as the C2 domains of protein kinase C.[35] If annexin a5's affinity for Ca^{2+} increases from a few micromolar to nanomolar as a result of local increases in cholesterol, it could be better situated to compete for free cytosolic Ca^{2+} compared to C2 domains with micromolar affinity. In this way, annexin a5 would potential participate in a Ca^{2+} buffering role. Additionally, if annexin a5 facilitates cholesterol flip-flop upon inner leaflet PS-enriched domain formation, these sites of protein association will result in increased local cholesterol content. Thus, annexin a5 affinity for Ca^{2+} and membrane, results in an ever evolving feedback mechanism to regulate annexin a5 affinity for and organization of the membrane surface (Figure 3.2F).

Much like the simple biochemical argument given for potential Ca^{2+} binding competition, with annexin a5's increased affinity for Ca^{2+} its membrane occupancy will also be greatly enhanced. If this affinity is greater than that of other membrane and Ca^{2+}-binding protein as measured in vitro, annexin a5 compete for or displace from the membrane other associating proteins. In this way, annexin a5's membrane-responsive character allows it to prevent or terminate signaling that requires other peripheral proteins to associate with PS. Annexin a5 sensitivity to Ca^{2+} at high stimulatory intracellular Ca^{2+} levels (~20μM as noted above) is defined by lipid composition prior to the Ca^{2+}-influx.[81-83] These same delineated characteristics that are amenable to membrane-based signal modification are also consistent with annexin a5 based cellular membrane repair.[84,85] In our last proposed model for function, we consider the annexin a5-induce flipping of sterol. With annexin a5's ability to drive cholesterol flip-flop, there is the potential for Ca^{2+}-mediated domain formation on the inner leaflet to consequently deplete (albeit on a local level) the cholesterol content of the outer leaflet. If the outer leaflet cholesterol is participating in a liquid-ordered/liquid-disordered phase modulation into which stimulatory proteins are preferentially partitioned, the higher cholesterol containing

liquid-ordered phase and its associated proteins therein may be disseminated. This model would result in an elimination of the stimulatory protein-protein association in the outer leaflet (Figure 3.5). Signal transduction through several pathways often initiates a Ca^{2+} influx as a down-stream second messenger.[86-88]What this flipping model offers is a rationale for the coupling of intracellular signaling events, that were initiated via extracellular mechanisms, back to the extracellular leaflet of the membrane. In essence, annexin a5-mediated flipping of sterol functions as a sensitive negative feedback loop for signal transduction events in the cell. With the tight control of intracellular Ca^{2+} via transport into the sarcoplasmic reticulum[89], out of the cell via efflux pumps[90], and Ca^{2+}-buffering proteins91, rapid removal of Ca^{2+} from the cytosol would theoretically reverse annexin a5-induce flip-flop and could reset the local cholesterol distribution and prime the cell for new signaling events.

3.5 Conclusion

Within a biological context, the data presented here have strong implications for how annexins a5 may regulate membrane domains and their function in signal transduction. Annexin a5's sensitivity to membrane cholesterol, wherein increasing concentrations of sterol dramatically increase affinity for Ca^{2+} (Figure 3.2), points to a model of second messenger attenuation; the high potential for sequestration of the signaling ion may act to prevent its subsequent activation of downstream effectors. Moreover, with annexin a5's increased affinity for membrane (Figure 3.1) and propensity to demix PS in the presence of cholesterol[53], the peripheral protein could potentially attenuate signal transduction further by displacing other cytosolic proteins that require membrane association with anionic lipid for activation. In addition to influencing these inner leaflet mechanisms for modulation of signal transduction, annexin a5's binding to and reorganization of cytoplasmic lipids could propagate to the outer leaflet through trans-leaflet reorganization of cholesterol. Through a concurrent demixing of PS53 and lyotropic ordering of lipid acyl chains (Figure 3.3), annexin a5 binding creates a local lipid environment suitable for enhanced partitioning of cholesterol from the opposing leaflet (Figure 3.4). In this functional model outer leaflet lipids, whose clustering is

sensitive to cholesterol, could have their organization perturbed and, as a consequence, so would signaling molecules that preferentially partition there (Figure 3.5).

Table 3.1. Thermodynamic parameters for the binding of membrane to annexin a5 in the presence of saturating Ca^{2+}. Measurements were made using a TA Instruments NanoITC. K_L values estimated from K_{app} values and fit parameters for calcium binding. Values of z represent the number of lipid molecules per protein. Errors are reported as 95% confidence interval.

	(60:40) (POPC:POPS)	(60:40):10 (POPC:POPS):Chol
z	57 ± 3	58 ± 5
K_{app} (mM^{-1})	2.8 ± 0.6	5.6 ± 2.8
$K_{d,app}$ (uM)	360 ± 80	180 ± 90
ΔH (kcal/mol)	-16.8 ±0.8	-14 ± 1
TΔS (kcal/mol)	-12.3 ± 0.7	-8.6 ±0.8
ΔG (kcal/mol)	-4.5 ± 0.1	-4.9 ± 0.3
$K_{L\ (hi\ only)}$ (M^{-1}) est.	0.16 ± 0.2	11000 ± 10000

Table 3.2. Thermodynamic parameters for the binding of Ca^{2+} to annexin a5 in both the presence and absence of saturating membranes. Measurements were made using a TA Instruments NanoITC. Errors are reported as 95% confidence interval.

		Calcium Binding with a background of saturating membrane present			
	Calcium binding in absence of membrane	(60:40) (POPC:POPS)	(60:40):10 (POPC:POPS): chol	(60:40):20 (POPC:POPS): chol	(60:40):30 (POPC:POPS): chol
n_1	-	3.6 ± 0.1	1.2 ± 0.2	1.8 ± 0.1	1.9 ± 0.1
K_1 (mM^{-1})	-	120 ± 40	590 ± 380	1,200 ± 350	84,000 ± 54,000
K_{d1} (uM)	-	8.6 ± 3.0	1.7 ± 1.0	0.09 ± 0.01	0.012 ± 0.008
ΔH_1 (kcal/mol)	-	2.0 ± 0.5	1.8 ± 0.7	2.4 ± 0.7	1 ± 0.3
$T\Delta S_1$ (kcal/mol)	-	8.7 ± 0.3	9.5 ± 0.3	11.7 ± 0.4	11.4 ± 0.4
ΔG_1 (kcal/mol)	-	-6.7 ± 0.2	-7.6 ± 0.4	-9.3 ± 0.5	-10.4 ± 0.7
n_2	5.0 ± 0.1	10.3 ± 0.7	16.5 ± 0.6	14.6 ± 0.8	12.4 ± 0.4
K_2 (mM^{-1})	3.1 ± 0.16	5.9 ± 0.6	23 ± 4	160 ± 50	760 ± 200
K_{d2} (uM)	330 ± 40	170 ± 16	43 ± 8	6.3 ± 0.05	1.3 ± 0.4
ΔH_2 (kcal/mol)	-2.4 ± 0.2	-25.7 ± 0.7	-30.8 ± 1.2	-28.3 ± 0.7	-29.5 ± 0.5
$T\Delta S_2$ (kcal/mol)	2.2 ±0.2	-20.7 ± 0.7	-25 ± 1	-21.4 ± 0.4	-21.8 ±0.3
ΔG_2 (kcal/mol)	-4.6 ± 0.1	-4.97 ± 0.06	-5.8 ± 0.1	-6.9 ± 0.2	-7.8 ± 0.16

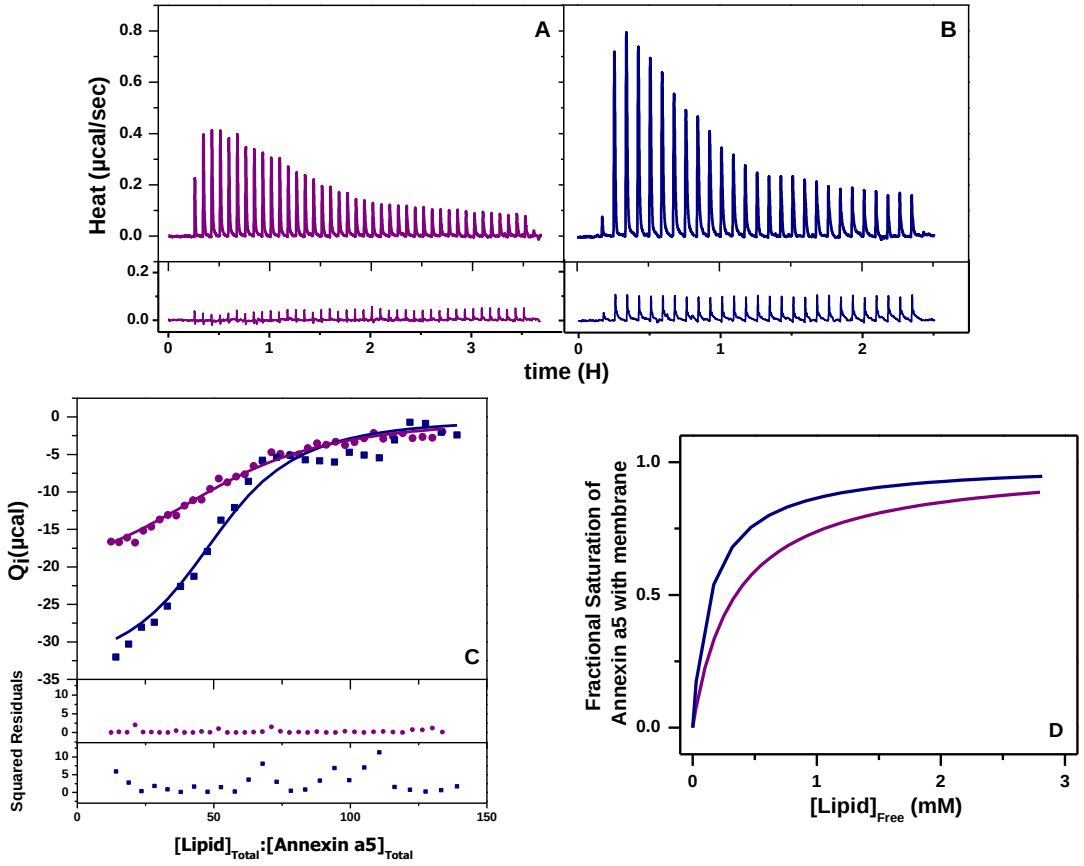

Figure 3.1. Raw heats of binding obtained from titrating LUVs into annexin a5 and Ca^{2+}. Measurements were made using a TA Instruments NanoITC. A. The titration of 31 µM annexin a5 with 16 mM total lipid as LUVs made of a (60:40) mixture of (POPC:POPS) in the presence 2.02 mM Ca^{2+} of at 15°C. (Above) Raw ITC data. (Below) Heat of dilution data (control). B. Results of the titration of 28 µM annexin a5 with 12.5 mM total lipid as LUVs made of a (60:40):10 mixture of (POPC:POPS):Chol in the presence 2.04 mM Ca^{2+} at 15°C. (Above) Raw ITC data. (Below) Heat of dilution data (control). C. Integrated heats of binding as a function of lipid/protein ratio where the purple circles represent the (60:40) mixture of (POPC:POPS) and the blue squares represent the (60:40):10 mixture of (POPC:POPS):Chol. (Below) Residuals for the corresponding models used to fit the integrated heats of bindings. D. Binding isotherms as a function of free lipid in the presence of Ca^{2+} calculated using the binding affinity values from Table 1.

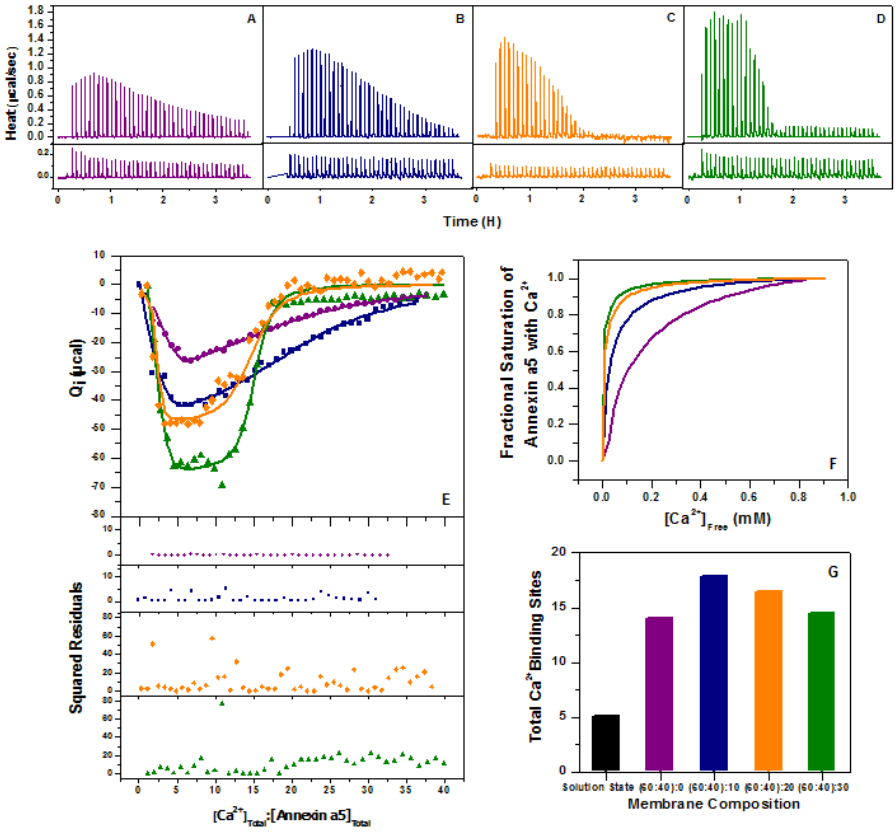

Figure 3.2. Raw heats of binding obtained from titrating Ca^{2+} into annexin a5 and LUVs. Measurements were made using a TA Instruments NanoITC. A: The titration of 30 µM annexin a5 with 3.78 mM Ca^{2+} in the presence of 3.18 mM total lipid as LUVs made of a (60:40) mixture of (POPC:POPS) at 15°C. (Above) Raw ITC data. (Below) Heat of dilution data (control). B: The titration of 30 µM annexin a5 with 4 mM Ca^{2+} in the presence of 3.56 mM total lipid as LUVs made of a (60:40):10 mixture of (POPC:POPS):Chol at 15°C. (Above) Raw ITC data. (Below) Heat of dilution data (control). C: The titration of 30 µM annexin a5 with 4 mM Ca^{2+} in the presence of 4.08 mM total lipid as LUVs made of a (60:40):20 mixture of (POPC:POPS):Chol at 15°C. (Above) Raw ITC data. (Below) Heat of dilution data (control). D: The titration of 30 µM annexin a5 with 4 mM Ca^{2+} in the presence of 4.57 mM total lipid as LUVs made of a (60:40):30 mixture of (POPC:POPS):Chol at 15°C. (Above) Raw ITC data. (Below) Heat of dilution data (control). E: Integrated heats of binding as a function of ligand/protein ratio where the purple circles represent the (60:40) mixture of (POPC:POPS), the blue squares represent the (60:40):10 mixture of (POPC:POPS):Chol, the orange diamonds represent the (60:40):20 mixture of (POPC:POPS):Chol, and the green triangles represent the (60:40):30 mixture of (POPC:POPS):Chol. (Bottom) Residuals for the corresponding models used to fit the integrated heats of bindings. F. Binding isotherms as a function of free Ca^{2+} in the presence of membrane calculated using the binding affinity values from Table 2. G. Total number of Ca^{2+} binding sites (high and low affinity) as a function of changing membrane composition.

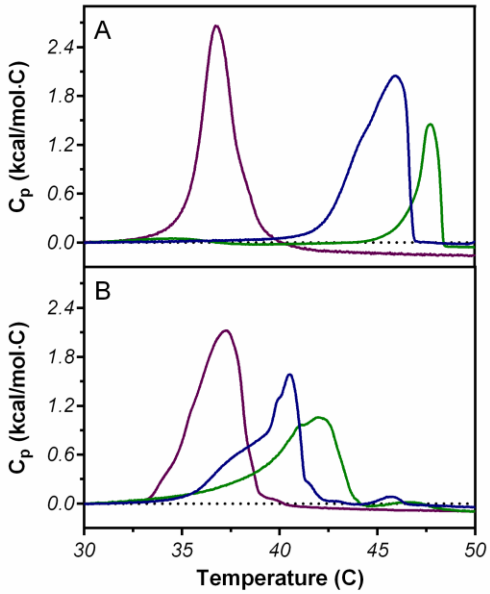

Figure 3.3. DSC measurement of DMPS gel-to-fluid phase transitions. Measurements were performed using a Microcal VpDSC. Endotherms of LUVs alone (purple), LUVs and Ca^{2+} alone (blue), and LUVs, Ca^{2+} and annexin a5 (green). A: DMPS LUVs. Note the dramatic decrease in endotherm area (corresponding to DMPS transition enthalpy) upon annexin a5 saturation, indicative of a protein-induced lyotropic phase transition and ordering of DMPS acyl chains. Similar results were seen for DMPS:Chol (90:10) samples in B.

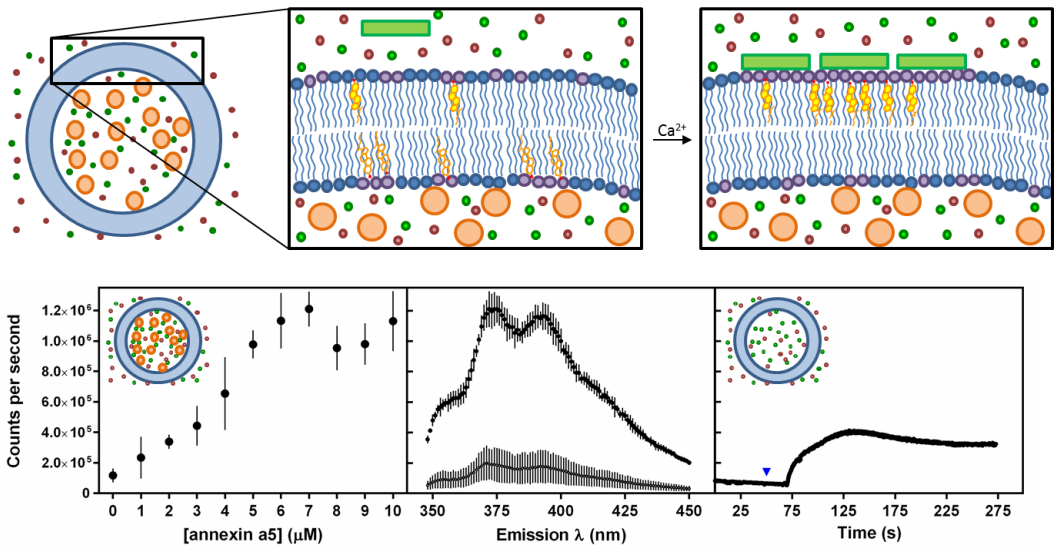

Figure 3.4. Annexin a5-induced flipping of DHE away from intra-vesicular KI. Measurements were performed on a Horiba Jobin Yvon Fluorolog 3 steady-state spectrometer. (Top) Diagram of quencher-containing LUVs wherein DHE molecules on the inner leaflet are contact quenched (transparent sterols) by KI (orange spheres) and DHE molecules in the outer leaflet are not (yellow sterol). Annexin a5 (green rectangles) in the presence of calcium demixes PS (lipids with purple headgroups) from PC (blue headgroups) and creates driving force for trans-leaflet redistribution of DHE. (Bottom, left panel) A suspension of 163μM liposomes consisting of (60:40):2:8 (POPC:POPS):DHE:Chol. Liposome interior consists of 80 mM KCl (red and green spheres), 20 mM KI, and 20 mM MOPS at a pH of 7.5 and the exterior consists of isotonic 100 mM KCl, 20 mM MOPS at a pH of 7.5. All liposome samples contained a background of 100 μM Ca^{2+} to ensure membrane-association of added annexin a5. Each data point is the average of 3 replicate samples. (Bottom, middle panel) Overlay of two emission spectra of (60:40):2:8 (POPC:POPS):DHE:Chol LUVs at 163 μM with 100μM Ca^{2+}: the bottom is DHE signal with no annexin a5 and the top is DHE signal at the apparent maximum (around 7 μM protein from the left panel). (Bottom, right panel) A kinetics scan of 400 μM LUVs and 100μM Ca^{2+} without encapsulated KI quencher at emission maximum of 374 nm. 8 μM annexin a5 was injected (blue arrow) and the signal increase was monitored.

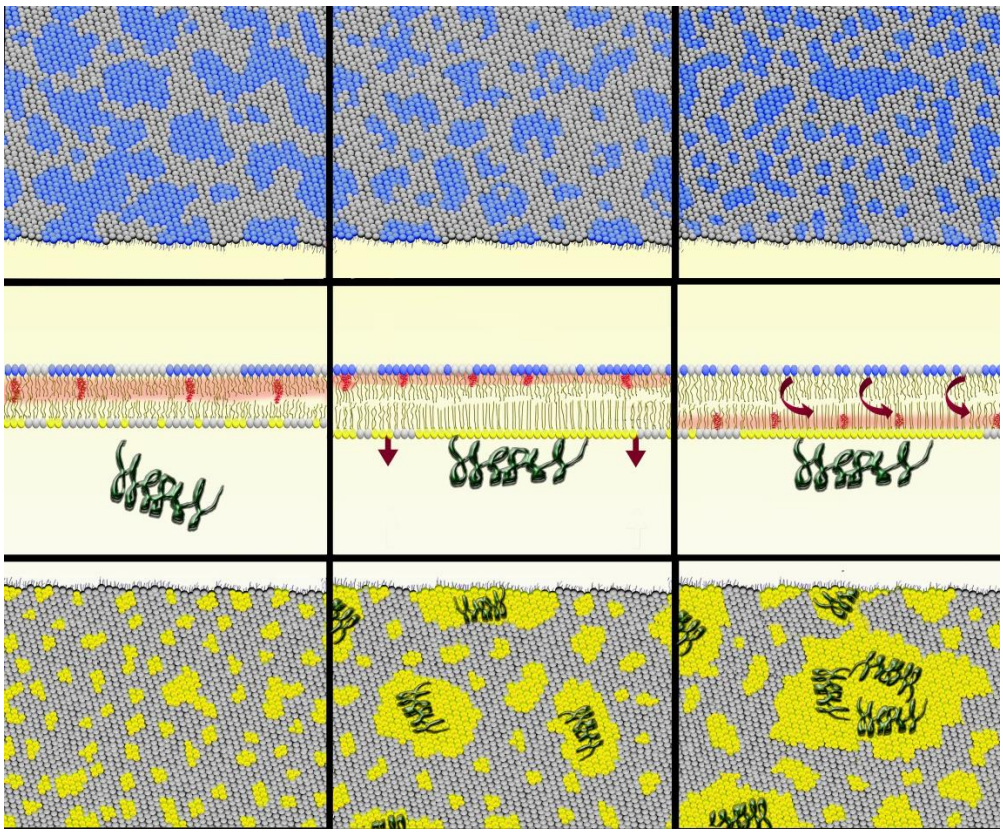

Figure 3.5. Model representation for coupling of inner (yellow+gray) and outer (blue+gray) leaflets of the membrane specifically mediated by annexin a5. In the left column, the outer leaflet (top) is rich in cholesterol and, as a result, forms domains to which signaling proteins can bind or partition into (blue clusters). The inner leaflet (bottom) is not bound by annexin a5 and thus acidic lipids (yellow) mix somewhat ideally. In the middle column, annexin a5 binds to acidic phospholipids (center and bottom), demixes the inner leaflet due to favorable protein-protein, protein-lipid, and lipid-lipid interactions creating a large domain that provides a thermodynamic driving force for cholesterol flip-flop (right most panels). Cholesterol is depleted from the outer leaflet as a result, causing the blue lipids initially found within domain signaling platforms to disperse.

Supplemental Table 3.1. Phase transition parameters of a binary 60:40 DMPC:DMPS lipid mixture.

	ΔH (kcal/mol)	**T_m (C)**	**ΔS (cal/molK)**
16.5mM DMPC:DMPS 60:40	7.50	26.4	25.1
9.4mM DMPC:DMPS 60:40 0.75mM Ca^{2+}	6.39	25.8	21.4
4.9mM DMPC:DMPS 60:40 0.75mM Ca^{2+} 75μM annexin a5	5.66	29.7	18.7

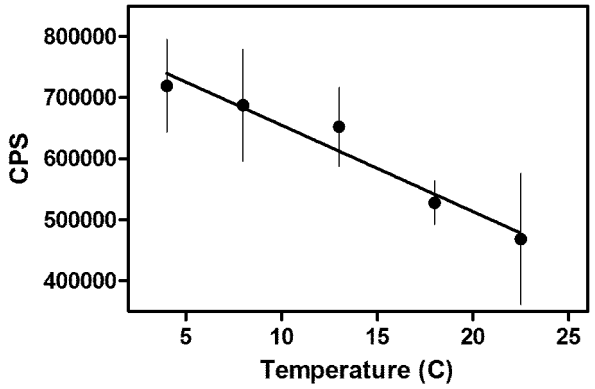

Supplemental Figure 3.1. Temperature dependence of DHE fluorescence in lipid vesicles. The above plot shows a near linear relationship between the DHE fluorescent signal and temperature in vesicles consisting of (60:40):2:8 mole percent (POPC:POPS):DHE:Chol. Data points plotted represent the average and standard deviation (thin vertical lines) of 4 samples at each temperature. The data set line is the output of linear least squares regression.

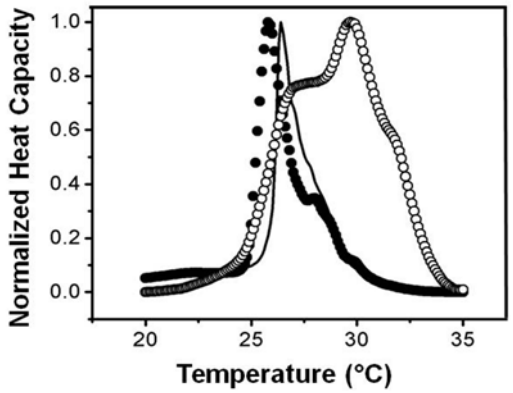

Supplemental Figure 3.2. DSC Thermogram, *Solid Line:* 16.5 mM total lipid as LUV of (60:40) di14:0PC:di14:0PS (or DMPC:DMPS). *Closed Circles:* 9.4 mM total lipid in the presence of 0.75 mM Ca^{2+}. *Open Circles:* 4.9 mM total lipid in the presence of 0.75 mM Ca^{2+} and 75 µM annexin a5. Raw ITC trace annexin a5.

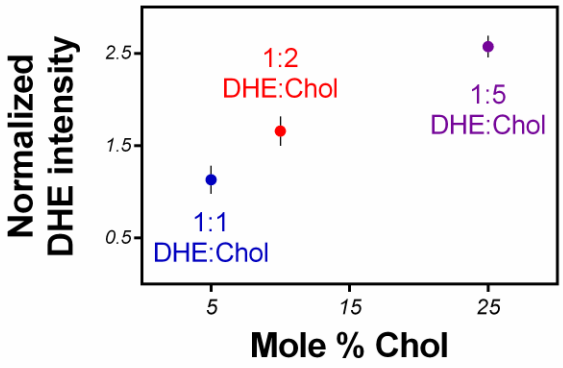

Supplemental Figure 3.3. DHE fluorescence in 100 μM (POPC:POPS):DHE:Chol LUVs, average and standard deviation of 4 measurements. Shown is normalized DHE fluorescence in LUVs whose mole percentages of the above lipids are (60:40):5:5 (blue), (60:40):5:10 (red), and (60:40):5:25 (purple). The above data indicate that the fluorescence of DHE increases with a smaller DHE-to-Chol ratio. Considered in the context of DHE flip-flop, this suggests that the increased change in intensity stems in part from additional accumulation of cholesterol in the outer leaflet of the LUVs.

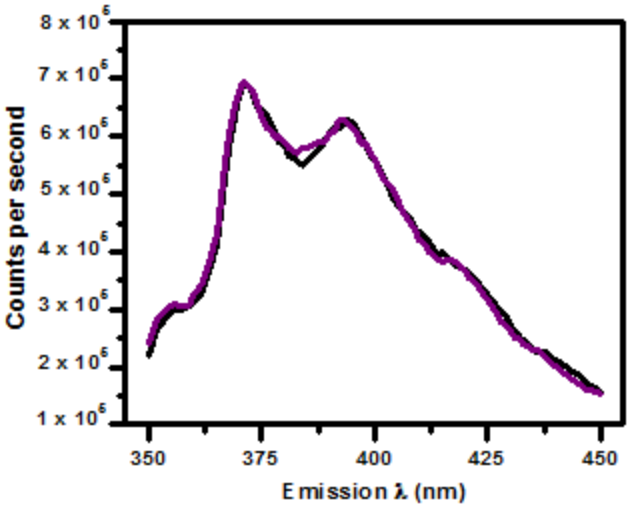

Supplemental Figure 3.4. Annexin A2 in DHE flip-flop experiment with intra-vesicular KI. Measurements were made on a Horiba Jobin Yvon Fluorolog 3 steady-state spectrometer. Shown is an overlay of two emission spectra of (60:40):2:8 (POPC:POPS):DHE:Chol LUVs at 163 μM with 100μM Ca^{2+} with the bottom spectrum containing no annexin A2 and containing 10 μM annexin A2. These results suggest that annexin A2 does not flip DHE as was seen for annexin a5. Each emission spectra is the average of 3 replicate samples.

Chapter Four: Development of a Predictive Binding Model of ErbB1 from Single Particle Tracking

4.1 Introduction

Epidermal Growth Factor Receptor (EGFR or erbB1) is a transmembrane receptor tyrosine kinase that is implicated in normal cellular growth and development. Mutation and/or overexpression of erbB1 can lead to constitutive activity resulting in uncontrolled cellular proliferation. Function of this receptor is dependent on homo- and hetero-dimerization which is induced by the extracellular arm binding to epidermal growth factor (EGF), although activation can also occur in the absence of ligand binding. Upon extracellular ligand binding, intracellular phosphorylation is initiated by asymmetrical dimerization of the kinase domains. Observational evidence suggests that lipid mobility affects the propensity of erbB1 to dimerize. However, due to the stochastic behavior of these receptors, lipid modulation of dimerization and their interaction with erbB1 is poorly understood.

ErbB1 can take on three dimerization confirmations; resting homodimer where neither erbB1 receptors are bound to EGF, heterodimer where one erbB1 receptor is bound to EGF, and bound homodimer where both erbB1 receptors are bound to EGF. During this study, the resting and EGF-bound wild type (WT) receptors were initially compared. After observing a significant increase in the propensity to dimerize from the resting to the EGF-bound WT receptor, the EGF-bound WT receptor's kinase domain was mutated at L858R.[93] Using single particle tracking (SPT) of quantum dot-labeled receptors in the plasma membrane of live cells, receptor mobility and interactions were observed in real time. Through analysis of these trajectories, the population of each receptor state was determined through the modeling of the cumulative probability plot of squared displacement. However, due to the SPT data not being accurately described with two-states, the number of states were investigated by distances between pairwise receptors. In order to gain a better understanding of the erbB1's system and the role of the local lipid environment on dimerization, the relationship between all pairwise receptors were studied.

4.2 Materials and Methods

4.2.1 Single Particle Tracking

Dual-color SPT of resting and EGF-bound erbB1 were conducted using anti-HA- and EGF-conjugated quantum-dots (QD) respectively. These QD probes were used to track erbB1 monomers on the apical cell membrane surface of live HeLa cells to quantify the diffusion and dimerization rates. These two-color images were simultaneously collected by the use of a beam splitter that projected QD655 and QD585 emissions onto an electron-multiplying charge-coupled device. An image registration method was used to map the relative positions of the QD585 and QD655 over the time course of data acquisition.[92] Once the relative positions of the QDs were mapped, trajectories for each individual receptor (Figure 4.1) and a cumulative probability plot of a squared displacement (Figure 4.2 were generated using MATLAB.[93]

4.2.2 Determination of States and Correlation Analysis

For each live HeLa cell that was monitored, coordinates for each individual erbB1 receptor were defined. Using these coordinates, the distance and approach speeds between all pairwise erbB1 receptors and individual speeds were calculated using MATLAB (see Appendix). A correlation analysis was conducted between the distances and approach speeds between all pairwise erbB1 receptors.

4.3 Development of an Allosteric Transition Model

4.3.1 Simplified Allosteric Transition Model

From the cumulative probability plot (Figure 4.2), the probability that a receptor moved a squared displacement (r^2) is represented for the hundreds of live CHO cells that were monitored. The data from this plot was fit using Equation 4.1, where α is the fraction of mobile species, 1-α is the fraction of immobile species, and r_1^2 and r_2^2 are the square displacements of the monomer and dimer receptor respectively.[94]

$$P(r^2, t) = 1 - \left[\alpha \cdot e^{\left(-r^2/r_1^2\right)} + (1-\alpha) \cdot e^{\left(-r^2/r_2^2\right)}\right] \quad (4.1)$$

This equation states that the cumulative probability that a receptor has moved a squared displacement of r^2 is dependent on two-components; mobile and immobile. Upon receptor dimerization, it has been shown through SPT that the receptors have a significantly slower diffusion coefficient compared to the individual monomers.[92] Through the use of the squared displacements of the monomer and dimer receptor conformations and Equation 4.1, the diffusion coefficients were calculated assuming Brownian motion using Equation 4.2

$$r_i^2(t_{lag}) = 4D_i t_{lag} \quad (4.2)$$

where t_{lag} is the time between the frames taken during SPT and D_i is the diffusion coefficient for the monomer or dimer receptor conformations. The calculated diffusion coefficients were compared to a previous study[93] to ensure accuracy of the model.

From the fit parameter α, the fraction for the monomer and dimer receptor conformations were able to be determined. Utilizing these fractions and a two-state allosteric transition model, the equilibrium rate constants for a receptor between its dimer and monomeric form were able to be studied (Figure 4.3). The fit parameters from the modeling of the cumulative probability plot of squared displacement shows an increase in propensity for receptors to dimerize when there is a mutation within the kinase domain (Table 4.1). While the trends determined from this model are consistent with previous studies[93], the SPT data is not accurately described by two states when looking at the off-rate kinetics of erbB1 dimers.

4.3.2 Complex Allosteric Transition Model

To include all potential dimerization confirmations, a complex allosteric transition model was developed (Figure 4.4). The partition function for this model system is described in Equation 4.3

$$Q = 1 + 2\kappa[X] + L[R](2\alpha\kappa[X] + 1 + \alpha^2\sigma\kappa^2[X]^2) \quad (4.3)$$

where R is an erbB1 receptor, X is EGF, L is the equilibrium constant of two receptors, κ is the equilibrium constant between EGF and an erbB1 receptor, α and σ are cooperativity factors. To obtain the equilibrium constants and cooperativity factors for this model system, the number of states that any potential dimerization confirmation can take needs to be confirmed. Since the SPT data was not accurately described by a two-state model calculating the dimer off-rates, a three-state Hidden Markov Model (HMM) was used to estimate the dimerization kinetics.[92] The distances between two erbB1 receptors were globally fit using a maximum likelihood estimation to identify a transition between the initial dimerization states. This analysis determined that erbB1 receptors have three probabilistic states: dimer, co-confined, and free. Based on the crystal structure of a back-to-back erbB1 structure, the dimer state is defined by an interaction distance of 40-50 nm. However, the co-confined and free state were not able to be well-defined due to fluctuations in the domain size of the co-confined state.[92] Once the number of states are confirmed and defined, the probability of being in each state can be used to determine the equilibrium constants and cooperativity factors by the means of the Equation 4.3.

4.4 Investigation of the role of the local lipid environment in dimerization of erbB1 receptors

4.4.1 Determination of the Number of States using Distances between all Pairwise Receptors

Since one of the states was able to be determined by the distance between two erbB1 receptors, the distances between all pairwise receptors were utilized to investigate the number of states present within this system. After each distance between all pairwise receptors were calculated at every time frame using the coordinates for the individual receptors obtained through SPT experiments, a probability distribution of these distances was created for each the resting and bound homodimer confirmations (Figure 4.5). At first glance, there is not a distinct difference between the two dimer confirmations and the shape of the distribution appear Gaussian. With the knowledge that two receptors must at

least be in two confirmations, dimer and monomer, and no additional peaks presents, it appears that multiple states are contributing to the shape of this distribution. Instead of deconvoluting the distribution, the speed of individual erbB1 receptors were calculated to further investigate the number of states.

4.4.2 Determination of the Number of States using Individual Speeds of erbB1 Receptors

Due to the complexity of the erbB1 system, speed of individual receptors were calculated to study the number of states that could occur by utilizing the coordinates of the receptors and the lag time between each frame. Once these speeds were calculated, a probability distribution of the speeds was created for the resting and bound homodimer confirmation (Figure 4.6). Again, there is no apparent difference between these two dimer confirmations. At first glance, it appears that two states are present for an individual erbB1 receptor, where the first state is slow moving, termed the immobile state, and the second state samples a distribution of speeds, termed the mobile state. The immobile and mobile state occurs ~80% and ~20% of the time, respectively. However, with the knowledge that there in an increase in dimer lifetime and activity when in the bound homodimer confirmation[93], an increase in the probability of being in the immobile state when comparing the bound homodimer to the resting homodimer should be observed. This leads to the speculation that the immobile state is an artifact in the analysis and an individual receptor can sample a distribution of speeds.

4.4.3 Correlation Analysis between Approach Speeds and Pairwise Distances

To investigate the role of the local lipid environment, a correlation analysis was conducted between the distance and approach speeds between pairwise erbB1 eceptors. The approach speeds between pairwise receptors were calculated using the individual speeds and correlated against the distances between the same pairs of receptors to obtain correlation coefficients and placed into seven different categories (Table 4.2). The probability of the correlation categories was created (Figure 4.7) and both the resting and bound homodimer confirmation showed that the relationship between the distance and approach speed of pairwise receptors had a linear relationship with a positive correlation (0.21 ± 0.03 and 0.19 ± 0.03, respectively). This is consistent with previous studies

showing that when the distance between two individual erbB1 receptors decrease, their speed decreases, thus, increasing their propensity to dimerize.[93]

4.5 Future Directions

While previous studies state that changes in dimerization activity are due to conformational changes of erbB1, we hypothesize that the local environment of the lipid membrane is a key component. By investigating how individual erbB1 receptors interact with one another, the landscape in which the signaling events occur is explored. However, issues have arose when conducting these types of analysis on the SPT data due to the stochastic behavior of erbB1 receptors.

The first question that needs to be addressed is how many states are available for an individual erbB1 receptor. Once the number of states are determined, the probability of being in that state can be calculated and applied to a partition function to determine equilibrium constants and cooperativity factors. However, the analysis that was conducted to create the probability distributions to answer this question did not take into account that there may be multiple types of individual receptors based on the movement of their trajectories. When looking into 3D trajectory plots of the individual receptors (Figure 4.1), it can be observed that some receptors have minimal movement throughout the length of the SPT experiment, while the movement of other receptors are random and constant, and some receptors display a mixture of both. By first classifying the receptors by the movement of their trajectories, insight could be gained on how to determine the number of states that are available to an individual erbB1 receptor. This classification can be done by conducting an autocorrelation analysis on individual receptor trajectories by cross-correlating the movement at different time frames. This analysis will determine patterns of specific classes of trajectories and how many movement classes are present. Once investing the behavior of the movement of individual receptors, the interaction distance between receptors can be explored.

To investigate the role of the local lipid environment in the dimerization process of erbB1 receptors, the interaction distance between two receptors can be utilized. By defining how close a receptor needs to be in order to have an interaction with another receptor, neighborhoods, or clusters, of the receptors can be studied. Previously, a correlation analysis was conducted on all receptors at every time frame to see if there was

a linear relationship between the distance and approach speed on pairwise receptors. After defining a radius of which a neighborhood can be formed, this distance can decrease the number of receptors that the correlation analysis is conducted on for each individual receptor. This correlation analysis will allow insight on how receptors move within neighborhoods. For instance, do neighborhoods move together as a group or is there random movement at close distances? After investigating the impact of the short, and potentially long range impact of the erbB1 receptors, defining the number of available states, and application of a partition function, the role of the local lipid environment on this system can be evaluated.

Table 4.1. The fit parameters obtained by modeling the cumulative probability plots of square displacement for individual erbB1 receptors. From the fit parameters using Equation 4.1, diffusion coefficients and equilibrium constants were calculated using Equations 4.2 and principals from an allosteric transition model, respectively.

Receptor Type	α	1-α	r_1^2	r_2^2	D_1	D_2	αL
EGF-Bound WT	0.676	0.324	0.031	0.002	0.015	0.001	0.479
EGF Bound Mutated	0.571	0.429	0.026	0.001	0.013	0.001	0.750

Table 4.2. The seven categories for the correlation analysis between the distance and approach speed between pairwise receptors based on the correlation coefficient.

Category	Correlation Coefficient Range
Strong, Negative Correlation	-1.0 to -0.5
Moderate, Negative Correlation	-0.5 to -0.3
Weak, Negative Correlation	-0.3 to -0.1
No Correlation	-0.1 to +0.1
Weak, Positive Correlation	+0.1 to +0.3
Moderate, Positive Correlation	+0.3 to +0.5
Strong, Positive Correlation	+0.5 to +1.0

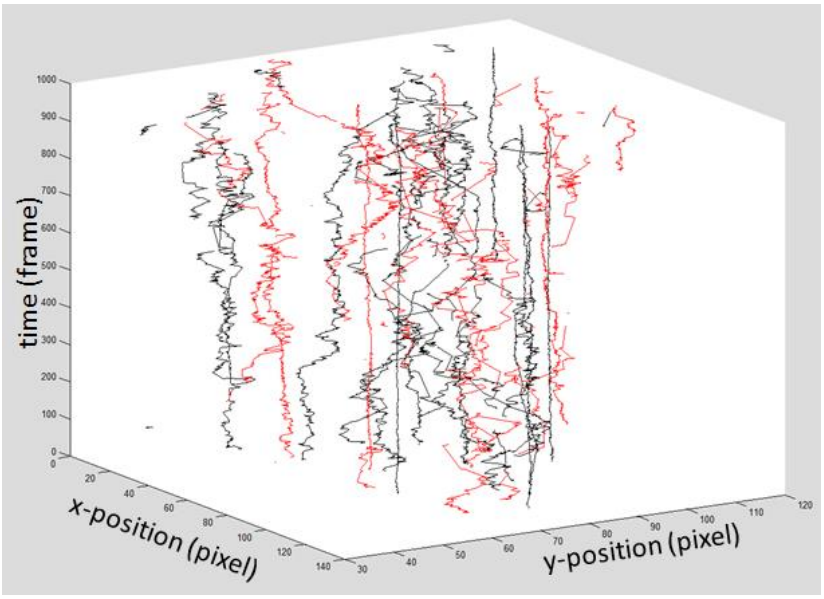

Figure 4.1. 3D Trajectories of individual receptors generated using SPT over the time of data acquisition where x and y are positions (in pixels) and z is time (in frames).

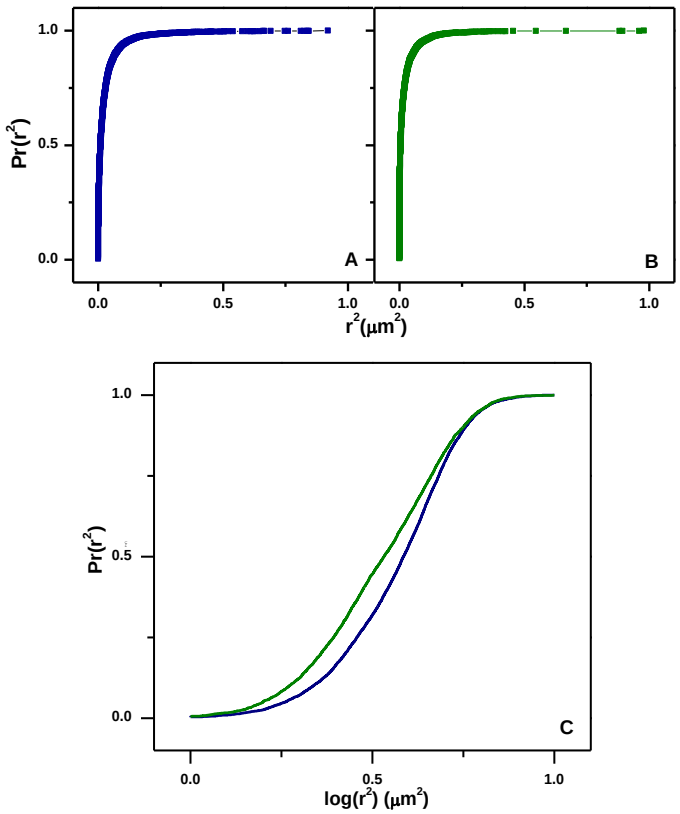

Figure 4.2. Cumulative probability plots for squared displacement of individual receptors generated using SPT over the time of data acquisition. Over hundreds of individual receptors contributed to this signal. A: WT EGF-bound receptor. B: Kinase domain mutated EGF-bound receptor. C: A transformed cumulative probability plot of squared displacement where the x-axis is the normalized log of the squared displacement where the blue line represents the WT EGF-bound receptor and the green line represents the kinase domain mutated EGF-bound receptor.

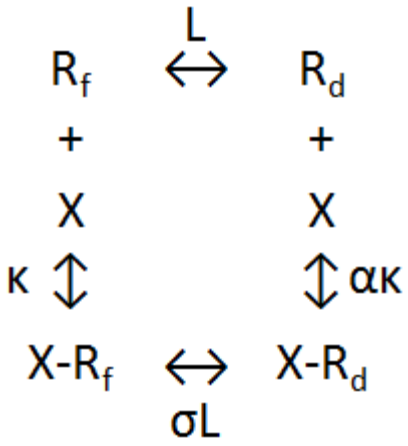

Figure 4.3. The simplified allosteric transition model for the dimerization of individual erbB1 receptors where R_i the monomeric form of erbB1, R_a is the dimeric form of erbB1, X is EGF, K is the equilibrium constant of an erbB1 receptor binding to EGF, L is the equilibrium constant of the dimerization of two erbB1 receptors, and α and σ are cooperativity factors.

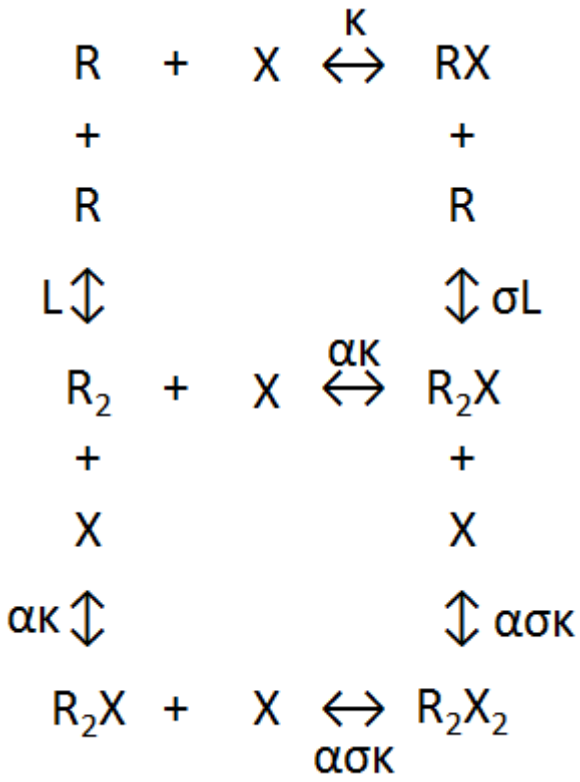

Figure 4.4. The complex allosteric transition model for the dimerization of individual erbB1 receptors where R is an erbB1 receptor, X is EGF, L is the equilibrium constant of two receptors, κ is the equilibrium constant between EGF and an erbB1 receptor, α and σ are cooperativity factors.

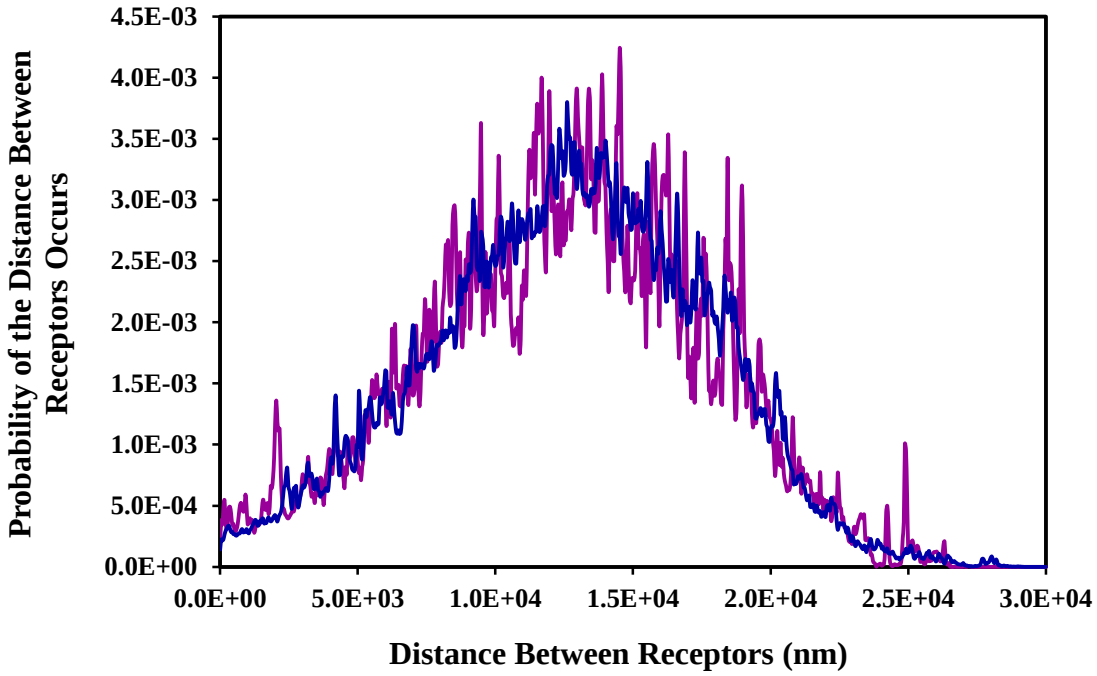

Figure 4.5. The probability distribution of distance between pairwise erbB1 receptors where blue represents the resting homodimer and purple represents the bound homodimer.

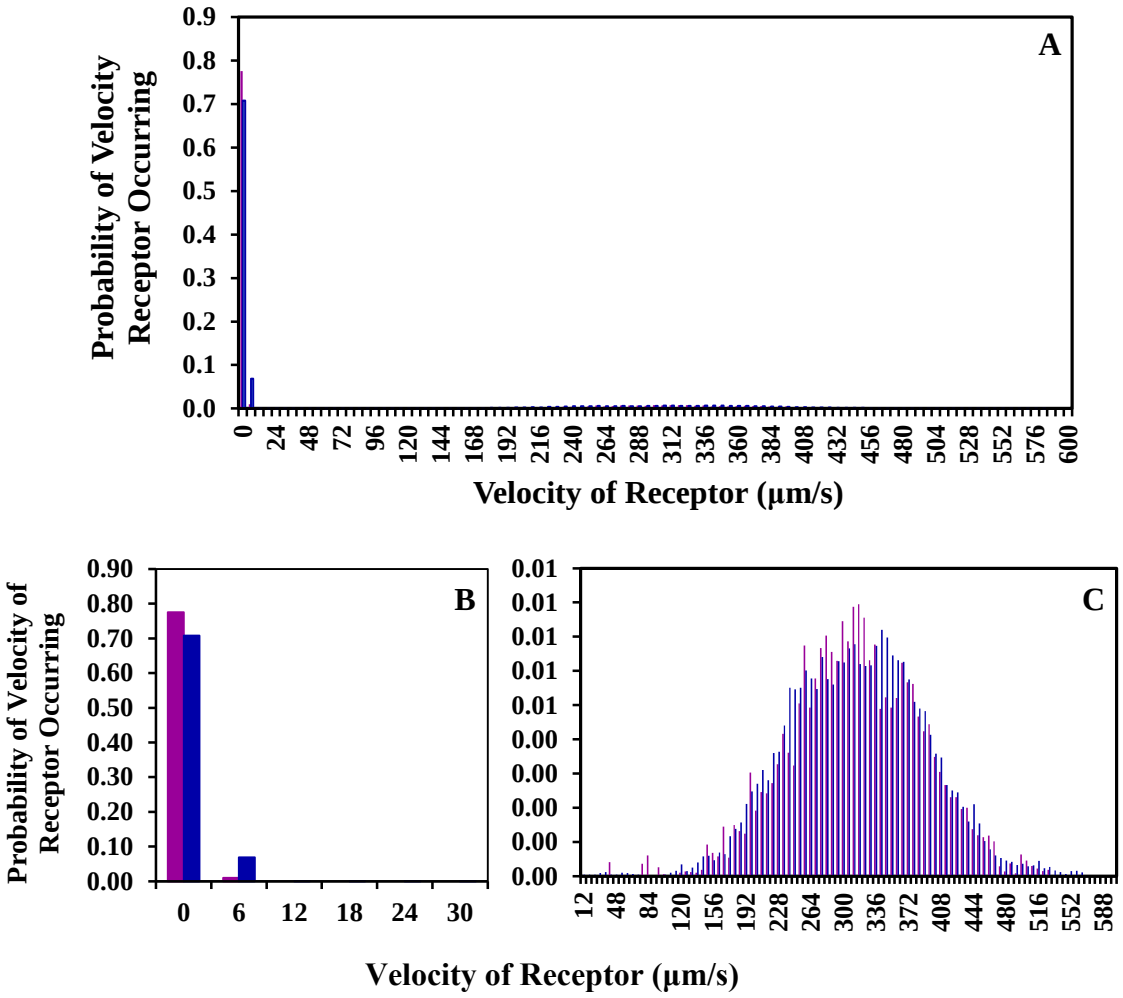

Figure 4.6. The probability distribution of speeds of individual erbB1 receptors where blue represents the resting homodimer and purple represents the bound homodimer. A: The probability distribution of speeds of individual erbB1 receptors for both immobile and mobile state. B: The probability distribution of speeds of individual erbB1 receptors for the immobile state that occurs ~80% of the time for both dimer confirmations. C: The probability distribution of speeds of individual erbB1 receptors for the mobile state that occurs ~20% of the time for both dimer confirmations.

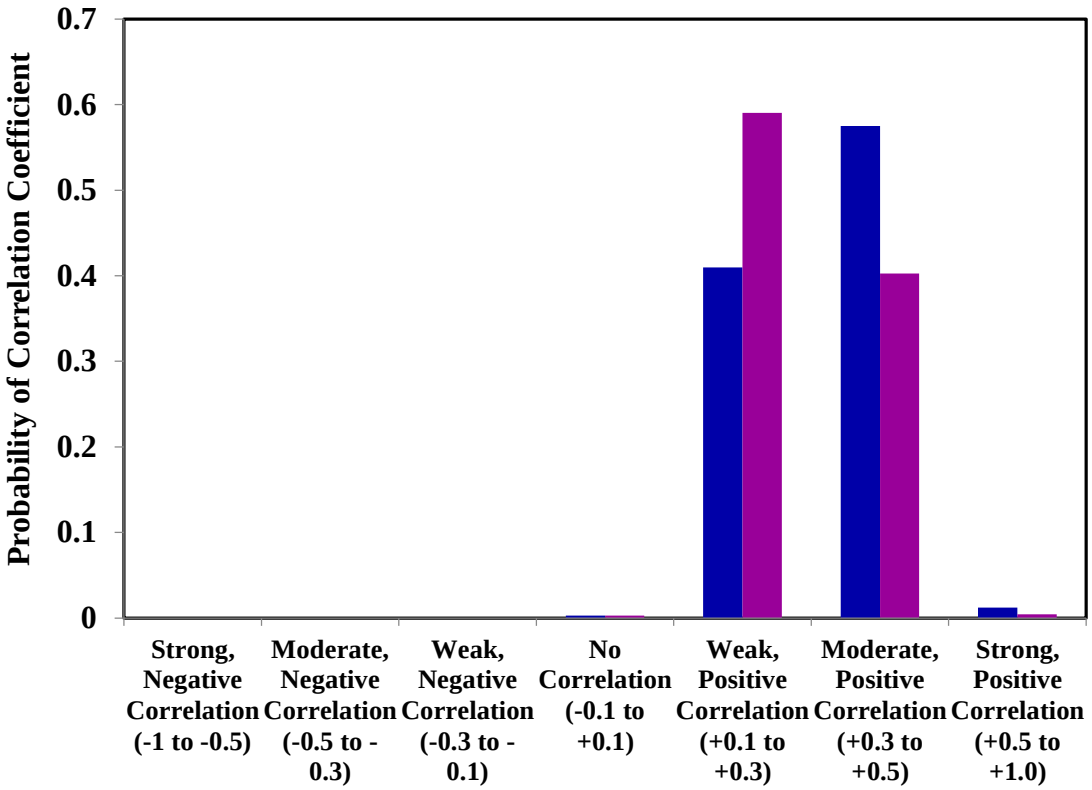

Figure 4.7. Correlation analysis between the distance and approach speed of pairwise erbB1 receptors represented in a histogram where the x-axis is the seven different categories for the analysis and the y-axis is the probability of the category occurring for the resting homodimer confirmation (blue) and the bound homodimer confirmation (purple).

References

1. Lodish H, Berk A, Zipursky SL, et al. *Molecular Cell Biology*. 4th ed.; New York: W. H. Freeman; 2000.
2. Tsai C-J, Nussinov R. A Unified View of "How Allostery Works." Livesay DR, ed. *PLoS Computational Biology*. 2014;10(2):e1003394.
3. Sudhof, T. C. (2004) The synaptic vesicle cycle, *Annu Rev Neurosci 27*, 509-547.
4. Fealey, M. E., Gauer, J. W., Kempka, S. C., Miller, K., Nayak, K., Sutton, R. B., and Hinderliter, A. (2012) Negative coupling as a mechanism for signal propagation between C2 domains of synaptotagmin I, *PLoS One 7*, e46748.
5. Lai, Y., Lou, X., Jho, Y., Yoon, T. Y., and Shin, Y. K. (2013) The synaptotagmin 1 linker may function as an electrostatic zipper that opens for docking but closes for fusion pore opening, *Biochem J 456*, 25-33.
6. Caccin, P., Scorzeto, M., Damiano, N., Marin, O., Megighian, A., and Montecucco, C. (2015) The synaptotagmin juxtamembrane domain is involved in neuroexocytosis, *FEBS Open Bio 5*, 388-396.
7. Lee, J., and Littleton, J. T. (2015) Transmembrane tethering of synaptotagmin to synaptic vesicles controls multiple modes of neurotransmitter release, *Proc Natl Acad Sci U S A 112*, 3793-3798.
8. Luque, I., Leavitt, S. A., and Freire, E. (2002) The linkage between protein folding and functional cooperativity: two sides of the same coin?, *Annu Rev Biophys Biomol Struct 31*, 235-256.
9. Freire, E. (1995) Differential scanning calorimetry, *Methods Mol Biol 40*, 191-218.
10. Vacic, V., Uversky, V. N., Dunker, A. K., and Lonardi, S. (2007) Composition Profiler: a tool for discovery and visualization of amino acid composition differences, *BMC Bioinformatics 8*, 211.
11. Chen, J. W., Romero, P., Uversky, V. N., and Dunker, A. K. (2006) Conservation of intrinsic disorder in protein domains and families: II. functions of conserved disorder, *J Proteome Res 5*, 888-898.
12. Chen, J. W., Romero, P., Uversky, V. N., and Dunker, A. K. (2006) Conservation of intrinsic disorder in protein domains and families: I. A database of conserved predicted disordered regions, *J Proteome Res 5*, 879-887.
13. Romero, P., Obradovic, Z., Li, X., Garner, E. C., Brown, C. J., and Dunker, A. K. (2001) Sequence complexity of disordered protein, *Proteins 42*, 38-48.
14. Dyson, H. J., and Wright, P. E. (2005) Intrinsically unstructured proteins and their functions, *Nat Rev Mol Cell Biol 6*, 197-208.
15. Gauer, J. W., Sisk, R., Murphy, J. R., Jacobson, H., Sutton, R. B., Gillispie, G. D., and Hinderliter, A. (2012) Mechanism for calcium ion sensing by the C2A domain of synaptotagmin I, *Biophys J 103*, 238-246.
16. Rice, A. M., Mahling, R., Fealey, M. E., Rannikko, A., Dunleavy, K., Hendrickson, T., Lohese, K. J., Kruggel, S., Heiling, H., Harren, D., Sutton, R. B., Pastor, J., and Hinderliter, A. (2014) Randomly organized lipids and marginally stable proteins: a coupling of weak interactions to optimize membrane signaling, *Biochim Biophys Acta 1838*, 2331-2340.

17. Lu, B., Kiessling, V., Tamm, L. K., and Cafiso, D. S. (2014) The juxtamembrane linker of full-length synaptotagmin 1 controls oligomerization and calcium-dependent membrane binding, *J Biol Chem 289*, 22161-22171.
18. Uversky, V. N. (2015) Unreported intrinsic disorder in proteins: disorder emergency room, *Intrinsically Disordered Proteins 3*, 1-15.
19. Hilser, V. J., and Thompson, E. B. (2007) Intrinsic disorder as a mechanism to optimize allosteric coupling in proteins, *Proc Natl Acad Sci U S A 104*, 8311-8315.
20. Kingsley, P. B., and Feigenson, G. W. (1979) The synthesis of a perdeuterated phospholipid: 1,2 dimyristoyl-*sn*-glycero-3-phosphocholine-d72, *Chem. Phys. Lipids. 24*.
21. Iakoucheva, L. M., Kimzey, A. L., Masselon, C. D., Smith, R. D., Dunker, A. K., and Ackerman, E. J. (2001) Aberrant mobility phenomena of the DNA repair protein XPA, *Protein Sci 10*, 1353-1362.
22. McMullen, T. P., Lewis, R. N., and McElhaney, R. N. (1993) Differential scanning calorimetric study of the effect of cholesterol on the thermotropic phase behavior of a homologous series of linear saturated phosphatidylcholines, *Biochemistry 32*, 516-522.
23. Gauer, J. W., Knutson, K. J., Jaworski, S. R., Rice, A. M., Rannikko, A. M., Lentz, B. R., and Hinderliter, A. (2013) Membrane modulates affinity for calcium ion to create an apparent cooperative binding response by annexin a5, *Biophys J 104*, 2437-2447.
24. Kertz, J. A., Almeida, P. F., Frazier, A. A., Berg, A. K., and Hinderliter, A. (2007) The cooperative response of synaptotagmin I C2A. A hypothesis for a Ca2+-driven molecular hammer, *Biophys J 92*, 1409-1418.
25. Ubach, J., Zhang, X., Shao, X., Sudhof, T. C., and Rizo, J. (1998) Ca2+ binding to synaptotagmin: how many Ca2+ ions bind to the tip of a C2-domain?, *Embo J 17*, 3921-3930.
26. Takamori, S., Holt, M., Stenius, K., Lemke, E. A., Gronborg, M., Riedel, D., Urlaub, H., Schenck, S., Brugger, B., Ringler, P., Muller, S. A., Rammner, B., Grater, F., Hub, J. S., De Groot, B. L., Mieskes, G., Moriyama, Y., Klingauf, J., Grubmuller, H., Heuser, J., Wieland, F., and Jahn, R. (2006) Molecular anatomy of a trafficking organelle, *Cell 127*, 831-846.
27. Tamiola, K., Acar, B., and Mulder, F. A. (2010) Sequence-specific random coil chemical shifts of intrinsically disordered proteins, *J Am Chem Soc 132*, 18000-18003.
28. Lee, S. H., Cha, E. J., Lim, J. E., Kwon, S. H., Kim, D. H., Cho, H., and Han, K. H. (2012) Structural characterization of an intrinsically unfolded mini-HBX protein from hepatitis B virus, *Mol Cells 34*, 165-169.
29. Rucker, A. L., and Creamer, T. P. (2002) Polyproline II helical structure in protein unfolded states: lysine peptides revisited, *Protein Sci 11*, 980-985.
30. Xu, C., Gagnon, E., Call, M. E., Schnell, J. R., Schwieters, C. D., Carman, C. V., Chou, J. J., and Wucherpfennig, K. W. (2008) Regulation of T cell receptor activation by dynamic membrane binding of the CD3epsilon cytoplasmic tyrosine-based motif, *Cell 135*, 702-713.

31. Haxholm, G. W., Nikolajsen, L. F., Olsen, J. G., Fredsted, J., Larsen, F. H., Goffin, V., Pedersen, S. F., Brooks, A. J., Waters, M. J., and Kragelund, B. B. (2015) Intrinsically disordered cytoplasmic domains of two cytokine receptors mediate conserved interactions with membranes, *Biochem J 468*, 495-506.
32. Papayannopoulos, V., Co, C., Prehoda, K. E., Snapper, S., Taunton, J., and Lim, W. A. (2005) A polybasic motif allows N-WASP to act as a sensor of PIP(2) density, *Mol Cell 17*, 181-191.
33. Santner, A. A., Croy, C. H., Vasanwala, F. H., Uversky, V. N., Van, Y. Y., and Dunker, A. K. (2012) Sweeping away protein aggregation with entropic bristles: intrinsically disordered protein fusions enhance soluble expression, *Biochemistry 51*, 7250-7262.
34. Li, J., Motlagh, H. N., Chakuroff, C., Thompson, E. B., and Hilser, V. J. (2012) Thermodynamic dissection of the intrinsically disordered N-terminal domain of human glucocorticoid receptor, *J Biol Chem 287*, 26777-26787.
35. Torrecillas, A., Laynez, J., Menendez, M., Corbalan-Garcia, S., and Gomez-Fernandez, J. C. (2004) Calorimetric study of the interaction of the C2 domains of classical protein kinase C isoenzymes with Ca2+ and phospholipids, *Biochemistry 43*, 11727-11739.
36. Zhang, X., Rizo, J., and Sudhof, T. C. (1998) Mechanism of phospholipid binding by the C2A-domain of synaptotagmin I, *Biochemistry 37*, 12395-12403.
37. Tochtrop, G. P., Richter, K., Tang, C., Toner, J. J., Covey, D. F., and Cistola, D. P. (2002) Energetics by NMR: site-specific binding in a positively cooperative system, *Proc Natl Acad Sci U S A 99*, 1847-1852.
38. Freire, E., Schon, A., and Velazquez-Campoy, A. (2009) Isothermal titration calorimetry: general formalism using binding polynomials, *Methods Enzymol 455*, 127-155.
39. Herrick, D. Z., Sterbling, S., Rasch, K. A., Hinderliter, A., and Cafiso, D. S. (2006) Position of synaptotagmin I at the membrane interface: cooperative interactions of tandem C2 domains, *Biochemistry 45*, 9668-9674.
40. Martens, S., and McMahon, H. T. (2008) Mechanisms of membrane fusion: disparate players and common principles, *Nat Rev Mol Cell Biol 9*, 543-556.
41. Baker, K., Gordon, S. L., Grozeva, D., van Kogelenberg, M., Roberts, N. Y., Pike, M., Blair, E., Hurles, M. E., Chong, W. K., Baldeweg, T., Kurian, M. A., Boyd, S. G., Cousin, M. A., and Raymond, F. L. (2015) Identification of a human synaptotagmin-1 mutation that perturbs synaptic vesicle cycling, *J Clin Invest 125*, 1670-1678.
42. Bykhovskaia, M. (2015) Calcium binding promotes conformational flexibility of the neuronal ca(2+) sensor synaptotagmin, *Biophys J 108*, 2507-2520.
43. Fealey, M. E., and Hinderliter, A. (2013) Allostery and instability in the functional plasticity of synaptotagmin I, *Commun Integr Biol 6*, e22830.
44. Motlagh, H. N., and Hilser, V. J. (2012) Agonism/antagonism switching in allosteric ensembles, *Proc Natl Acad Sci U S A 109*, 4134-4139.
45. Simons, K., and Vaz, W. L. (2004) Model systems, lipid rafts, and cell membranes, *Annu Rev Biophys Biomol Struct 33*, 269-295.
46. Kinnunen, P. K. (1991) On the principles of functional ordering in biological membranes, *Chem Phys Lipids 57*, 375-399.

47. Almeida, P. F., Pokorny, A., and Hinderliter, A. (2005) Thermodynamics of membrane domains, *Biochim Biophys Acta 1720*, 1-13.
48. Hinderliter, A., Almeida, P. F., Creutz, C. E., and Biltonen, R. L. (2001) Domain formation in a fluid mixed lipid bilayer modulated through binding of the C2 protein motif, *Biochemistry 40*, 4181-4191.
49. Mbamala, E. C., Ben-Shaul, A., and May, S. (2005) Domain formation induced by the adsorption of charged proteins on mixed lipid membranes, *Biophys J 88*, 1702-1714.
50. Veatch, S. L., and Keller, S. L. (2003) Separation of liquid phases in giant vesicles of ternary mixtures of phospholipids and cholesterol, *Biophys J 85*, 3074-3083.
51. Veatch, S. L., and Keller, S. L. (2002) Organization in lipid membranes containing cholesterol, *Phys Rev Lett 89*, 268101.
52. Gerke, V., Creutz, C. E., and Moss, S. E. (2005) Annexins: linking Ca2+ signalling to membrane dynamics, *Nat Rev Mol Cell Biol 6*, 449-461.
53. Almeida, P. F., Best, A., and Hinderliter, A. (2011) Monte Carlo simulation of protein-induced lipid demixing in a membrane with interactions derived from experiment, *Biophys J 101*, 1930-1937.
54. Vats, K., Knutson, K., Hinderliter, A., and Sheets, E. D. (2010) Peripheral protein organization and its influence on lipid diffusion in biomimetic membranes, *ACS Chem Biol 5*, 393-403.
55. Miao, L., Nielsen, M., Thewalt, J., Ipsen, J. H., Bloom, M., Zuckermann, M. J., and Mouritsen, O. G. (2002) From lanosterol to cholesterol: structural evolution and differential effects on lipid bilayers, *Biophys J 82*, 1429-1444.
56. Kiessling, V., Wan, C., and Tamm, L. K. (2009) Domain coupling in asymmetric lipid bilayers, *Biochim Biophys Acta 1788*, 64-71.
57. Bennett, W. F., MacCallum, J. L., Hinner, M. J., Marrink, S. J., and Tieleman, D. P. (2009) Molecular view of cholesterol flip-flop and chemical potential in different membrane environments, *J Am Chem Soc 131*, 12714-12720.
58. Jo, S., Rui, H., Lim, J. B., Klauda, J. B., and Im, W. (2010) Cholesterol flip-flop: insights from free energy simulation studies, *J Phys Chem B 114*, 13342-13348.
59. John, K., Kubelt, J., Muller, P., Wustner, D., and Herrmann, A. (2002) Rapid transbilayer movement of the fluorescent sterol dehydroergosterol in lipid membranes, *Biophys J 83*, 1525-1534.
60. Robalo, J. R., do Canto, A. M., Carvalho, A. J., Ramalho, J. P., and Loura, L. M. (2013) Behavior of fluorescent cholesterol analogues dehydroergosterol and cholestatrienol in lipid bilayers: a molecular dynamics study, *J Phys Chem B 117*, 5806-5819.
61. Wang, J., Megha, and London, E. (2004) Relationship between sterol/steroid structure and participation in ordered lipid domains (lipid rafts): implications for lipid raft structure and function, *Biochemistry 43*, 1010-1018.
62. Garvik, O., Benediktson, P., Simonsen, A. C., Ipsen, J. H., and Wustner, D. (2009) The fluorescent cholesterol analog dehydroergosterol induces liquid-ordered domains in model membranes, *Chem Phys Lipids 159*, 114-118.
63. Maxfield, F. R., and Wustner, D. (2012) Analysis of cholesterol trafficking with fluorescent probes, *Methods Cell Biol 108*, 367-393.

64. McIntosh, A. L., Atshaves, B. P., Huang, H., Gallegos, A. M., Kier, A. B., and Schroeder, F. (2008) Fluorescence techniques using dehydroergosterol to study cholesterol trafficking, *Lipids 43*, 1185-1208.
65. Kingsley, P. B., and Feigenson, G. W. (1981) 1H-NMR study of the location and motion of ubiquinones in perdeuterated phosphatidylcholine bilayers, *Biochim Biophys Acta 635*, 602-618.
66. Schroeder, F., Barenholz, Y., Gratton, E., and Thompson, T. E. (1987) A fluorescence study of dehydroergosterol in phosphatidylcholine bilayer vesicles, *Biochemistry 26*, 2441-2448.
67. Zhang, J., Cao, H., Jing, B., Almeida, P. F., and Regen, S. L. (2006) Cholesterol-phospholipid association in fluid bilayers: a thermodynamic analysis from nearest-neighbor recognition measurements, *Biophys J 91*, 1402-1406.
68. Zucker, R. S., and Regehr, W. G. (2002) Short-term synaptic plasticity, *Annu Rev Physiol 64*, 355-405.
69. Mabrey, S., and Sturtevant, J. M. (1976) Investigation of phase transitions of lipids and lipid mixtures by sensitivity differential scanning calorimetry, *Proc Natl Acad Sci U S A 73*, 3862-3866.
70. Mountcastle, D. B., Biltonen, R. L., and Halsey, M. J. (1978) Effect of anesthetics and pressure on the thermotropic behavior of multilamellar dipalmitoylphosphatidylcholine liposomes, *Proc Natl Acad Sci U S A 75*, 4906-4910.
71. Dibble, A. R., Hinderliter, A. K., Sando, J. J., and Biltonen, R. L. (1996) Lipid lateral heterogeneity in phosphatidylcholine/phosphatidylserine/diacylglycerol vesicles and its influence on protein kinase C activation, *Biophys J 71*, 1877-1890.
72. Hinderliter, A. K., Dibble, A. R., Biltonen, R. L., and Sando, J. J. (1997) Activation of protein kinase C by coexisting diacylglycerol-enriched and diacylglycerol-poor lipid domains, *Biochemistry 36*, 6141-6148.
73. Casal, H. L., Mantsch, H. H., Paltauf, F., and Hauser, H. (1987) Infrared and 31P-NMR studies of the effect of Li+ and Ca2+ on phosphatidylserines, *Biochim Biophys Acta 919*, 275-286.
74. Casal, H. L., Martin, A., Mantsch, H. H., Paltauf, F., and Hauser, H. (1987) Infrared studies of fully hydrated unsaturated phosphatidylserine bilayers. Effect of Li+ and Ca2+, *Biochemistry 26*, 7395-7401.
75. Mattai, J., Hauser, H., Demel, R. A., and Shipley, G. G. (1989) Interactions of metal ions with phosphatidylserine bilayer membranes: effect of hydrocarbon chain unsaturation, *Biochemistry 28*, 2322-2330.
76. Marsh, D. (1991) General features of phospholipid phase transitions, *Chem Phys Lipids 57*, 109-120.
77. Ipsen, J. H., Karlstrom, G., Mouritsen, O. G., Wennerstrom, H., and Zuckermann, M. J. (1987) Phase equilibria in the phosphatidylcholine-cholesterol system, *Biochim Biophys Acta 905*, 162-172.
78. Ipsen, J. H., Mouritsen, O. G., and Bloom, M. (1990) Relationships between lipid membrane area, hydrophobic thickness, and acyl-chain orientational order. The effects of cholesterol, *Biophys J 57*, 405-412.
79. Moss, S. E., and Morgan, R. O. (2004) The annexins, *Genome Biol 5*, 219.

80. Morgan, R. O., and Fernandez, M. P. (1995) Molecular phylogeny of annexins and identification of a primitive homologue in Giardia lamblia, *Mol Biol Evol 12*, 967-979.
81. Bers, D. M. (2014) Cardiac sarcoplasmic reticulum calcium leak: basis and roles in cardiac dysfunction, *Annu Rev Physiol 76*, 107-127.
82. Despa, S., Shui, B., Bossuyt, J., Lang, D., Kotlikoff, M. I., and Bers, D. M. (2014) Junctional cleft [Ca(2)(+)]i measurements using novel cleft-targeted Ca(2)(+) sensors, *Circ Res 115*, 339-347.
83. Meinrenken, C. J., Borst, J. G., and Sakmann, B. (2003) Local routes revisited: the space and time dependence of the Ca2+ signal for phasic transmitter release at the rat calyx of Held, *J Physiol 547*, 665-689.
84. Draeger, A., Monastyrskaya, K., and Babiychuk, E. B. (2011) Plasma membrane repair and cellular damage control: the annexin survival kit, *Biochem Pharmacol 81*, 703-712.
85. Monastyrskaya, K., Babiychuk, E. B., and Draeger, A. (2009) The annexins: spatial and temporal coordination of signaling events during cellular stress, *Cell Mol Life Sci 66*, 2623-2642.
86. Berridge, M. J., Bootman, M. D., and Roderick, H. L. (2003) Calcium signalling: dynamics, homeostasis and remodelling, *Nat Rev Mol Cell Biol 4*, 517-529.
87. Berridge, M. J., Lipp, P., and Bootman, M. D. (2000) The versatility and universality of calcium signalling, *Nat Rev Mol Cell Biol 1*, 11-21.
88. Clapham, D. E. (2007) Calcium signaling, *Cell 131*, 1047-1058.
89. Bublitz, M., Musgaard, M., Poulsen, H., Thogersen, L., Olesen, C., Schiott, B., Morth, J. P., Moller, J. V., and Nissen, P. (2013) Ion pathways in the sarcoplasmic reticulum Ca2+-ATPase, *J Biol Chem 288*, 10759-10765.
90. Blaustein, M. P., and Lederer, W. J. (1999) Sodium/calcium exchange: its physiological implications, *Physiol Rev 79*, 763-854.
91. Prins, D., and Michalak, M. (2011) Organellar calcium buffers, *Cold Spring Harb Perspect Biol 3*.
92. Low-Nam, S.; Lidke, K.; Cutler, P.; Roovers, R.; van Bergen en Henegouwen, P.; Wilson, B.; Lidke, D. Erbb1 Dimerization Is Promoted By Domain Co-Confinement And Stabilized By Ligand Binding. *Nat Struct Mol Biol* 2011, *18*, 1244-1249.
93. Valley, C.; Arndt-Jovin, D.; Karedla, N.; Steinkamp, M.; Chizhik, A.; Hlavacek, W.; Wilson, B.; Lidke, K.; Lidke, D. Enhanced Dimerization Drives Ligand-Independent Activity of Mutant EGFR In Lung Cancer. *Molecular Biology of the Cell* 2015.
94. Schütz, G.; Schindler, H.; Schmidt, T. Single-Molecule Microscopy on Model Membranes Reveals Anomalous Diffusion. *Biophysical Journal* 1997, *73*, 1073-1080.

Appendix

The following code is used in the analysis of the SPT data of erbB1 to determination of the number of states using distances between all pairwise receptors and speeds of individual receptors as well as the correlation analysis between the approach speeds and pairwise distances.

```
  %Determine the individual x- and y- coordinates for each receptor for
  %each channel and put it into one array
  ch1coordsx=squeeze(HMM_Data.raw_ch1_tracks(:,: ,1));
  ch1coordsy=squeeze(HMM_Data.raw_ch1_tracks(:,: ,2));
  ch2coordsx=squeeze(HMM_Data.ch2_tracks(:,: ,1));
  ch2coordsy=squeeze(HMM_Data.ch2_tracks(:,:,2));
  coordsx=cat(1,ch1coordsx,ch2coordsx);
  coordsy=cat(1,ch1coordsy,ch2coordsy);

  %time between each frame
  deltatime=5e-2; %seconds
  %number of frames and total number of receptors
  framemax=999; %wil usually be 999
  %number of total receptors
  trackmax=size(HMM_Data.raw_ch1_tracks)+size(HMM_Data.ch2_tracks);

  %determine the distance between each pair of receptors
       for frame=1:framemax;
           for track=1:trackmax(1);
               for track0=track:trackmax(1);
                distancex(track,track0,frame)=coordsx(track,frame)-
coordsx(track0,frame);
               end;
           end;
       end;

       for frame=1:framemax;
           for track=1:trackmax(1);
               for track0=1:trackmax(1);
               distancey(track,track0,frame)=coordsy(track,frame)-
coordsy(track0,frame);
               end;
           end;
       end;

       distanceR2=sqrt(distancex.^2+distancey.^2);
       %account for the fact that one pixel=167 nm
       R2adjust=1.67E-7*distanceR2;

       %Pairwise distance histogram analysis
       PairwiseDist=[];
       for frame=1:framemax;
           frame
           for track=1:trackmax(1);
               AllR2adjust=R2adjust(track,:,frame);
               AllR2adjust(isnan(AllR2adjust))=[];
               AllR2adjustwozeros=[];
               AllR2adjustwozeros=AllR2adjust(AllR2adjust~=0);
```

```
            PairwiseDist=[PairwiseDist,AllR2adjustwozeros];
        end;
    end;

    edges=[0.0000E+00    4.0000E-08  8.0000E-08  1.2000E-07
1.6000E-07  2.0000E-07  2.4000E-07  2.8000E-07  3.2000E-07  3.6000E-07
4.0000E-07  4.4000E-07  4.8000E-07  5.2000E-07  5.6000E-07  6.0000E-07
6.4000E-07  6.8000E-07  7.2000E-07  7.6000E-07  8.0000E-07  8.4000E-07
8.8000E-07  9.2000E-07  9.6000E-07  1.0000E-06  1.0400E-06  1.0800E-06
1.1200E-06  1.1600E-06  1.2000E-06  1.2400E-06  1.2800E-06  1.3200E-06
1.3600E-06  1.4000E-06  1.4400E-06  1.4800E-06  1.5200E-06  1.5600E-06
1.6000E-06  1.6400E-06  1.6800E-06  1.7200E-06  1.7600E-06  1.8000E-06
1.8400E-06  1.8800E-06  1.9200E-06  1.9600E-06  2.0000E-06  2.0400E-06
2.0800E-06  2.1200E-06  2.1600E-06  2.2000E-06  2.2400E-06  2.2800E-06
2.3200E-06  2.3600E-06  2.4000E-06  2.4400E-06  2.4800E-06  2.5200E-06
2.5600E-06  2.6000E-06  2.6400E-06  2.6800E-06  2.7200E-06  2.7600E-06
2.8000E-06  2.8400E-06  2.8800E-06  2.9200E-06  2.9600E-06  3.0000E-06
3.0400E-06  3.0800E-06  3.1200E-06  3.1600E-06  3.2000E-06  3.2400E-06
3.2800E-06  3.3200E-06  3.3600E-06  3.4000E-06  3.4400E-06  3.4800E-06
3.5200E-06  3.5600E-06  3.6000E-06  3.6400E-06  3.6800E-06  3.7200E-06
3.7600E-06  3.8000E-06  3.8400E-06  3.8800E-06  3.9200E-06  3.9600E-06
4.0000E-06  4.0400E-06  4.0800E-06  4.1200E-06  4.1600E-06  4.2000E-06
4.2400E-06  4.2800E-06  4.3200E-06  4.3600E-06  4.4000E-06  4.4400E-06
4.4800E-06  4.5200E-06  4.5600E-06  4.6000E-06  4.6400E-06  4.6800E-06
4.7200E-06  4.7600E-06  4.8000E-06  4.8400E-06  4.8800E-06  4.9200E-06
4.9600E-06  5.0000E-06  5.0400E-06  5.0800E-06  5.1200E-06  5.1600E-06
5.2000E-06  5.2400E-06  5.2800E-06  5.3200E-06  5.3600E-06  5.4000E-06
5.4400E-06  5.4800E-06  5.5200E-06  5.5600E-06  5.6000E-06  5.6400E-06
5.6800E-06  5.7200E-06  5.7600E-06  5.8000E-06  5.8400E-06  5.8800E-06
5.9200E-06  5.9600E-06  6.0000E-06  6.0400E-06  6.0800E-06  6.1200E-06
6.1600E-06  6.2000E-06  6.2400E-06  6.2800E-06  6.3200E-06  6.3600E-06
6.4000E-06  6.4400E-06  6.4800E-06  6.5200E-06  6.5600E-06  6.6000E-06
6.6400E-06  6.6800E-06  6.7200E-06  6.7600E-06  6.8000E-06  6.8400E-06
6.8800E-06  6.9200E-06  6.9600E-06  7.0000E-06  7.0400E-06  7.0800E-06
7.1200E-06  7.1600E-06  7.2000E-06  7.2400E-06  7.2800E-06  7.3200E-06
7.3600E-06  7.4000E-06  7.4400E-06  7.4800E-06  7.5200E-06  7.5600E-06
7.6000E-06  7.6400E-06  7.6800E-06  7.7200E-06  7.7600E-06  7.8000E-06
7.8400E-06  7.8800E-06  7.9200E-06  7.9600E-06  8.0000E-06  8.0400E-06
8.0800E-06  8.1200E-06  8.1600E-06  8.2000E-06  8.2400E-06  8.2800E-06
8.3200E-06  8.3600E-06  8.4000E-06  8.4400E-06  8.4800E-06  8.5200E-06
8.5600E-06  8.6000E-06  8.6400E-06  8.6800E-06  8.7200E-06  8.7600E-06
8.8000E-06  8.8400E-06  8.8800E-06  8.9200E-06  8.9600E-06  9.0000E-06
9.0400E-06  9.0800E-06  9.1200E-06  9.1600E-06  9.2000E-06  9.2400E-06
9.2800E-06  9.3200E-06  9.3600E-06  9.4000E-06  9.4400E-06  9.4800E-06
9.5200E-06  9.5600E-06  9.6000E-06  9.6400E-06  9.6800E-06  9.7200E-06
9.7600E-06  9.8000E-06  9.8400E-06  9.8800E-06  9.9200E-06  9.9600E-06
1.0000E-05  1.0040E-05  1.0080E-05  1.0120E-05  1.0160E-05  1.0200E-05
1.0240E-05  1.0280E-05  1.0320E-05  1.0360E-05  1.0400E-05  1.0440E-05
1.0480E-05  1.0520E-05  1.0560E-05  1.0600E-05  1.0640E-05  1.0680E-05
1.0720E-05  1.0760E-05  1.0800E-05  1.0840E-05  1.0880E-05  1.0920E-05
1.0960E-05  1.1000E-05  1.1040E-05  1.1080E-05  1.1120E-05  1.1160E-05
1.1200E-05  1.1240E-05  1.1280E-05  1.1320E-05  1.1360E-05  1.1400E-05
1.1440E-05  1.1480E-05  1.1520E-05  1.1560E-05  1.1600E-05  1.1640E-05
1.1680E-05  1.1720E-05  1.1760E-05  1.1800E-05  1.1840E-05  1.1880E-05
1.1920E-05  1.1960E-05  1.2000E-05  1.2040E-05  1.2080E-05  1.2120E-05
1.2160E-05  1.2200E-05  1.2240E-05  1.2280E-05  1.2320E-05  1.2360E-05
1.2400E-05  1.2440E-05  1.2480E-05  1.2520E-05  1.2560E-05  1.2600E-05
```

1.2640E-05	1.2680E-05	1.2720E-05	1.2760E-05	1.2800E-05	1.2840E-05
1.2880E-05	1.2920E-05	1.2960E-05	1.3000E-05	1.3040E-05	1.3080E-05
1.3120E-05	1.3160E-05	1.3200E-05	1.3240E-05	1.3280E-05	1.3320E-05
1.3360E-05	1.3400E-05	1.3440E-05	1.3480E-05	1.3520E-05	1.3560E-05
1.3600E-05	1.3640E-05	1.3680E-05	1.3720E-05	1.3760E-05	1.3800E-05
1.3840E-05	1.3880E-05	1.3920E-05	1.3960E-05	1.4000E-05	1.4040E-05
1.4080E-05	1.4120E-05	1.4160E-05	1.4200E-05	1.4240E-05	1.4280E-05
1.4320E-05	1.4360E-05	1.4400E-05	1.4440E-05	1.4480E-05	1.4520E-05
1.4560E-05	1.4600E-05	1.4640E-05	1.4680E-05	1.4720E-05	1.4760E-05
1.4800E-05	1.4840E-05	1.4880E-05	1.4920E-05	1.4960E-05	1.5000E-05
1.5040E-05	1.5080E-05	1.5120E-05	1.5160E-05	1.5200E-05	1.5240E-05
1.5280E-05	1.5320E-05	1.5360E-05	1.5400E-05	1.5440E-05	1.5480E-05
1.5520E-05	1.5560E-05	1.5600E-05	1.5640E-05	1.5680E-05	1.5720E-05
1.5760E-05	1.5800E-05	1.5840E-05	1.5880E-05	1.5920E-05	1.5960E-05
1.6000E-05	1.6040E-05	1.6080E-05	1.6120E-05	1.6160E-05	1.6200E-05
1.6240E-05	1.6280E-05	1.6320E-05	1.6360E-05	1.6400E-05	1.6440E-05
1.6480E-05	1.6520E-05	1.6560E-05	1.6600E-05	1.6640E-05	1.6680E-05
1.6720E-05	1.6760E-05	1.6800E-05	1.6840E-05	1.6880E-05	1.6920E-05
1.6960E-05	1.7000E-05	1.7040E-05	1.7080E-05	1.7120E-05	1.7160E-05
1.7200E-05	1.7240E-05	1.7280E-05	1.7320E-05	1.7360E-05	1.7400E-05
1.7440E-05	1.7480E-05	1.7520E-05	1.7560E-05	1.7600E-05	1.7640E-05
1.7680E-05	1.7720E-05	1.7760E-05	1.7800E-05	1.7840E-05	1.7880E-05
1.7920E-05	1.7960E-05	1.8000E-05	1.8040E-05	1.8080E-05	1.8120E-05
1.8160E-05	1.8200E-05	1.8240E-05	1.8280E-05	1.8320E-05	1.8360E-05
1.8400E-05	1.8440E-05	1.8480E-05	1.8520E-05	1.8560E-05	1.8600E-05
1.8640E-05	1.8680E-05	1.8720E-05	1.8760E-05	1.8800E-05	1.8840E-05
1.8880E-05	1.8920E-05	1.8960E-05	1.9000E-05	1.9040E-05	1.9080E-05
1.9120E-05	1.9160E-05	1.9200E-05	1.9240E-05	1.9280E-05	1.9320E-05
1.9360E-05	1.9400E-05	1.9440E-05	1.9480E-05	1.9520E-05	1.9560E-05
1.9600E-05	1.9640E-05	1.9680E-05	1.9720E-05	1.9760E-05	1.9800E-05
1.9840E-05	1.9880E-05	1.9920E-05	1.9960E-05	2.0000E-05	2.0040E-05
2.0080E-05	2.0120E-05	2.0160E-05	2.0200E-05	2.0240E-05	2.0280E-05
2.0320E-05	2.0360E-05	2.0400E-05	2.0440E-05	2.0480E-05	2.0520E-05
2.0560E-05	2.0600E-05	2.0640E-05	2.0680E-05	2.0720E-05	2.0760E-05
2.0800E-05	2.0840E-05	2.0880E-05	2.0920E-05	2.0960E-05	2.1000E-05
2.1040E-05	2.1080E-05	2.1120E-05	2.1160E-05	2.1200E-05	2.1240E-05
2.1280E-05	2.1320E-05	2.1360E-05	2.1400E-05	2.1440E-05	2.1480E-05
2.1520E-05	2.1560E-05	2.1600E-05	2.1640E-05	2.1680E-05	2.1720E-05
2.1760E-05	2.1800E-05	2.1840E-05	2.1880E-05	2.1920E-05	2.1960E-05
2.2000E-05	2.2040E-05	2.2080E-05	2.2120E-05	2.2160E-05	2.2200E-05
2.2240E-05	2.2280E-05	2.2320E-05	2.2360E-05	2.2400E-05	2.2440E-05
2.2480E-05	2.2520E-05	2.2560E-05	2.2600E-05	2.2640E-05	2.2680E-05
2.2720E-05	2.2760E-05	2.2800E-05	2.2840E-05	2.2880E-05	2.2920E-05
2.2960E-05	2.3000E-05	2.3040E-05	2.3080E-05	2.3120E-05	2.3160E-05
2.3200E-05	2.3240E-05	2.3280E-05	2.3320E-05	2.3360E-05	2.3400E-05
2.3440E-05	2.3480E-05	2.3520E-05	2.3560E-05	2.3600E-05	2.3640E-05
2.3680E-05	2.3720E-05	2.3760E-05	2.3800E-05	2.3840E-05	2.3880E-05
2.3920E-05	2.3960E-05	2.4000E-05	2.4040E-05	2.4080E-05	2.4120E-05
2.4160E-05	2.4200E-05	2.4240E-05	2.4280E-05	2.4320E-05	2.4360E-05
2.4400E-05	2.4440E-05	2.4480E-05	2.4520E-05	2.4560E-05	2.4600E-05
2.4640E-05	2.4680E-05	2.4720E-05	2.4760E-05	2.4800E-05	2.4840E-05
2.4880E-05	2.4920E-05	2.4960E-05	2.5000E-05	2.5040E-05	2.5080E-05
2.5120E-05	2.5160E-05	2.5200E-05	2.5240E-05	2.5280E-05	2.5320E-05
2.5360E-05	2.5400E-05	2.5440E-05	2.5480E-05	2.5520E-05	2.5560E-05
2.5600E-05	2.5640E-05	2.5680E-05	2.5720E-05	2.5760E-05	2.5800E-05
2.5840E-05	2.5880E-05	2.5920E-05	2.5960E-05	2.6000E-05	2.6040E-05
2.6080E-05	2.6120E-05	2.6160E-05	2.6200E-05	2.6240E-05	2.6280E-05

```
2.6320E-05  2.6360E-05  2.6400E-05  2.6440E-05  2.6480E-05  2.6520E-05
2.6560E-05  2.6600E-05  2.6640E-05  2.6680E-05  2.6720E-05  2.6760E-05
2.6800E-05  2.6840E-05  2.6880E-05  2.6920E-05  2.6960E-05  2.7000E-05
2.7040E-05  2.7080E-05  2.7120E-05  2.7160E-05  2.7200E-05  2.7240E-05
2.7280E-05  2.7320E-05  2.7360E-05  2.7400E-05  2.7440E-05  2.7480E-05
2.7520E-05  2.7560E-05  2.7600E-05  2.7640E-05  2.7680E-05  2.7720E-05
2.7760E-05  2.7800E-05  2.7840E-05  2.7880E-05  2.7920E-05  2.7960E-05
2.8000E-05  2.8040E-05  2.8080E-05  2.8120E-05  2.8160E-05  2.8200E-05
2.8240E-05  2.8280E-05  2.8320E-05  2.8360E-05  2.8400E-05  2.8440E-05
2.8480E-05  2.8520E-05  2.8560E-05  2.8600E-05  2.8640E-05  2.8680E-05
2.8720E-05  2.8760E-05  2.8800E-05  2.8840E-05  2.8880E-05  2.8920E-05
2.8960E-05  2.9000E-05  2.9040E-05  2.9080E-05  2.9120E-05  2.9160E-05
2.9200E-05  2.9240E-05  2.9280E-05  2.9320E-05  2.9360E-05  2.9400E-05
2.9440E-05  2.9480E-05  2.9520E-05  2.9560E-05  2.9600E-05  2.9640E-05
2.9680E-05  2.9720E-05  2.9760E-05  2.9800E-05  2.9840E-05  2.9880E-05
2.9920E-05  2.9960E-05  3.0000E-05]
       figure
       hist(PairwiseDist,edges)
       PairwiseDistHist=hist(PairwiseDist,edges)


       %Determine the total velocity of each receptor from the x- and
y-
       %velocity components


       for frame=1:framemax;
           for track=1:trackmax(1);
               Vx(track,frame)=[coordsx(track,frame)-
(coordsx(track,frame+1))]/deltatime;
               Vy(track,frame)=[coordsy(track,frame)-
(coordsy(track,frame+1))]/deltatime;
               V=sqrt(Vx.^2+Vy.^2);
           end;
       end;

       Vxadjust=1.67E-7*Vx;
       Vyadjust=1.67E-7*Vy;
       Vadjust=1.67E-7*V;

       %Pairwise distance histogram analysis
       Velocity=[];
       for frame=1:framemax;
           frame
           for track=1:trackmax(1);
               AllVelocity=Vadjust(track,frame);
               AllVelocity(isnan(AllVelocity))=[];
               AllVelocitywozeros=[];
               AllVelocitywozeros=AllVelocity(AllVelocity~=0);
               Velocity=[Velocity,AllVelocitywozeros];
           end;
       end;

       edges=[0 5.00E-06    1.00E-05    1.50E-05    2.00E-05    2.50E-
05    3.00E-05    3.50E-05    4.00E-05    4.50E-05    5.00E-05
```

```
5.50E-05    6.00E-05    6.50E-05    7.00E-05    7.50E-05    8.00E-05
8.50E-05    9.00E-05    9.50E-05    1.00E-04    1.05E-04    1.10E-04
1.15E-04    1.20E-04    1.25E-04    1.30E-04    1.35E-04    1.40E-04
1.45E-04    1.50E-04    1.55E-04    1.60E-04    1.65E-04    1.70E-04
1.75E-04    1.80E-04    1.85E-04    1.90E-04    1.95E-04    2.00E-04
2.05E-04    2.10E-04    2.15E-04    2.20E-04    2.25E-04    2.30E-04
2.35E-04    2.40E-04    2.45E-04    2.50E-04    2.55E-04    2.60E-04
2.65E-04    2.70E-04    2.75E-04    2.80E-04    2.85E-04    2.90E-04
2.95E-04    3.00E-04    3.05E-04    3.10E-04    3.15E-04    3.20E-04
3.25E-04    3.30E-04    3.35E-04    3.40E-04    3.45E-04    3.50E-04
3.55E-04    3.60E-04    3.65E-04    3.70E-04    3.75E-04    3.80E-04
3.85E-04    3.90E-04    3.95E-04    4.00E-04    4.05E-04    4.10E-04
4.15E-04    4.20E-04    4.25E-04    4.30E-04    4.35E-04    4.40E-04
4.45E-04    4.50E-04    4.55E-04    4.60E-04    4.65E-04    4.70E-04
4.75E-04    4.80E-04    4.85E-04    4.90E-04    4.95E-04    5.00E-04]
       figure
       hist(Velocity,edges)
       VelocityHist=hist(Velocity,edges);


       %Determine the relative velocity between each pair of receptors
       for frame=1:framemax;
           for track=1:trackmax(1);
               for track0=track:trackmax(1);
                RelVx(track,track0,frame)=Vxadjust(track,frame)-
Vxadjust(track0,frame);
               end;
           end;
       end;

       for frame=1:framemax;
           for track=1:trackmax(1);
               for track0=1:trackmax(1);
               RelVy(track,track0,frame)=Vyadjust(track,frame)-
Vyadjust(track0,frame);
               end;
           end;
       end;

      RelV=sqrt(RelVx.^2+RelVy.^2);
      RelVadjust=1.67E-7*RelV;

  %correlation analysis between distances and approach velocities

  correlation=corrcoef(R2adjust,RelVadjust)


  %Need to break down the the correlation to see how it looks at every
  %given time point

  RelVadjust2=reshape(RelVadjust,[trackmax(1),trackmax(1)*framemax]);
  R2adjust2=reshape(R2adjust,[trackmax(1),trackmax(1)*framemax]);

  a=9; %usually 9 because 999 is divisible easily by 9
```

```
corr1=corrcoef(R2adjust2(1:trackmax(1),1:trackmax(1)*a),RelVadjust2(1:t
rackmax(1),1:trackmax(1)*a));

corr2=corrcoef(R2adjust2(1:trackmax(1),trackmax(1)*a+1:trackmax(1)*a*2)
,RelVadjust2(1:trackmax(1),trackmax(1)*a+1:trackmax(1)*a*2));

corr3=corrcoef(R2adjust2(1:trackmax(1),trackmax(1)*a*2+1:trackmax(1)*a*
3),RelVadjust2(1:trackmax(1),trackmax(1)*a*2+1:trackmax(1)*a*3));

corr4=corrcoef(R2adjust2(1:trackmax(1),trackmax(1)*a*3+1:trackmax(1)*a*
4),RelVadjust2(1:trackmax(1),trackmax(1)*a*3+1:trackmax(1)*a*4));

corr5=corrcoef(R2adjust2(1:trackmax(1),trackmax(1)*a*4+1:trackmax(1)*a*
5),RelVadjust2(1:trackmax(1),trackmax(1)*a*4+1:trackmax(1)*a*5));

corr6=corrcoef(R2adjust2(1:trackmax(1),trackmax(1)*a*5+1:trackmax(1)*a*
6),RelVadjust2(1:trackmax(1),trackmax(1)*a*5+1:trackmax(1)*a*6));

corr7=corrcoef(R2adjust2(1:trackmax(1),trackmax(1)*a*6+1:trackmax(1)*a*
7),RelVadjust2(1:trackmax(1),trackmax(1)*a*6+1:trackmax(1)*a*7));

corr8=corrcoef(R2adjust2(1:trackmax(1),trackmax(1)*a*7+1:trackmax(1)*a*
8),RelVadjust2(1:trackmax(1),trackmax(1)*a*7+1:trackmax(1)*a*8));

corr9=corrcoef(R2adjust2(1:trackmax(1),trackmax(1)*a*8+1:trackmax(1)*a*
9),RelVadjust2(1:trackmax(1),trackmax(1)*a*8+1:trackmax(1)*a*9));

corr10=corrcoef(R2adjust2(1:trackmax(1),trackmax(1)*a*9+1:trackmax(1)*a
*10),RelVadjust2(1:trackmax(1),trackmax(1)*a*9+1:trackmax(1)*a*10));

corr11=corrcoef(R2adjust2(1:trackmax(1),trackmax(1)*a*10+1:trackmax(1)*
a*11),RelVadjust2(1:trackmax(1),trackmax(1)*a*10+1:trackmax(1)*a*11));

corr12=corrcoef(R2adjust2(1:trackmax(1),trackmax(1)*a*11+1:trackmax(1)*
a*12),RelVadjust2(1:trackmax(1),trackmax(1)*a*11+1:trackmax(1)*a*12));

corr13=corrcoef(R2adjust2(1:trackmax(1),trackmax(1)*a*12+1:trackmax(1)*
a*13),RelVadjust2(1:trackmax(1),trackmax(1)*a*12+1:trackmax(1)*a*13));

corr14=corrcoef(R2adjust2(1:trackmax(1),trackmax(1)*a*13+1:trackmax(1)*
a*14),RelVadjust2(1:trackmax(1),trackmax(1)*a*13+1:trackmax(1)*a*14));

corr15=corrcoef(R2adjust2(1:trackmax(1),trackmax(1)*a*14+1:trackmax(1)*
a*15),RelVadjust2(1:trackmax(1),trackmax(1)*a*14+1:trackmax(1)*a*15));

corr16=corrcoef(R2adjust2(1:trackmax(1),trackmax(1)*a*15+1:trackmax(1)*
a*16),RelVadjust2(1:trackmax(1),trackmax(1)*a*15+1:trackmax(1)*a*16));

corr17=corrcoef(R2adjust2(1:trackmax(1),trackmax(1)*a*16+1:trackmax(1)*
a*17),RelVadjust2(1:trackmax(1),trackmax(1)*a*16+1:trackmax(1)*a*17));

corr18=corrcoef(R2adjust2(1:trackmax(1),trackmax(1)*a*17+1:trackmax(1)*
a*18),RelVadjust2(1:trackmax(1),trackmax(1)*a*17+1:trackmax(1)*a*18));

corr19=corrcoef(R2adjust2(1:trackmax(1),trackmax(1)*a*18+1:trackmax(1)*
a*19),RelVadjust2(1:trackmax(1),trackmax(1)*a*18+1:trackmax(1)*a*19));
```

```
corr20=corrcoef(R2adjust2(1:trackmax(1),trackmax(1)*a*19+1:trackmax(1)*
a*20),RelVadjust2(1:trackmax(1),trackmax(1)*a*19+1:trackmax(1)*a*20));

corr21=corrcoef(R2adjust2(1:trackmax(1),trackmax(1)*a*20+1:trackmax(1)*
a*21),RelVadjust2(1:trackmax(1),trackmax(1)*a*20+1:trackmax(1)*a*21));

corr22=corrcoef(R2adjust2(1:trackmax(1),trackmax(1)*a*21+1:trackmax(1)*
a*22),RelVadjust2(1:trackmax(1),trackmax(1)*a*21+1:trackmax(1)*a*22));

corr23=corrcoef(R2adjust2(1:trackmax(1),trackmax(1)*a*22+1:trackmax(1)*
a*23),RelVadjust2(1:trackmax(1),trackmax(1)*a*22+1:trackmax(1)*a*23));

corr24=corrcoef(R2adjust2(1:trackmax(1),trackmax(1)*a*23+1:trackmax(1)*
a*24),RelVadjust2(1:trackmax(1),trackmax(1)*a*23+1:trackmax(1)*a*24));

corr25=corrcoef(R2adjust2(1:trackmax(1),trackmax(1)*a*24+1:trackmax(1)*
a*25),RelVadjust2(1:trackmax(1),trackmax(1)*a*24+1:trackmax(1)*a*25));

corr26=corrcoef(R2adjust2(1:trackmax(1),trackmax(1)*a*25+1:trackmax(1)*
a*26),RelVadjust2(1:trackmax(1),trackmax(1)*a*25+1:trackmax(1)*a*26));

corr27=corrcoef(R2adjust2(1:trackmax(1),trackmax(1)*a*26+1:trackmax(1)*
a*27),RelVadjust2(1:trackmax(1),trackmax(1)*a*26+1:trackmax(1)*a*27));

corr28=corrcoef(R2adjust2(1:trackmax(1),trackmax(1)*a*27+1:trackmax(1)*
a*28),RelVadjust2(1:trackmax(1),trackmax(1)*a*27+1:trackmax(1)*a*28));

corr29=corrcoef(R2adjust2(1:trackmax(1),trackmax(1)*a*28+1:trackmax(1)*
a*29),RelVadjust2(1:trackmax(1),trackmax(1)*a*28+1:trackmax(1)*a*29));

corr30=corrcoef(R2adjust2(1:trackmax(1),trackmax(1)*a*29+1:trackmax(1)*
a*30),RelVadjust2(1:trackmax(1),trackmax(1)*a*29+1:trackmax(1)*a*30));

corr31=corrcoef(R2adjust2(1:trackmax(1),trackmax(1)*a*30+1:trackmax(1)*
a*31),RelVadjust2(1:trackmax(1),trackmax(1)*a*30+1:trackmax(1)*a*31));

corr32=corrcoef(R2adjust2(1:trackmax(1),trackmax(1)*a*31+1:trackmax(1)*
a*32),RelVadjust2(1:trackmax(1),trackmax(1)*a*31+1:trackmax(1)*a*32));

corr33=corrcoef(R2adjust2(1:trackmax(1),trackmax(1)*a*32+1:trackmax(1)*
a*33),RelVadjust2(1:trackmax(1),trackmax(1)*a*32+1:trackmax(1)*a*33));

corr34=corrcoef(R2adjust2(1:trackmax(1),trackmax(1)*a*33+1:trackmax(1)*
a*34),RelVadjust2(1:trackmax(1),trackmax(1)*a*33+1:trackmax(1)*a*34));

corr35=corrcoef(R2adjust2(1:trackmax(1),trackmax(1)*a*34+1:trackmax(1)*
a*35),RelVadjust2(1:trackmax(1),trackmax(1)*a*34+1:trackmax(1)*a*35));

corr36=corrcoef(R2adjust2(1:trackmax(1),trackmax(1)*a*35+1:trackmax(1)*
a*36),RelVadjust2(1:trackmax(1),trackmax(1)*a*35+1:trackmax(1)*a*36));

corr37=corrcoef(R2adjust2(1:trackmax(1),trackmax(1)*a*36+1:trackmax(1)*
a*37),RelVadjust2(1:trackmax(1),trackmax(1)*a*36+1:trackmax(1)*a*37));

corr38=corrcoef(R2adjust2(1:trackmax(1),trackmax(1)*a*37+1:trackmax(1)*
a*38),RelVadjust2(1:trackmax(1),trackmax(1)*a*37+1:trackmax(1)*a*38));
```

```
corr39=corrcoef(R2adjust2(1:trackmax(1),trackmax(1)*a*38+1:trackmax(1)*
a*39),RelVadjust2(1:trackmax(1),trackmax(1)*a*38+1:trackmax(1)*a*39));

corr40=corrcoef(R2adjust2(1:trackmax(1),trackmax(1)*a*39+1:trackmax(1)*
a*40),RelVadjust2(1:trackmax(1),trackmax(1)*a*39+1:trackmax(1)*a*40));

corr41=corrcoef(R2adjust2(1:trackmax(1),trackmax(1)*a*40+1:trackmax(1)*
a*41),RelVadjust2(1:trackmax(1),trackmax(1)*a*40+1:trackmax(1)*a*41));

corr42=corrcoef(R2adjust2(1:trackmax(1),trackmax(1)*a*41+1:trackmax(1)*
a*42),RelVadjust2(1:trackmax(1),trackmax(1)*a*41+1:trackmax(1)*a*42));

corr43=corrcoef(R2adjust2(1:trackmax(1),trackmax(1)*a*42+1:trackmax(1)*
a*43),RelVadjust2(1:trackmax(1),trackmax(1)*a*42+1:trackmax(1)*a*43));

corr44=corrcoef(R2adjust2(1:trackmax(1),trackmax(1)*a*43+1:trackmax(1)*
a*44),RelVadjust2(1:trackmax(1),trackmax(1)*a*43+1:trackmax(1)*a*44));

corr45=corrcoef(R2adjust2(1:trackmax(1),trackmax(1)*a*44+1:trackmax(1)*
a*45),RelVadjust2(1:trackmax(1),trackmax(1)*a*44+1:trackmax(1)*a*45));

corr46=corrcoef(R2adjust2(1:trackmax(1),trackmax(1)*a*45+1:trackmax(1)*
a*46),RelVadjust2(1:trackmax(1),trackmax(1)*a*45+1:trackmax(1)*a*46));

corr47=corrcoef(R2adjust2(1:trackmax(1),trackmax(1)*a*46+1:trackmax(1)*
a*47),RelVadjust2(1:trackmax(1),trackmax(1)*a*46+1:trackmax(1)*a*47));

corr48=corrcoef(R2adjust2(1:trackmax(1),trackmax(1)*a*47+1:trackmax(1)*
a*48),RelVadjust2(1:trackmax(1),trackmax(1)*a*47+1:trackmax(1)*a*48));

corr49=corrcoef(R2adjust2(1:trackmax(1),trackmax(1)*a*48+1:trackmax(1)*
a*49),RelVadjust2(1:trackmax(1),trackmax(1)*a*48+1:trackmax(1)*a*49));

corr50=corrcoef(R2adjust2(1:trackmax(1),trackmax(1)*a*49+1:trackmax(1)*
a*50),RelVadjust2(1:trackmax(1),trackmax(1)*a*49+1:trackmax(1)*a*50));

corr51=corrcoef(R2adjust2(1:trackmax(1),trackmax(1)*a*50+1:trackmax(1)*
a*51),RelVadjust2(1:trackmax(1),trackmax(1)*a*50+1:trackmax(1)*a*51));

corr52=corrcoef(R2adjust2(1:trackmax(1),trackmax(1)*a*51+1:trackmax(1)*
a*52),RelVadjust2(1:trackmax(1),trackmax(1)*a*51+1:trackmax(1)*a*52));

corr53=corrcoef(R2adjust2(1:trackmax(1),trackmax(1)*a*52+1:trackmax(1)*
a*53),RelVadjust2(1:trackmax(1),trackmax(1)*a*52+1:trackmax(1)*a*53));

corr54=corrcoef(R2adjust2(1:trackmax(1),trackmax(1)*a*53+1:trackmax(1)*
a*54),RelVadjust2(1:trackmax(1),trackmax(1)*a*53+1:trackmax(1)*a*54));

corr55=corrcoef(R2adjust2(1:trackmax(1),trackmax(1)*a*54+1:trackmax(1)*
a*55),RelVadjust2(1:trackmax(1),trackmax(1)*a*54+1:trackmax(1)*a*55));

corr56=corrcoef(R2adjust2(1:trackmax(1),trackmax(1)*a*55+1:trackmax(1)*
a*56),RelVadjust2(1:trackmax(1),trackmax(1)*a*55+1:trackmax(1)*a*56));

corr57=corrcoef(R2adjust2(1:trackmax(1),trackmax(1)*a*56+1:trackmax(1)*
a*57),RelVadjust2(1:trackmax(1),trackmax(1)*a*56+1:trackmax(1)*a*57));
```

```
corr58=corrcoef(R2adjust2(1:trackmax(1),trackmax(1)*a*57+1:trackmax(1)*
a*58),RelVadjust2(1:trackmax(1),trackmax(1)*a*57+1:trackmax(1)*a*58));

corr59=corrcoef(R2adjust2(1:trackmax(1),trackmax(1)*a*58+1:trackmax(1)*
a*59),RelVadjust2(1:trackmax(1),trackmax(1)*a*58+1:trackmax(1)*a*59));

corr60=corrcoef(R2adjust2(1:trackmax(1),trackmax(1)*a*59+1:trackmax(1)*
a*60),RelVadjust2(1:trackmax(1),trackmax(1)*a*59+1:trackmax(1)*a*60));

corr61=corrcoef(R2adjust2(1:trackmax(1),trackmax(1)*a*60+1:trackmax(1)*
a*61),RelVadjust2(1:trackmax(1),trackmax(1)*a*60+1:trackmax(1)*a*61));

corr62=corrcoef(R2adjust2(1:trackmax(1),trackmax(1)*a*61+1:trackmax(1)*
a*62),RelVadjust2(1:trackmax(1),trackmax(1)*a*61+1:trackmax(1)*a*62));

corr63=corrcoef(R2adjust2(1:trackmax(1),trackmax(1)*a*62+1:trackmax(1)*
a*63),RelVadjust2(1:trackmax(1),trackmax(1)*a*62+1:trackmax(1)*a*63));

corr64=corrcoef(R2adjust2(1:trackmax(1),trackmax(1)*a*63+1:trackmax(1)*
a*64),RelVadjust2(1:trackmax(1),trackmax(1)*a*63+1:trackmax(1)*a*64));

corr65=corrcoef(R2adjust2(1:trackmax(1),trackmax(1)*a*64+1:trackmax(1)*
a*65),RelVadjust2(1:trackmax(1),trackmax(1)*a*64+1:trackmax(1)*a*65));

corr66=corrcoef(R2adjust2(1:trackmax(1),trackmax(1)*a*65+1:trackmax(1)*
a*66),RelVadjust2(1:trackmax(1),trackmax(1)*a*65+1:trackmax(1)*a*66));

corr67=corrcoef(R2adjust2(1:trackmax(1),trackmax(1)*a*66+1:trackmax(1)*
a*67),RelVadjust2(1:trackmax(1),trackmax(1)*a*66+1:trackmax(1)*a*67));

corr68=corrcoef(R2adjust2(1:trackmax(1),trackmax(1)*a*67+1:trackmax(1)*
a*68),RelVadjust2(1:trackmax(1),trackmax(1)*a*67+1:trackmax(1)*a*68));

corr69=corrcoef(R2adjust2(1:trackmax(1),trackmax(1)*a*68+1:trackmax(1)*
a*69),RelVadjust2(1:trackmax(1),trackmax(1)*a*68+1:trackmax(1)*a*69));

corr70=corrcoef(R2adjust2(1:trackmax(1),trackmax(1)*a*69+1:trackmax(1)*
a*70),RelVadjust2(1:trackmax(1),trackmax(1)*a*69+1:trackmax(1)*a*70));

corr71=corrcoef(R2adjust2(1:trackmax(1),trackmax(1)*a*70+1:trackmax(1)*
a*71),RelVadjust2(1:trackmax(1),trackmax(1)*a*70+1:trackmax(1)*a*71));

corr72=corrcoef(R2adjust2(1:trackmax(1),trackmax(1)*a*71+1:trackmax(1)*
a*72),RelVadjust2(1:trackmax(1),trackmax(1)*a*71+1:trackmax(1)*a*72));

corr73=corrcoef(R2adjust2(1:trackmax(1),trackmax(1)*a*72+1:trackmax(1)*
a*73),RelVadjust2(1:trackmax(1),trackmax(1)*a*72+1:trackmax(1)*a*73));

corr74=corrcoef(R2adjust2(1:trackmax(1),trackmax(1)*a*73+1:trackmax(1)*
a*74),RelVadjust2(1:trackmax(1),trackmax(1)*a*73+1:trackmax(1)*a*74));

corr75=corrcoef(R2adjust2(1:trackmax(1),trackmax(1)*a*74+1:trackmax(1)*
a*75),RelVadjust2(1:trackmax(1),trackmax(1)*a*74+1:trackmax(1)*a*75));

corr76=corrcoef(R2adjust2(1:trackmax(1),trackmax(1)*a*75+1:trackmax(1)*
a*76),RelVadjust2(1:trackmax(1),trackmax(1)*a*75+1:trackmax(1)*a*76));
```

```
corr77=corrcoef(R2adjust2(1:trackmax(1),trackmax(1)*a*76+1:trackmax(1)*
a*77),RelVadjust2(1:trackmax(1),trackmax(1)*a*76+1:trackmax(1)*a*77));

corr78=corrcoef(R2adjust2(1:trackmax(1),trackmax(1)*a*77+1:trackmax(1)*
a*78),RelVadjust2(1:trackmax(1),trackmax(1)*a*77+1:trackmax(1)*a*78));

corr79=corrcoef(R2adjust2(1:trackmax(1),trackmax(1)*a*78+1:trackmax(1)*
a*79),RelVadjust2(1:trackmax(1),trackmax(1)*a*78+1:trackmax(1)*a*79));

corr80=corrcoef(R2adjust2(1:trackmax(1),trackmax(1)*a*79+1:trackmax(1)*
a*80),RelVadjust2(1:trackmax(1),trackmax(1)*a*79+1:trackmax(1)*a*80));

corr81=corrcoef(R2adjust2(1:trackmax(1),trackmax(1)*a*80+1:trackmax(1)*
a*81),RelVadjust2(1:trackmax(1),trackmax(1)*a*80+1:trackmax(1)*a*81));

corr82=corrcoef(R2adjust2(1:trackmax(1),trackmax(1)*a*81+1:trackmax(1)*
a*82),RelVadjust2(1:trackmax(1),trackmax(1)*a*81+1:trackmax(1)*a*82));

corr83=corrcoef(R2adjust2(1:trackmax(1),trackmax(1)*a*82+1:trackmax(1)*
a*83),RelVadjust2(1:trackmax(1),trackmax(1)*a*82+1:trackmax(1)*a*83));

corr84=corrcoef(R2adjust2(1:trackmax(1),trackmax(1)*a*83+1:trackmax(1)*
a*84),RelVadjust2(1:trackmax(1),trackmax(1)*a*83+1:trackmax(1)*a*84));

corr85=corrcoef(R2adjust2(1:trackmax(1),trackmax(1)*a*84+1:trackmax(1)*
a*85),RelVadjust2(1:trackmax(1),trackmax(1)*a*84+1:trackmax(1)*a*85));

corr86=corrcoef(R2adjust2(1:trackmax(1),trackmax(1)*a*85+1:trackmax(1)*
a*86),RelVadjust2(1:trackmax(1),trackmax(1)*a*85+1:trackmax(1)*a*86));

corr87=corrcoef(R2adjust2(1:trackmax(1),trackmax(1)*a*86+1:trackmax(1)*
a*87),RelVadjust2(1:trackmax(1),trackmax(1)*a*86+1:trackmax(1)*a*87));

corr88=corrcoef(R2adjust2(1:trackmax(1),trackmax(1)*a*87+1:trackmax(1)*
a*88),RelVadjust2(1:trackmax(1),trackmax(1)*a*87+1:trackmax(1)*a*88));

corr89=corrcoef(R2adjust2(1:trackmax(1),trackmax(1)*a*88+1:trackmax(1)*
a*89),RelVadjust2(1:trackmax(1),trackmax(1)*a*88+1:trackmax(1)*a*89));

corr90=corrcoef(R2adjust2(1:trackmax(1),trackmax(1)*a*89+1:trackmax(1)*
a*90),RelVadjust2(1:trackmax(1),trackmax(1)*a*89+1:trackmax(1)*a*90));

corr91=corrcoef(R2adjust2(1:trackmax(1),trackmax(1)*a*90+1:trackmax(1)*
a*91),RelVadjust2(1:trackmax(1),trackmax(1)*a*90+1:trackmax(1)*a*91));

corr92=corrcoef(R2adjust2(1:trackmax(1),trackmax(1)*a*91+1:trackmax(1)*
a*92),RelVadjust2(1:trackmax(1),trackmax(1)*a*91+1:trackmax(1)*a*92));

corr93=corrcoef(R2adjust2(1:trackmax(1),trackmax(1)*a*92+1:trackmax(1)*
a*93),RelVadjust2(1:trackmax(1),trackmax(1)*a*92+1:trackmax(1)*a*93));

corr94=corrcoef(R2adjust2(1:trackmax(1),trackmax(1)*a*93+1:trackmax(1)*
a*94),RelVadjust2(1:trackmax(1),trackmax(1)*a*93+1:trackmax(1)*a*94));

corr95=corrcoef(R2adjust2(1:trackmax(1),trackmax(1)*a*94+1:trackmax(1)*
a*95),RelVadjust2(1:trackmax(1),trackmax(1)*a*94+1:trackmax(1)*a*95));
```

```
corr96=corrcoef(R2adjust2(1:trackmax(1),trackmax(1)*a*95+1:trackmax(1)*
a*96),RelVadjust2(1:trackmax(1),trackmax(1)*a*95+1:trackmax(1)*a*96));

corr97=corrcoef(R2adjust2(1:trackmax(1),trackmax(1)*a*96+1:trackmax(1)*
a*97),RelVadjust2(1:trackmax(1),trackmax(1)*a*96+1:trackmax(1)*a*97));

corr98=corrcoef(R2adjust2(1:trackmax(1),trackmax(1)*a*97+1:trackmax(1)*
a*98),RelVadjust2(1:trackmax(1),trackmax(1)*a*97+1:trackmax(1)*a*98));

corr99=corrcoef(R2adjust2(1:trackmax(1),trackmax(1)*a*98+1:trackmax(1)*
a*99),RelVadjust2(1:trackmax(1),trackmax(1)*a*98+1:trackmax(1)*a*99));

corr100=corrcoef(R2adjust2(1:trackmax(1),trackmax(1)*a*99+1:trackmax(1)
*a*100),RelVadjust2(1:trackmax(1),trackmax(1)*a*99+1:trackmax(1)*a*100)
);

corr101=corrcoef(R2adjust2(1:trackmax(1),trackmax(1)*a*100+1:trackmax(1
)*a*101),RelVadjust2(1:trackmax(1),trackmax(1)*a*100+1:trackmax(1)*a*10
1));

corr102=corrcoef(R2adjust2(1:trackmax(1),trackmax(1)*a*101+1:trackmax(1
)*a*102),RelVadjust2(1:trackmax(1),trackmax(1)*a*101+1:trackmax(1)*a*10
2));

corr103=corrcoef(R2adjust2(1:trackmax(1),trackmax(1)*a*102+1:trackmax(1
)*a*103),RelVadjust2(1:trackmax(1),trackmax(1)*a*102+1:trackmax(1)*a*10
3));

corr104=corrcoef(R2adjust2(1:trackmax(1),trackmax(1)*a*103+1:trackmax(1
)*a*104),RelVadjust2(1:trackmax(1),trackmax(1)*a*103+1:trackmax(1)*a*10
4));

corr105=corrcoef(R2adjust2(1:trackmax(1),trackmax(1)*a*104+1:trackmax(1
)*a*105),RelVadjust2(1:trackmax(1),trackmax(1)*a*104+1:trackmax(1)*a*10
5));

corr106=corrcoef(R2adjust2(1:trackmax(1),trackmax(1)*a*105+1:trackmax(1
)*a*106),RelVadjust2(1:trackmax(1),trackmax(1)*a*105+1:trackmax(1)*a*10
6));

corr107=corrcoef(R2adjust2(1:trackmax(1),trackmax(1)*a*106+1:trackmax(1
)*a*107),RelVadjust2(1:trackmax(1),trackmax(1)*a*106+1:trackmax(1)*a*10
7));

corr108=corrcoef(R2adjust2(1:trackmax(1),trackmax(1)*a*107+1:trackmax(1
)*a*108),RelVadjust2(1:trackmax(1),trackmax(1)*a*107+1:trackmax(1)*a*10
8));

corr109=corrcoef(R2adjust2(1:trackmax(1),trackmax(1)*a*108+1:trackmax(1
)*a*109),RelVadjust2(1:trackmax(1),trackmax(1)*a*108+1:trackmax(1)*a*10
9));

corr110=corrcoef(R2adjust2(1:trackmax(1),trackmax(1)*a*109+1:trackmax(1
)*a*110),RelVadjust2(1:trackmax(1),trackmax(1)*a*109+1:trackmax(1)*a*11
0));
```

```
       TotalCorr=[corr1(2) corr2(2) corr3(2) corr4(2) corr5(2) corr6(2)
corr7(2) corr8(2) corr9(2) corr10(2) corr11(2) corr12(2) corr13(2)
corr14(2) corr15(2) corr16(2) corr17(2) corr18(2) corr19(2) corr20(2)
corr21(2) corr22(2) corr23(2) corr24(2) corr25(2) corr26(2) corr27(2)
corr28(2) corr29(2) corr30(2) corr31(2) corr32(2) corr33(2) corr34(2)
corr35(2) corr36(2) corr37(2) corr38(2) corr39(2) corr40(2) corr41(2)
corr42(2) corr43(2) corr44(2) corr45(2) corr46(2) corr47(2) corr48(2)
corr49(2) corr50(2) corr51(2) corr52(2) corr53(2) corr54(2) corr55(2)
corr56(2) corr57(2) corr58(2) corr59(2) corr60(2) corr61(2) corr62(2)
corr63(2) corr64(2) corr65(2) corr66(2) corr67(2) corr68(2) corr69(2)
corr70(2) corr71(2) corr72(2) corr73(2) corr74(2) corr75(2) corr76(2)
corr77(2) corr78(2) corr79(2) corr80(2) corr81(2) corr82(2) corr83(2)
corr84(2) corr85(2) corr86(2) corr87(2) corr88(2) corr89(2) corr90(2)
corr91(2) corr92(2) corr93(2) corr94(2) corr95(2) corr96(2) corr97(2)
corr98(2) corr99(2) corr100(2) corr101(2) corr102(2) corr103(2)
corr104(2) corr105(2) corr106(2) corr107(2) corr108(2) corr109(2)
corr110(2)];

       edges=[-1 -0.5 -0.3 -0.1 0.1 0.3 0.5 1];
       figure
       hist(TotalCorr,edges)
       TotalCorrHist=hist(TotalCorr,edges);
```